STUDY OF LOCALIZED POTENTIAL STRUCTURE AND HEATING IN EXPANDING HELICON PLASMA

By

SOUMEN GHOSH

PHYS06200904002

Institute For Plasma Research, Bhat

Gandhinagar 382428, India

A thesis submitted to the
Board of Studies in Physical Sciences

In partial fulfillment of the requirements
for the degree of

DOCTOR OF PHILOSOPHY

of

HOMI BHABHA NATIONAL INSTITUTE

November 2015

Homi Bhabha National Institute

Recommendations of the Viva Voce Committee

As members of the Viva Voce Committee, we certify that we have read the dissertation prepared by **Soumen Ghosh** entitled "STUDY OF LOCALIZED POTENTIAL STRUCTURE AND HEATING IN EXPANDING HELICON PLASMA" and recommend that it may be accepted as fulfilling the thesis requirement for the award of Degree of Doctor of Philosophy.

Dhiraj Bora ------------------------------ **Date :** 17/ 03/ 2016

Chairman : Prof. Dhiraj Bora

PKChattopadhyay ------------------------------ **Date :** 17/ 03/ 2016

Guide/ Convener : Prof. Prabal Kr. Chattopadhyay

Sudeep Bhattacharjee ------------------------------ **Date :** 17/ 03/ 2016

Examiner : Prof. Sudeep Bhattacharjee

JGhosh ------------------------------ **Date :** 17/ 03/ 2016

Member : Dr. Joydeep Ghosh

Devendra Sharma ------------------------------ **Date :** 17/ 03/ 2016

Member : Dr. Devendra Sharma

PKSharma ------------------------------ **Date :** 17/ 03/ 2016

Member : Dr. Promod Kr. Sharma

Final approval and acceptance of this thesis is contingent upon the candidate's submission of the final copies of the thesis to HBNI.

I hereby certify that I have read this thesis prepared under my direction and recommend that it may be accepted as fulfilling the thesis requirement.

PKChattopadhyay ------------------------------ **Date :** 17/ 03/ 2016

Guide : Prof. Prabal Kr. Chattopadhyay **Place:** IPR, Gandhinagar

STATEMENT BY AUTHOR

This dissertation has been submitted in partial fulfillment of requirements for an advanced degree at Homi Bhabha National Institute (HBNI) and is deposited in the Library to be made available to borrowers under rules of the HBNI.

Brief quotations from this dissertation are allowable without special permission, provided that accurate acknowledgement of source is made. Requests for permission for extended quotation from or reproduction of this manuscript in whole or in part may be granted by the Competent Authority of HBNI when in his or her judgement the proposed use of the material is in the interests of scholarship. In all other instances, however, permission must be obtained from the author.

Soumen Ghosh

DECLARATION

I, hereby declare that the investigation presented in the thesis has been carried out by me. The work is original and the work has not been submitted earlier as a whole or in part for a degree/diploma at this or any other Institution/University.

Soumen Ghosh

List of Publications arising from the thesis

Journal:

1. **Localized electron heating and density peaking in downstream helicon plasma**

   Soumen Ghosh, K. K. Barada, P. K. Chattopadhyay, J. Ghosh, and D. Bora. *Plasma Sources Sci. Technol.* **24**, 034011, (2015).

2. **Resolving an anomaly in electron temperature measurement using double and triple Langmuir probes**

   Soumen Ghosh, K. K. Barada, P. K. Chattopadhyay, J. Ghosh, and D. Bora. *Plasma Sources Sci. Technol.* **24**, 015017, (2015).

3. **RF compensation of single Langmuir probe in low density helicon plasma**

   Soumen Ghosh, P. K. Chattopadhyay, J. Ghosh, and D. Bora. *Under review for publication in Fusion Engineering and Design.*

4. **Role of magnetic aperture in downstream annular plasma formation**

   Soumen Ghosh, P. K. Chattopadhyay, J. Ghosh, and D. Bora. *To be submitted for publication in refereed journal.*

5. **Formation of multiple axial potential structures (MAPS) in expanding helicon plasmas**

   Soumen Ghosh, P. K. Chattopadhyay, J. Ghosh, and D. Bora. *To be submitted for publication in refereed journal.*

Conferences:

1. **A novel gridded retarding field energy analyzer for IEDF measurement**

   Soumen Ghosh, P. K. Chattopadhyay, J. Ghosh, and D. Bora. 42^{nd} *EPS Conference on Plasma Physics, 22-26 June 2015*, Lisbon, Portugal.

Soumen Ghosh

DEDICATIONS

Dedicated to my Maa, Baba, Didi, Jiju and my niece who encouraged me to "stay on it".

ACKNOWLEDGEMENTS

It gives me an immense pleasure to become a PhD graduate from Institute for Plasma Research, Bhat, Gandhinagar, India. This thesis would not have been completed without the support and guidance of many people, whom I would like to thank from bottom of my heart. I would like to thank each and everyone, who have been involved directly or indirectly in the research activities carried as a part of my dissertation.

I sincerely thank to Prof. Prabal Kr. Chattopadhyay with deep sense of gratitude for serving as thesis adviser and chief motivator during my PhD. Prof. Chattopadhyay's guidance has been instrumental in developing research and scientific skills throughout my PhD. He scrutinized all my experimental activities, starting from the techniques used to report the observations. His demand for excellence has fostered me a drive and motivation that I hope will bring great success in the future. It has truly been a privilege to work with Prof. Chattopadhyay.

I thank all the "Doctoral Committee" members for following up the step by step progress made during my thesis work. Especially, I express my gratitude to my PhD doctoral chairman, Prof. Dhiraj Bora for his constant support and encouragement during my PhD and motivation to finish the work timely. I am grateful to Dr. Joydeep Ghosh for his thorough scrutiny on my manuscripts and discussion on the way of representing the work. I am thankful to him for his help to develop such skills on me. I appreciate the crucial role played by other "Doctoral Committee" members, Dr. D. Sharma and Dr. P. K. Sharma by reviewing my work, critical comments and their encouragement to learn additional techniques.

I am extremely thankful to Prof. Y. C. Saxena, Prof. P. K. Kaw, Prof. A. Sen and Prof. R. Pal for their valuable suggestions and discussion at various stage during my PhD. I am grateful to other faculty members, Prof. R. Jha, Prof. Amita Das, Prof. S. Mukherjee, Dr. R. Ganseh, Dr. D. Raju, Dr. S. Sengupta, Dr. Ramasubramanian, Dr. M. Warrier, Dr. R. Goswami, Dr. M. Kundu, Dr. A. K. Chattopadhyay, Dr. R. Kaur, Dr. L. M. Awasthi, Dr. G. Ravi, M. Bandyopadhyay and others, who have taught me basic plasma physics, experimental, computational techniques and other disciplines of physics during the pre-PhD course work. Special thanks to Dr. Pintu Bandyopadhyay for spending his valuable time for proofreading my thesis and I highly appreciate his valuable comments and suggestions.

There were many helping hands during several instances when I was in need of information or equipments for the experiment and other related activities. I would like to acknowledge Mr. Varadarajulu, Mr. Sunil Kumar, Mr. Sunil Churasma, Hiral, Lavkesh, Pankaj-ji, Amulya da, LVPD group, Aditya group, Electronics lab, Workshop, Library, Computer center, Drafting section, Water cooling, Store, Purchase, Accounts, Administration and Transport section for their help and I convey my sincere thanks to all of them.

I express my sincere thanks to the seniors and friends in the hostel for their company and unconditional support ever. My warm regards to Rameswar, Sushil, Sanat, Pravesh, Kshitish, Deepak, Ujjwal, Gurudatt, Vikram, Prabal, Ashwin, Sharad, Satya, Shekar, Jugal, Kishor, Vikrant bhai, Sita, Sunita and Maya di. My Best wishes to my batchmate Aditya and Iliyas and my labmate Sayak, Manjit and Sonu and my junior friends Vikram Dharodi, Veda, Rana, Rimza, Dushyant, Vara, Bibhu, Neeraj, Rupendra, Chandrasekhar, Mangilal, Meghraj, Akanksha, Vidhi, Deepa, Harish, Samir, Debraj, Ratan, Narayan, Arghya, Umesh, Modhu, Amit, Bhumika, Surabhi, Sagar, Chetan, Atul, Deepak Verma, Alam, Prabhakar, Jervis, Sandeep, Pallavi, Minakshi, Harshita and other scholars and TTPs for taking me to grow with all of you together in the hostel, a delightful natural ambient inside the campus. I fill honored to get a place together with all of you in our hostel to go years long. I have enjoyed every moment with all of you playing games especially Volleyball, Football and Cricket.

Last but not least, I would like to convey my hearty gratitude and respect to my parents: Maa, Baba, Didi, Jiju and my niece Jolly whose blessings, guidance and moral support helped me to achieve my goal to become a PhD graduate. It is undoubtedly true that this work would not have been possible, without the consistent support and encouragement from my family.

Soumen Ghosh

SYNOPSIS

Plasma is a unique medium which supports several kinds of waves. Whistler wave is one of such waves in magnetized plasma. It is a polarized electromagnetic wave, propagating along the magnetic field. A class of such low frequency ($\sqrt{\omega_{ce}\Omega_{ci}} < \omega < \omega_{ce}$) whistler wave is known as helicon wave, observed in laboratory plasmas. Its electric field propagates helically along the magnetic field direction. The waves, launched by a helical antenna, produce plasmas with higher ionization efficiency leading to production of high density plasma. In addition, when the helicon antenna produced plasmas are subjected to geometric and magnetic expansion, it is shown to produce localized potential structures near the expansion region. Plasma, produced inside a narrow source chamber, where the antenna is placed, diffuses into a large expansion chamber, called the downstream region. The content of this thesis provides a detailed experimental study of downstream physics of expanding helicon plasmas.

Helicon sources are attractive for material processing application purpose as they are capable of producing high density plasma, where the ion density and ion energy can be controlled independently. Plasma expansion may be associated with complex transport phenomena including double layer like potential structure formation and instabilities. In this kind of systems, ionization dominates mainly in the source chamber and geometrical expansion leads to a gradient in the plasma density, decreasing from source to the expansion chamber. In these expanding plasmas, generally the electrons closely obey the Boltzmann equilibrium and the gradient of density is accompanied by a very weak gradient in DC plasma potential. Consequently, a very weak electric field accelerates positive ions out of the source. In general the plasma remains quasi-neutral during the expansion and the ion acceleration remains insignificant in this case. Adding strong magnetic divergence together with the geometrical expansion leads to enhancement of ion acceleration and generation of supersonic ions. Production of supersonic ions in the expanding helicon plasmas, having both the geometric and magnetic expansions, opens up a new area of application of these kinds of systems in the field of electric propulsion. These expanding helicon plasma systems now competes with other current driven thrusters such as ion engine and Hall thrusters etc. Formation of potential structures, known as double layers and its current-less character differentiates the helicon double layer thruster from other electric propulsion systems. Research has been progressed significantly in this direction since 2003 for investigating double layer like potential structures, ion beam and thrust generation in expanding helicon plasmas. However, there exists many open questions such as the stability and dynamics of the double layers, which needs to be answered. For example observations of Multiple Axial Potential Structure (MAPS) in high pressure ($> 10^{-1} mbar$) glow discharge plasmas are not being directly observed in expanding helicon plasmas. Although there exist some indications of presence of MAPS following the measurements of multiple ion beams. This motivates further investigation of the existence of MAPS in the **He**licon **eX**perimental (**HeX**) system at the Institute for Plasma Research, India. A transition from single axial potential structure (SAPS) to MAPS is obtained by changing the magnetic field topology after the throat expansion in HeX. Observation of MAPS in HeX-system with comprehensive analysis in association with measurements of ion beam energy and axial profiles of density and electron temperature constitutes the novelty of this thesis.

BGK theory predicts that there must be atleast four groups of particles such as trapped/ untrapped electrons and ions are necessary to form an equilibrium double layer like potential structure. MAPS are known to be formed in high pressure ($> 10^{-1} mbar$) glow discharge plasmas. Although not substantiated, but it is conjectured that in the glow discharge MAPS, the electrons having energies more than the first potential barrier (first double layer like structure) overcome the barrier and cause ionization with the background neutrals maintaining the threshold density required for producing another potential structure adjacent to the first one. However, in the helicon discharges, untrapped electrons overcoming the first potential barrier have longer mean free path because of low neutral pressures and hence are not able to cause further ionization to form another structure. Therefore, the mechanism responsible for maintaining threshold density even after the magnetic and geometrical expansion is important to understand the cause behind the formation of MAPS, which is experimented and discussed in detailed in this thesis. Plasma generated by radio-frequency power radiation through an antenna, where energy is transferred from antenna to plasma electrons to produce heating by collisional and collision-less mechanisms. The antenna driven RF oscillation propagates in the plasma and are guided by the magnetic fields. Specific design of antenna is required for launching propagating electromagnetic waves. The shape of antenna determines the wavelength, mode structure and mode number of the wave. Collision-less wave particle interaction known as Landau damping plays an important role in obtaining global electron heating and density determination particularly at relatively low density ($\sim 10^{16} m^{-3}$) helicon plasmas as being produced in HeX machine. Localized helicon wave power absorption away from the helical antenna leads to increase in local electron temperature. As the electrons are heated locally, they rapidly escape the local volume, creating a density trough in that location. Further downstream beyond geometric and magnetic expansion regions, the electron temperature falls off sharply and a density rise is observed to maintain the pressure constant, which corresponds to the formation of second potential structure. Cusp like magnetic field profile inside the expansion controls this downstream density rise and when this density rise reaches the threshold limit, the second potential structure is formed. Double layer like potential structures formation in this kind of expanding helicon system produces thrusts along the axial direction. However, the radial density distribution plays an important role for controlling and determining the axial thrust efficiency. Annular plasma is observed both in presence and absence of axial potential structures in HeX. A proper physical understanding of formation of annular plasma and its control in HeX, forms another major contribution of this thesis in expanding helicon plasma research.

In free space, whistler waves are right circularly polarized electromagnetic waves, but in a radially bounded axial system it produces short wavelength electrostatic components as well, called Trivelpiece-Gould (TG) mode. Whistler wave dispersion in a bounded magnetized system allows existence of long-wavelength helicon together with short-wavelength TG mode. A half wave right helicon antenna is used to launch helicon wave in HeX, which propagates away from the antenna into the bulk plasma, where the wave energy is absorbed by the electrons. The thesis starts with the presentation of analytical derivation using both cold plasma and generalized ohms law of Helicon and TG mode dispersion relation in context of the experimental regimes in HeX. It is followed with the detailed description of HeX-system and the diagnostics developed for studying above mentioned problems are discussed. A brief summary of each chapter with a comprehensive understanding of major physical observations are described in the following:

Chapter-1: *Introduction and outline of the problem.* Detailed literature survey and current status of the research work in helicon antenna produced expanding radio-frequency plasma is presented. The important advances in this field are highlighted and open problems in the area of potential structures formation, localized electron heating and downstream inhomogeneity after the expansion are mentioned, followed by the motivation of the thesis.

Chapter-2: *Physics of helicon discharges.* In radio-frequency plasmas, the wave energy is transferred to the plasma electrons to produce heating predominantly by collision-less mechanism. Helicon wave discharge achieves high ionization efficiency. In this method the wave energy is transferred resonantly to the plasma electrons to produce heating and plasma production. Helicon waves belong to the class of low frequency whistler waves. The whistler wave dispersion relation is presented here using cold plasma as well as generalized Ohms law. Helicon and Trivelpiece-Gould (TG) modes and RF power transfer mechanisms are also discussed in this chapter.

Chapter-3: *HeX system and implemented diagnostics.* The expanding helicon plasma experimental system is described in detail. Source and diffusion chamber, antenna configuration, RF power, driving frequency, shielding and grounding are discussed. Orientation of electromagnets to produce desired magnetic field configurations are also given here.

Various electrical probes such as RF compensated single Langmuir probe, Double probe, Triple probe, Emissive probe, Retarding field energy analyzer (RFEA) and high frequency different kinds of Magnetic probes are developed for plasma diagnosis in this system. The techniques used for measurements, method of operation and estimation of local parameters from the measurements are discussed. Interpretations of Single Langmuir probe measurements in electrode-less radio frequency (RF) plasmas require adequate RF compensation. Conventional RF compensation technique is limited only at high density ($> 10^{17} m^{-3}$) RF plasmas. RF compensation of Single Langmuir probe is achieved at low density RF plasmas ($\sim 10^{16} m^{-3}$) even when there are limitations from getting very high impedance ($\sim 500k$) self-resonant tiny choke. A manuscript with describing the technique to compensate RF modulation at low density plasma is *under review* for publication in *(S. Ghosh et al.) Fusion Eng. Design.*

Langmuir probes with its variants such as single, double and triple probes remain the most common method of electron temperature measurement in low-temperature laboratory plasmas. However, proper estimation of electron temperature mainly using triple probe configuration requires the proper choice of compensation factor (W). Determination of the compensating factor is not very straightforward as it depends heavily on plasma floating potential (V_f), electron temperature (T_e), the type of gas used for plasma production and the bias voltage applied to probe pins, especially in cases where there are substantial variations in floating potential. In this chapter resolving anomaly in electron temperature measurement using triple Langmuir probe and compared the electron temperature measurements with its other two variants single and double Langmuir probe. Moreover, for proper compensated T_e values measured using the triple probe suitable bias voltage range (V_B) is also investigated. This work has been published in *(S. Ghosh et al.) Plasma Sources Sci. Technol. 24, 015017, (2015).*

A retarding field energy analyzer (RFEA) has been developed to measure ion energy distribution function (IEDF) in helicon plasmas. The gridded energy analyzer is widely used in many machines including cold plasmas in linear machine and hot tokamak plasmas to measure ion/electron distribution. It is well known that grid transparency and their spacing plays important role to optimize the RFEA energy resolution. Although the RFEA are being used for last few decades there are several technical knowhow on RFEA construction which are yet to be understood fully. Some of those issues are discussed in this thesis. DC characterization is carried out to understand suitable repeller bias voltage and bias scheme for ion collection mode operation, which has been published in *(S. Ghosh et al.)* 42^{nd} *EPS Conference on Plasma Physics, 22-26 June (2015).* A low frequency ($\sim 50mHz$) transistor amplifier circuit is used for application of bias to the discriminator and collector signal is acquired using an analog (I to V) converter circuit, which detects the ion beam generated from the double layer like potential structure in this expanding helicon plasma system. RFEA in ion collection mode operation, the untrapped energetic electrons, coming out from the double layer like potential structure, are responsible for the creation of off-sets in collector signal. Thus the location of RFEA for ion beam energy measurement is crucial, which is also discussed in detail in this thesis.

Chapter-4: *Multiple Axial Potential Structure (MAPS) formation.* Spontaneous formation of electrostatic potential structures in geometric and magnetic expanding plasma has great importance to study the ion beam formation mechanism. These structures also have useful application in space plasma thruster. In quasi-neutral plasma it does not have significant electric field, but if the plasma quasi-neutrality locally violates, then plasma will have a local potential gradient and consequently a strong electric field compared to ambipolar field. This layer of non-neutral regime separates two quasi-neutral plasmas called the double layer like potential structures. This electrostatic structure can be static or transient, which forms inside the bulk plasma far away from the sheath edge plasma boundary. Current-free double layer like potential structures have been observed in expanding helicon plasma systems where both geometric and magnetic expansion are present. Recent observation of multiple ion beams, indirectly evident that there may form multiple double layer like structures. However, there is no such direct evidence for the formation of multiple double layer like structures, in an expanding helicon plasma systems. This motivates us to investigate further to get multiple axial potential structures (MAPS) in expanding helicon plasma system. Generation of cusp like magnetic field configuration after the throat helps to generate MAPS like potential structure. Associated ion beam generation, having energy nearly equal to the potential drops corresponding to first strong structure confirms the existence of the structure. Second weak structure, found to be much sharper than the predicted Boltzmann potential drop, confirms the existence of the second structure. The density profile maintains in such way in the system that it gives two unidirectional axial gradients, which corresponds to two potential structures. A manuscript with observation of multiple axial potential structures (MAPS) formation is *to be submitted for publication in (S. Ghosh et al.) refereed journal.*

Chapter-5: *Localized electron heating.* To investigate the source, maintaining threshold density even after the geometric and magnetic expansion, helicon wave interaction with plasma electrons is thoroughly characterized. It is observed that the electrons are locally heated up axially away from the antenna center and the corresponding local density drops down and farther away from this location inside the diffusion chamber density again rise up. These localized electron heating and downstream density rise observation is critically analyzed and find out the root cause behind this is discussed in this section. Presence of dumped helicon wave is identified at low densities ($\sim 10^{16} m^3$). The measured helicon wavelength is just about twice the antenna length and the phase velocity (v_p) is almost equal to the speed required for electron impact ionization. These experimental observations strongly advocate the Landau damping heating and density production by the helicon waves, particularly in low density plasma. Electron heating, confined at $35-45$ cm away from the antenna center, strongly indicates a source of local power absorption, occurring due to dumped helicon waves at those locations. Further downstream from the location of the maximum electron temperature, a density rise is observed, which is located $55 - 65$ cm away from the antenna. Location of both electron heating and density peaking can be varied by changing the axial magnetic field topology. This downstream density rise causes as a result of maintaining the pressure balance in the system. The major findings presented in this chapter have been published in *(S. Ghosh et al.) Plasma Sources Sci. Technol. 24, 034011, (2015).*

Chapter-6: *Inhomogeneous downstream plasma.* Radial density inhomogeneity or annular plasma formation detriments the axial thrust efficiency for electric propulsion, where the rotational kinetic energy is converted into axial kinetic energy due to gas dynamical expansion from narrow source to wide expansion chamber. It is believed that the radial electric field which generates a poloidal current (J) causes (J $\times$ B) forces to the electrons and pushed them away from the central location. Ions are also following them as they are electrostatically coupled to each other, creating annulus. In this thesis, it is shown that the annular plasma can be formed both in presence and absence of radial as well as axial electric fields. Presence of tail electrons are observed only at the off axial location where the density is piling up. Recycling neutrals from the conducting expansion chamber fulfil the sufficient ionization length for neutral ionization with the tail electrons. Detailed discussion is carried out in this chapter to establish the reason for the formation of annular plasma and its control. Moreover, the dominant role between geometric and magnetic aperture for the formation of downstream annular plasma is also unclear, which will also be discussed in this thesis. Experimental verification of the above model describing the formation of downstream plasma annulus is *to be submitted for publication in (S. Ghosh et al.) refereed journal.*

Chapter-7: *Conclusion and future scope.* This thesis work provides the first clear experimental evidence for the formation of current-less MAPS in expanding helicon plasmas. The thesis establishes the cause behind the localized electron heating and downstream density rise in expanding helicon plasma. The root cause behind the formation of downstream annular plasma formation in expanding helicon plasma is also explained with proper physics model. The future scope of the work is also presented in this chapter.

Contents

List of Figures

List of Tables

1 Introduction

1.1 General introduction

Plasma is a ionized medium, contain mixtures of lighter electrons, heavier particles such as ions (positive or negative) and neutrals, exhibits collective behavior. Plasmas are primarily characterized by the electron temperature (T_e) and density (n_e). The wide dynamic range of plasma electron temperature and density offers distinctive properties of the plasma, where each of the parameter space has unique feature. The dynamical range of electron temperature and density shown in figure 1.1 [1], shows the existence of various kind of plasmas.

This thesis research deals with the low temperature Laboratory plasma, where the plasma is produced by application of radio frequency power into it though a right helical antenna. Plasma does not support to have an electric field because it tries to maintain the "quasi-neutrality" ($n_e \approx n_i$). "Quasi-neutrality", describes apparent overall charge neutrality, while at small scales (within $\sim \lambda_D$, Debye length), charge particles may give rise to electric field. It is well known that quasineutrality violation happens at the plasma edge called sheath. However, there are examples where this may happen deep inside the main plasma under different circumstances. Generation of this kind of local violation of quasineutrality inside

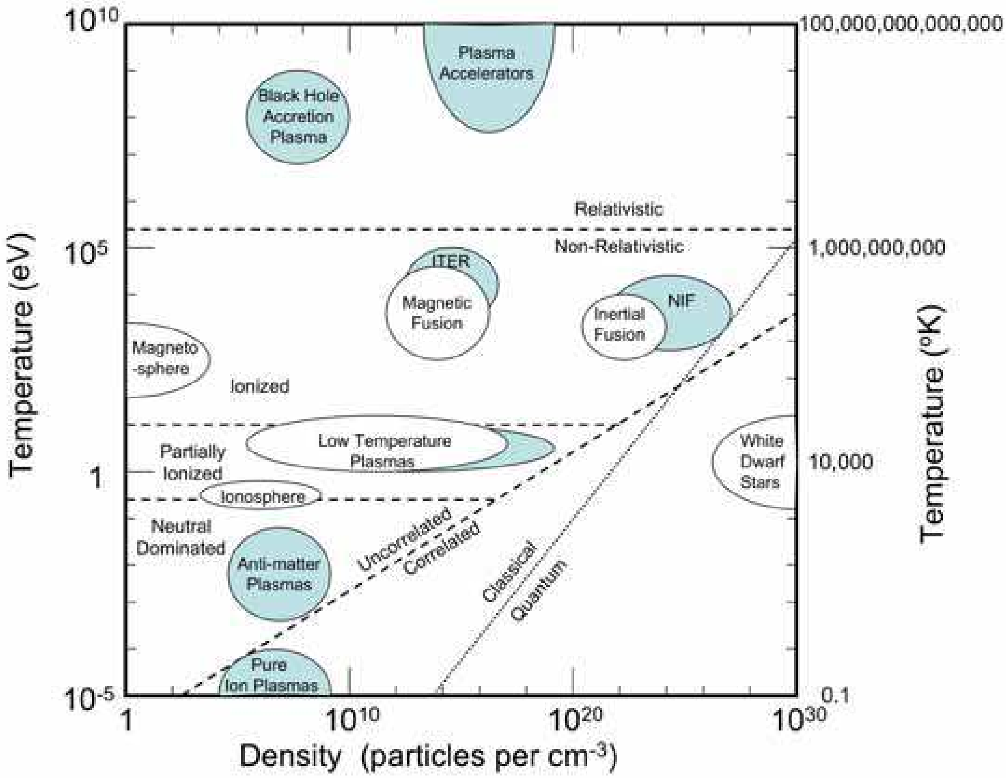

Figure 1.1: The dynamic range of n_e and T_e for plasmas.

the bulk plasma giving rise of electric field, is called double layer [2, 3]. One example of existence of such potential structure is observed in a geometrically expanding plasma in association with magnetic field divergence [4]. The double layer essentially consists of two separate positive and negative charge layers. This structure accelerates ions and electrons in a direction opposite to each other, creates a non-zero current flowing through the plasma. Double layer (DL) is also observed in Earth's magnetosphere [5]. Ion energy distribution function measurements by spacecraft, DLs have been identified in magnetospheric regions ranging from the aurora zone to the plasma sheet [6, 7]. These double layers are essentially "current-free" as there is no net current due to unbounded plasma. However, double layer is observed in laboratory (in 2003) in a helicon plasma system consists of geometric and magnetic expansion is also "current-free" [4].

Boswell et al. in 1970 [8] used helicon antenna for producing plasma. Latter on, they showed helicon wave sustained plasma is an efficient source for high density plasma production [9]. The density obtained in helicon discharge is higher by an order compared to RF discharge with same source power and magnetic field. This highly efficient helicon plasma production is attractive and has growing interests in helicon plasma physics as well as its various potential applications. In this decades they are considered for many application like material procession [10], negative ion production [11], pre-ionization [12, 13] and current drive [14–16] in fusion plasmas. More recently, helicon waves have been considered for space propulsion [17, 18], where the source of ionization can be due to the upstream energetic electron or due to localized heating. VASIMIR engine [17] is utilizing helicon as an ionizing source. The charge particle acceleration mechanism is due to axial potential gradient or double layer like structure, created near the expansion throat at low pressure bellow $\sim 5 \times 10^{-4}$ mbar in helicon plasma, where ion can be accelerated in supersonic speed. Although, current free such double layer like structure has been observed by other authors [4, 19, 20], the location and strength of double layer and the governing physics with magnetic field topology is not clear yet.

1.2 Motivation

Double layers are often found in coexistence with currents flowing parallel to the electric field. In magnetospheric physics, these structures are mostly recognized by 1) particles accelerated through the double layers and 2) in measurements of the electrostatic potential leap. Double layers are thought to be created either in sheaths where two plasmas of different properties merge, or plasmas dominated by currents. Double layers created under such conditions are respectively called weak and strong. In this context, weak and strong refer to the energy gained or lost by a particle passing through the double layer. Electric thrusters offer an attractive option for various in space propulsion tasks due to their high thrust efficiencies [21]. The performance characteristics of a compact electric thruster utilizing a helicon plasma source is investigated with the goal of identifying potential thrust mechanisms [22, 23].

Nearly all recent current free double layer experiments have been performed in expanding helicon plasma devices, having different source to expansion chamber aspect ratios. *Charles* and *Boswell* at Australian National University (ANU) started the current free double layer experiments in expanding helicon plasma [4]. *Charles et al.* [19] and *Singh* [20] provide a thorough review of recent current free double layers. *Thakur et. al.* at West Virginia University (WVU) worked on the instability threshold on formation of double layer [24]. *Wiebold et. al.* at Wisconsin University [25] and *Sun et. al.* at WVU [26] showed the ion energy distribution measurements in presence of "double layer like potential structure" using Laser Induced Fluorescence (LIF). Single double layer is usually observed in experiment. However, under certain experimental conditions two or more subsequent double layers, called a multiple double layer is observed in other experiments [27–30]. In a current driven system multiple double layer has been reported in glow discharge, double and triple plasma device [27–29, 31, 32]. In double plasma device, filament discharge experiments have been carried out for investigating the transition from single to multiple axial potential structures by (i) increasing the separation distance between the two filaments and (ii) by changing the filament current to each of the filaments [28]. It is observed from this experiment that transition from single to multiple such structure is formed above a critical separation distance between the two filaments. This confirms that the boundary condition has an important role for the formation of multiple such structures. On the other hand change of the filament current causes to vary density and temperature. Therefore, by changing the filament current one has the independent control over debye length (λ_D), for a fixed boundary or separation between two grids. Instead of mechanical change between two grids, it is possible to reach the sufficient condition ($\xi = \frac{L}{\lambda_D} \sim 10^{-5}$) by changing the filament current or λ_D for producing the multiple axial potential structures [28]. All the above mentioned double layer potential structures belong to the current driven group. Multiple Axial Potential Structures (MAPS) have not been directly observed in current-less devices such as expanding helicon plasma system. This is the main motivation of this thesis to peruse detail study in this topic.

1.3 Helicon: A class of whistler waves

Ionospheric whistlers were discovered during the first World-war while German radio monitors were trying to intercept Allied radio transmissions [33]. Without narrow band tuners, the whistlers occurred as declining tones in the audio band. They were later traced by tracking their lightning and propagation in the ionosphere and the magnetosphere [34]. In order to see the characteristics of this mode of propagation, one has to note that it occurs in regions ($\omega_{ci} << \omega << \omega_{ce} \sim \omega_{pe}$) [35]. In electron and ion species plasmas, the simple cold plasma dispersion relation for the right-handed wave, $n^2 = R = \frac{k^2c^2}{\omega^2}$, which propagates parallel to B_0 is given by the following equation

$$R = 1 - \frac{\omega_{pi}^2}{\omega(\omega + \omega_{ci})} - \frac{\omega_{pe}^2}{\omega(\omega - \omega_{ce})}. \tag{1.1}$$

For intermediate frequency regime ($\omega_{ci} << \omega << \omega_{ce}$), the above equation reduced to

$$R = 1 + \frac{\omega_{pe}^2}{\omega\omega_{ce}}, \tag{1.2}$$

and for $\omega_{ce} \sim \omega_{pe}$, $\omega_{pe} >> \omega$, the above equation becomes

$$R = \frac{\omega_{pe}^2}{\omega\omega_{ce}} = \frac{c^2k^2}{\omega^2} \tag{1.3}$$

$$\Rightarrow \omega = \frac{c^2k^2\omega_{ce}}{\omega_{pe}^2} \tag{1.4}$$

Hence phase velocity

$$v_\phi = \frac{c}{n} = \frac{c^2\omega_{ce}}{\omega_{pe}^2}k = c\sqrt{\frac{\omega\omega_{ce}}{\omega_{pe}^2}}, \tag{1.5}$$

and group velocity,

$$v_g = \frac{\partial \omega}{\partial k} = \frac{2c^2\omega_{ce}}{\omega_{pe}^2}k = 2v_\phi = 2c\sqrt{\frac{\omega\omega_{ce}}{\omega_{pe}^2}}, \tag{1.6}$$

of the wave are proportional to $\sqrt{\omega}$, which causes high frequencies to propagate faster along the magnetic field lines. The whistlers in the audio range in the northern hemisphere are most commonly caused by lightning strokes in the southern hemisphere (and vice versa) which are guided by the Earth's magnetic fields, and the dispersion led to the detection of a declining tone which was heard as a whistle [35] and hence the name whistler wave.

Plasma is a unique medium which supports several kinds of waves. Whistler wave is one of such waves in magnetized plasma. It is a polarized electromagnetic wave, propagating along the magnetic field. A class of such low frequency ($\sqrt{\omega_{ce}\Omega_{ci}} < \omega < \omega_{ce}$) whistler wave is known as helicon wave, observed in laboratory plasmas. Its electric field propagates helically along the magnetic field direction. The name "helicon" is introduced by Aigrain to describe the propagation of electromagnetic wave in presence of an applied magnetic field at low temperature plasmas, with frequencies lies between electron and ion cyclotron frequencies [36]. The waves, launched by a helical antenna, produce plasma with higher ionization efficiency leading to production of high density plasma. In addition, when the helicon antenna produced plasmas are subjected to geometric and magnetic expansion, it is shown to produce localized potential structures near the expansion region. Plasma, produced inside a narrow source chamber, where the antenna is placed, diffuses into a large expansion chamber, called the downstream region.

Important characteristic feature of waves in plasma is that they are subject to damping even in the absence of particle collisions. The collision-less wave damping plays important role in plasma heating and current drive which can be effectively used in further raising the temperature of a plasma already having a temperature high enough where the collisional Joule heating is ineffective. A general fluid description method considering both species ions and electrons will be presented for waves in collision-less, magnetized plasma.

1.4 Overview and relevant previous work

Helicon waves are low frequency ($\sqrt{\omega_{ce}\Omega_{ci}} < \omega < \omega_{ce}$) whistler wave, observed in bounded magnetized plasma. In free space, whistler waves are right circularly polarized electromagnetic waves, but in a radially bounded axial system it produces short wavelength electrostatic components as well, called Trivelpiece-Gould (TG) mode in 1959 [37]. After four decades Trivelpiece-Gould (TG) mode in helicon plasma has been experimentally observed [38]. Whistler wave dispersion in a bounded magnetized system allows existence of long-wavelength helicon together with short-wavelength TG mode. Helicon sources are attractive for plasma processing applications due to high density plasma production at low magnetic field with an ionization efficiency which is much higher than expected for $\sim 3eV$ electron temperature [9].

After Boswell's successful demonstration of efficient production of high density plasma using helicon waves [9], a variety of experiments have been carried out to investigate the physics of helicon discharges [8, 38–45]. Theoretical and experimental investigation on helicon discharge focused primarily on helicon wave mode structures and the mechanism responsible for efficient ionization to produce high density plasma. Klozenberg et al. have derived the helicon wave dispersion relation for a uniform bounded cylindrical plasma, known as KMT theory [46]. The theory describes wave dispersion and damping when the effects of electron and ion inertia are neglected. Davies et al. [47] have described the helicon wave dispersion and damping using generalized Ohms law for a non-uniform cylindrical resistive plasma bounded by a conductor, including the effects of electron inertia. The separation of the Hall and electron inertia terms in the wave dispersion was shown by Boswell [48]. Chen et al. [40, 49] have extended this work on helicon wave dispersion analytically for nonuniform plasmas bounded by insulating wall to predict the helicon wave mode structures. Several researchers have measured the spatial variation of helicon wave magnetic field structures [41, 50–53]. Remote ionization by helicon waves, axially far away from the antenna in a cylindrical system was shown by Ellingboe (1995) [54] and Degeling (1996) [42, 55].

In case of low density plasmas bellow $\sim 5\times10^{18}m^{-3}$, Chen et al. have suggested Landau damping as the dominant mechanism for energy transfer from helicon wave to plasma electrons [40, 56]. Helicon antenna produced helicon waves have been experimentally demonstrated the power absorption mechanism via Landau damping wave particle interaction [56]. Kamori et al. have experimentally shown helicon wave phase velocity measurements, which qualitatively supported the Landau damping hypothesis in low density helicon plasmas [56]. However, Keiter et. al. have argued that Landau damping may not be the a viable candidate for electron energization in their high density helicon plasmas in 1997 [57]. Couple of years later, Chen et al. reported that Landau damping mechanism is incapable of producing sufficient ionization to account for the high densities produced in helicon plasmas [58]. However, in this same paper they acknowledged that for very low density plasmas, Landau damping can still be a source of heating and density production.

Further, Chen et al. have investigated the behavior of undamped normal modes of helicon waves in a uniform plasma filling a long conducting or insulating cylinder [59]. When finite electron mass is taken into account, a second branch of the dispersion relation appeared. This identified as electron cyclotron TG mode with short radial wave length, propagating primarily inward from the radial boundary. The effect of the TG wave is expected to be important only for low DC magnetic fields [59]. The undamped normal modes of the helicon (H) and TG waves have distinctly different wave patterns at high magnetic fields but at low fields have similar patterns and therefore interact strongly [60]. Chen et al. further argued absorption of helicon waves occurring via mode coupling of helicon waves to the TG waves at the boundary, followed by strong damping of the short wavelength TG wave. Akhiezer et al. [61] have suggested that damping of the helicon wave by excitation of parametrically driven ion sound turbulence may explain the helicon wave damping rate and the downstream plasma density peak, often observed in helicon plasmas [62]. Kline et al. have identified appearance of parametrically driven waves in helicon plasmas [63]. Efficient coupling between the parametrically excited waves [64, 65] and plasma ions and electrons can lead to enhanced plasma density, electron temperature and ion temperature. In last two decades, significant effort made to understand the various aspects of ion heating [66–70] in helicon plasmas as well.

Helicon sources are attractive for material processing application purpose as they are capable of producing high density plasma, where the ion density and ion energy can be controlled independently. Radio frequency antenna driven helicon sources produce high density plasma in a narrow tube which diffuses into a comparatively large expansion chamber, where large wafer for material processing can be accommodated. The processing material on the wafer can be bias separately to control the energy of the deposited ion and density can be controlled by the changing the antenna currents. This necessary requirement for material processing makes the shape of the helicon reactor as geometrically expanding system, which consists of a narrow source chamber and a comparatively large expansion chamber. High density plasma produces inside the source chamber which diffuses into the expansion chamber. The content of this thesis provides a detailed experimental study of downstream physics of expanding helicon plasmas.

1.5 Objective of this research

Plasma expansion from narrow source chamber to wide expansion chamber may be associated with complex transport phenomena including double layer like potential structure formation and instabilities. In this kind of systems, ionization dominates mainly in the source chamber and geometrical expansion leads to a gradient in the plasma density, decreasing from source to the expansion chamber. In these expanding plasmas, generally the electrons closely obey the Boltzmann equilibrium and the gradient of density is accompanied by a very weak gradient in DC plasma potential. Consequently, a very weak electric field accelerates positive ions out of the source. In general the plasma remains quasi-neutral during the expansion and the ion acceleration remains insignificant in this case. Adding strong magnetic divergence together with the geometrical expansion leads to enhancement of ion acceleration and generation of supersonic ions. Production of supersonic ions in the expanding helicon plasmas, having both the geometric and magnetic expansions, opens up a new area of application of these kinds of system in the field of electric propulsion. These expanding helicon plasma systems now competes with other current driven thrusters such as ion engine and Hall thrusters etc. Formation of potential structures, known as double layers and its current-less character differentiates the helicon double layer thruster from other electric propulsion systems. Research has been progressed significantly in this direction since 2003 for investigating double layer like potential structures, ion beam and thrust generation in expanding helicon plasmas. However, there exists many open questions such as the stability and dynamics of the double layers, which needs to be answered. For example observations of Multiple Axial Potential Structure (MAPS) in high pressure ($> 10^{-1} mbar$) glow discharge plasmas are not being directly observed in expanding helicon plasmas. Although there exist some indications of presence of MAPS following the measurements of multiple ion beams. This motivates further investigation of the existence of MAPS in the **He**licon e**X**perimental (**HeX**) system at the Institute for Plasma Research, India. A transition from single axial potential structure (SAPS) to MAPS is obtained by changing the magnetic field topology after the throat expansion in HeX. Observation of MAPS in HeX-system with comprehensive analysis in association with measurements of ion beam energy and axial profiles of density and electron temperature constitutes the novelty of this thesis. Double layer like potential structures formation in this kind of expanding helicon system produces thrusts along the axial direction. However, the radial density distribution plays an important role for controlling and determining the axial thrust efficiency. Annular plasma is observed both in presence and absence of axial potential structures in HeX. A proper physical understanding of formation of annular plasma and its control in HeX, forms another major contribution of this thesis in expanding helicon plasma research.

This dissertation comprises both the development and enhancement of diagnostic techniques and explorations of fundamental physics of downstream helicon plasma. Localized electron heating away from the helical antenna which governs the appearance of downstream density rise, meets the critical density threshold for another potential structure formation is explored in detail. Independent role of magnetic and geometric aperture, two component electron temperatures is also studied. Retarding field energy analyzer (RFEA) is developed for ion beam energy measurement. The flexibility on accessing all the electrical and mechanical tiny components make the RFEA design unique in its class. Anomaly in triple Langmuir probe electron temperature measurement is resolved and compared the electron temperature measurement by the three variants (single, double and triple) of Langmuir probe.

1.6 Organization of the thesis

The chapters of this thesis is organized as follows. In *chapter 2*, physics of helicon discharge is discussed and reviewed the helicon wave dispersion starting form generalized ohms law. Helicon and Trivelpiece-Gould modes are addressed. Helicon source and helical antenna design parameter, excitation of helicon wave, various RF power coupling mechanism, E-H-W transitions are presented. In *chapter 3*, details of **He**licon **eX**perimental **(HeX)** system and the implemented diagnostics are discussed. Quantitative discussion on RF shielding effectiveness with different material is presented. Plasma diagnostics be it magnetic and electric probes with data analysis techniques are discussed. Comparison of three variants of Langmuir probe measurement and the technical issues are addressed. *Chapter 4* deals with the results of direct observations of transition from single to multiple axial potential structures (MAPS) formation. In *chapter 5*, the localized electron heating away from the helical antenna and the downstream density rise are presented. The helicon wave with electron interaction in connection with the localized electron heating is discussed. Pressure and energy balance models are prepared to establish the downstream density rise. In *chapter 6*, downstream annular plasma formation is presented in connection with the presence and absence of axial potential structure. Presence of tail electrons and the independent role of magnetic and geometric aperture are discussed, followed by thesis conclusion in *chapter 7*.

2

Physics of helicon discharge

2.1 Introduction

Theory of helicon wave has steadily evolved over the past several decades. The root of finding the theory of plasma waves in an unbounded uniform magnetic field system, which results in the cold plasma dispersion relation. This simple cold plasma wave theory graphically presented in the form of a Clemmow-Mullaly-Allis (CMA) diagram. Helicon waves are commonly known as bounded whistler waves which propagate in free space. Starting from the cold plasma wave, when collisional effects and finite electron mass are considered, the internal plasma fields reveal a secondary wave branch called the Trivelpiece-Gould mode. Several groups have considered more elaborate theories such as incorporating ion mass effects, wave propagation based on radially localized modes [59, 60], non-uniform density distribution etc [49, 51].

Helicon waves are cylindrically bounded low-frequency whistler waves and propagate between the ion cyclotron (ω_{ci}) and electron cyclotron (ω_{ce}) frequencies. The wave may have left or right circular polarization and propagates parallel or anti-parallel to an external applied magnetic field. Several treatments of helicon waves are found in these literatures [9, 40, 51, 58, 71, 72]. This chapter presents a literature review of the physics of helicon discharge, wave propagation in the physical limits which are relevant to the application under consideration, and modes of RF power coupling.

The rest of this chapter is organized as follows: section 2.2 discussed about the generalized helicon wave dispersion considering electron inertia and the electrostatic Trivelpiece Gould mode. Section 2.3 discussed the design principle of helicon plasma source antenna and wave field profiles. Quantitative discussion on helicon antenna and source chamber dimensions are carried out in section 2.4. Power coupling mechanisms are discussed in section 2.5.

2.2 Helicon wave physics

Cold plasma is one in which the thermal speeds of the particles are much smaller than the phase speeds of the waves. Plasma parameters can change the operational modes within plasma, which makes diversity in the subject of plasma waves, often called as “plasma wave zoo”. Magnetized plasma is a typical anisotropic medium for electromagnetic waves and can support various kinds of waves. Since plasma consists of light electrons and heavy ions, characteristic frequencies range from low frequency ion cyclotron frequency to high frequency electron cyclotron frequency. Important characteristic feature of waves in plasma is that they are subject to damping even in the absence of particle collisions. The collision-less wave damping plays important roles in plasma heating and current drive which can be effectively used in further raising the temperature of a plasma already having a temperature high enough so that collisional Joule heating is ineffective. A general fluid description method considering both species ions and electrons will be presented for waves in collision-less, magnetized plasma. Cold plasma wave equations are simply the ion and electron equations of continuity and the motion in the electromagnetic fields, which govern with Maxwell’s equations and force equation.

2.2.1 Dispersion relation

The helicon wave dispersion relationship is derived from first principles in the most direct manner for the cold plasma with plane wave approximation in this section. Equilibrium quantities are here-on denoted with a subscript (e.g. B_0). Wave perturbed quantities is of the form $e^{i(m\theta+kz-\omega t)}$, representing wave patterns that rotate in the clockwise ($m > 0$) or counterclockwise ($m < 0$) direction in time at a given position Z, viewing towards the B_0 direction in a cylindrical geometry. Maxwell's equations take on the following linearized form to derive the helicon wave dispersion.

$$\nabla.\mathbf{B} = 0 \tag{2.1}$$

$$\nabla \times \mathbf{E} = i\omega\mathbf{B} \tag{2.2}$$

$$\nabla \times \mathbf{B} = \mu_0 J - i\mu_0\omega\epsilon_0\mathbf{E} \tag{2.3}$$

Plasma current density neglecting small ion current density is given by

$$\mathbf{j} = -en_0\mathbf{v_e} \tag{2.4}$$

where, plasma quasi-neutrality implies that $n_0 \approx n_e \approx n_i$. $\mathbf{v_e}$ is the electron velocity (equation 2.4) can be found using the following electron fluid equation (2.5).

$$n_0 m_e \frac{\partial \mathbf{v_e}}{\partial t} = -n_0 e[\mathbf{E} + \mathbf{v_e} \times \mathbf{B_0}] + n_0 m_e \nu \mathbf{v_e} + \nabla P \tag{2.5}$$

The collision term $(-n_0 m_e \nu v_e)$ is neglected for the time being; it may be accounted for at any time by replacing the electron mass with an effective mass $m^* = m_e(1 + i\frac{\nu}{\omega})$ as usual way. The nonlinear pressure term ∇P in equation (2.5) can be expanded using the ideal gas law $\nabla P = \nabla n_0 KT_e$. In helicon plasma $KT_e \sim 5$eV, while typical antenna wave potentials are well in excess of 100V; then KT_e is small in comparison to the eE term in equation (2.5). The pressure term is negligible in the limit of a cold plasma. The linearized electron fluid equation simplifies to the equation (2.6).

$$- in_0 \omega m_e \mathbf{v_e} = -n_0 e[\mathbf{E} + \mathbf{v_e} \times \mathbf{B_0}] \tag{2.6}$$

which is then converted with current density (j) equation using equation (2.4) to find the wave electric field.

$$\mathbf{E} = -\frac{B_0}{en_0}\{i\frac{\omega}{\omega_{ce}}\mathbf{j} - (\mathbf{j} \times \hat{Z})\} \tag{2.7}$$

In helicon mode of plasma operation, capacitive coupling is very weak, therefore the displacement current ($-i\mu_0\omega\epsilon_0\mathbf{E}$) in equation (2.3) can be neglected. Equation (2.2), (2.3) and (2.7) are now the three governing equation for helicon wave dispersion. Substituting current (j) from equation (2.3) for helicon mode discharge ($\mathbf{j} = \frac{\nabla\times\mathbf{B}}{\mu_0}$) in equation (2.7).

$$i\omega\mathbf{B} = -\frac{B_0}{en_0\mu_0}[i\frac{\omega}{\omega_{ce}}\nabla \times (\nabla \times \mathbf{B}) - \{(\nabla \times \mathbf{B}) \times \hat{Z}\}] \tag{2.8}$$

Application of vector identity and using equation (2.1),

$$\begin{aligned}
\{(\nabla \times \mathbf{B}) \times \hat{Z}\} &= (\nabla \times \mathbf{B})(\nabla \cdot \hat{Z}) - \hat{Z}\{\nabla \cdot (\nabla \times \mathbf{B})\} \\
&\quad + (\hat{Z} \cdot \nabla)(\nabla \times \mathbf{B}) - \{(\nabla \times \mathbf{B}) \cdot \nabla\}\hat{Z} \\
&= (\hat{Z} \cdot \nabla)(\nabla \times \mathbf{B}) \\
&= ik(\nabla \times \mathbf{B})
\end{aligned} \tag{2.9}$$

The vector equation for $\mathbf{B}$ can be written as

$$i\omega\mathbf{B} = -\frac{B_0}{en_0\mu_0}\{i\frac{\omega}{\omega_{ce}}\nabla \times (\nabla \times \mathbf{B}) - ik(\nabla \times \mathbf{B})\} \tag{2.10}$$

$$\Rightarrow \frac{\omega}{\omega_{ce}}\nabla \times (\nabla \times \mathbf{B}) - k(\nabla \times \mathbf{B}) + \frac{en_0\mu_0}{B_0}\omega\mathbf{B} = 0 \tag{2.11}$$

This 2^{nd} order differential equation of Bessel kind can be written as

$$(\beta_1 - \nabla\times)(\beta_2 - \nabla\times)\mathbf{B} = 0 \tag{2.12}$$

$$\frac{\omega}{\omega_{ce}}\beta^2 - k\beta + \frac{en_0\mu_0\omega}{B_0} = 0 \tag{2.13}$$

where, β_1 and β_2 are the roots of the following quadratic equation (2.14) and β is the total wave number, which is discussed in the next section.

$$\frac{\omega}{\omega_{ce}}\beta^2 - k\beta + k_W^2 = 0 \tag{2.14}$$

where $k_W = \sqrt{\frac{\omega n_0 \mu_0 e}{B_0}} = \frac{\omega}{\omega_{ce}}\frac{\omega_P^2}{c^2} = \delta\frac{\omega_P^2}{c^2}$ is the Whistler wavenumber in free space and ($\delta = \frac{\omega}{\omega_{ce}}$) is the skin depth, ω_P is the plasma oscillation frequency.

2.2.2 Helicon and Trivelpiece-Gould mode

In free space, whistler waves are right circularly polarized electromagnetic waves. Whistler wave dispersion in a bounded magnetized system allows existence of long-wavelength helicon together with short-wavelength TG mode. Trivelpiece-Gould (TG) mode in helicon plasma has also been experimentally observed [38].

Solution of the equation (2.14) are

$$\beta_{1,2} = \frac{k\omega_{ce}}{2\omega}(1 \pm (1 - \frac{4\omega}{\omega_{ce}}\frac{k_W^2}{k^2})^{1/2}) \tag{2.15}$$

$$\beta_{1,2} = \frac{k}{2\delta}(1 \pm (1 - \frac{4\omega}{\omega_{ce}}\frac{k_W^2}{k^2})^{1/2}) \tag{2.16}$$

The two roots in equation (2.16) are well separated when the axial helicon wavelength in the plasma ($\sim$ few cm) is small in comparison to the free space whistler wavelength ($\lambda_W = \frac{2\pi}{k_W} \sim$ few meter) for all frequencies of interest; in this limit ($\frac{\omega k_W^2}{\omega_{ce}k^2} = \frac{\delta k_W^2}{k^2} << 1$) equation (2.16) can be written as

$$\beta_1 = \frac{k}{2\delta}\{1 - 1 + \frac{2\omega}{\omega_{ce}}\frac{k_W^2}{k^2}\} \tag{2.17}$$

$$\Rightarrow \beta_1 = \frac{k_W^2}{k} \tag{2.18}$$

and

$$\beta_2 = \frac{k}{2\delta}\{1 + 1 - \frac{2\omega}{\omega_{ce}}\frac{k_W^2}{k^2}\} \tag{2.19}$$

$$\Rightarrow \beta_2 = \frac{k}{\delta} = \frac{k\omega_{ce}}{\omega} \tag{2.20}$$

where, β_1 root corresponds to the helicon wave whereas β_2 root is associated with electrostatic electron cyclotron waves called Trivelpiece-Gould modes, usually referred to as TG-waves [51]. The corresponding wave solutions even for low or moderate magnetic fields ($B_0 \sim 100G$) RF frequency $f = 13.56$MHz, in Argon plasma $\delta = \frac{\omega}{\omega_{ce}} \sim 0.1$. In this magnetic field β_2 approaches higher value (equation 2.20) and the total wave solution is essentially for a pure helicon wave. The $k - \beta$ diagram in figure (2.1) is showing the existence and separation of helicon and TG mode. Where, k is the axial wavenumber and β is the total wavenumber. To plot the $k - \beta$ diagram the equation (2.14) has been simplified in equation (2.24).

$$k = \delta\beta + \frac{k_W^2}{\beta} \tag{2.21}$$

$$k = \delta\beta + \delta\frac{\omega_P^2}{c^2\beta} \tag{2.22}$$

$$k = \frac{\delta}{\beta}\{\beta^2 + \frac{\omega_P^2}{c^2}\} \tag{2.23}$$

$$k = \frac{(\omega/\omega_{ce})}{\beta}\{\beta^2 + \frac{\omega_P^2}{c^2}\} \tag{2.24}$$

The $k - \beta$ diagram for various axial magnetic fields are plotted in figure (2.1) using helicon dispersion equation (2.24).

The $k - \beta$ diagram shows there is a lower bound on the axial wavenumber (k) for any set of fixed physical parameters. Solving the characteristic equation (2.16) for β and differentiating with respect to k yields a minimum axial wavenumber

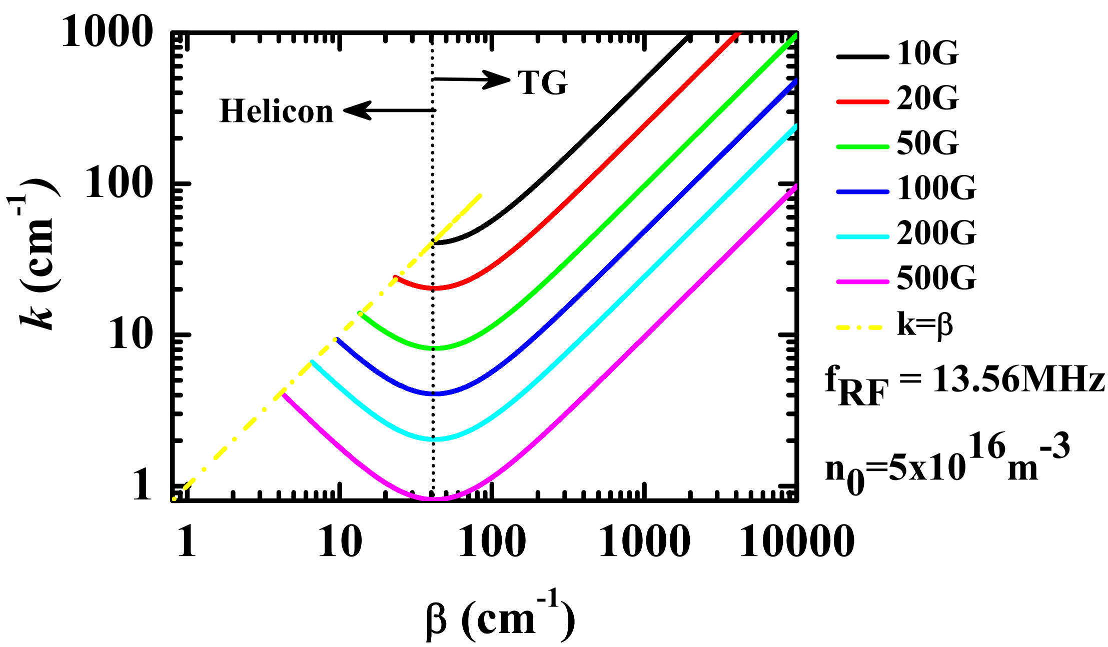

Figure 2.1: Helicon wave dispersion plots for various magnetic fields from 10G to 500G, keeping the driving frequency f_{RF} = 13.56MHz and density n_0 = $5 \times 10^{16} m^{-3}$. The vertical dot line shows the minimum point along the vertical axis (which is the minimum of axial wavenumber). The curve at left side of this dot line represents the helicon wave branch and the right side is the TG wave branch. Yellow dash dot line is $k = \beta$ line, which corresponds to pure helical (no perpendicular wave vector is there). The solution on the left side of this yellow line does not exist.

k_{min} equation (2.25).

$$k_{min} = 2k_W\sqrt{\delta} \tag{2.25}$$

Figure (2.1) clearly shows this k_{min} in the $k-\beta$ diagrams for different the magnetic fields. With decreasing magnetic fields the helicon wave branch is reduced since it is approaching towards electron cyclotron resonance (ECR) frequency (ω_{ce}), at $\sim$ 5G magnetic field for 13.56MHz RF source. Therefore, helicon waves in laboratory plasma has been studied mostly at high magnetic field to get broader helicon regimes in the dispersion plot. The equation (2.25) can be expressed as

$$k^2_{min} = 4\frac{\omega^2}{\omega^2_{ce}}\frac{\omega^2_P}{c^2} \tag{2.26}$$

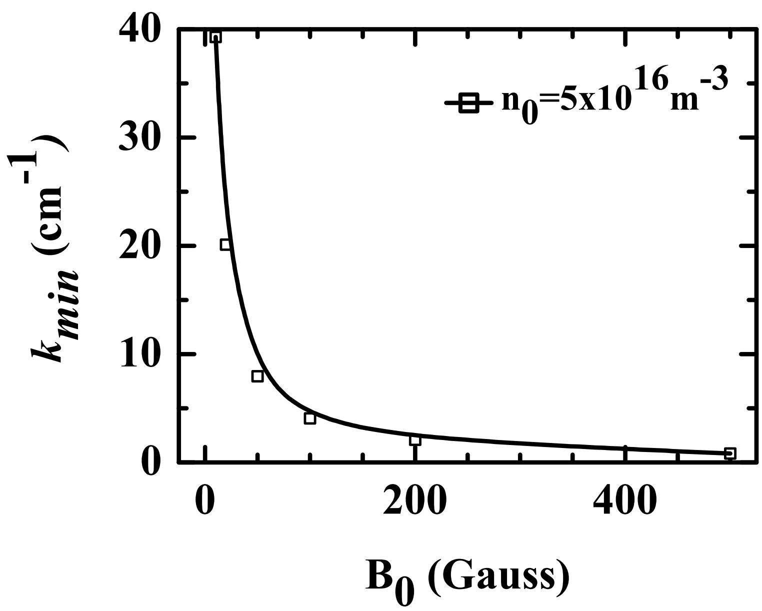

Figure 2.2: k_{min} with B_0 keeping a fixed density corresponding to figure (2.1)

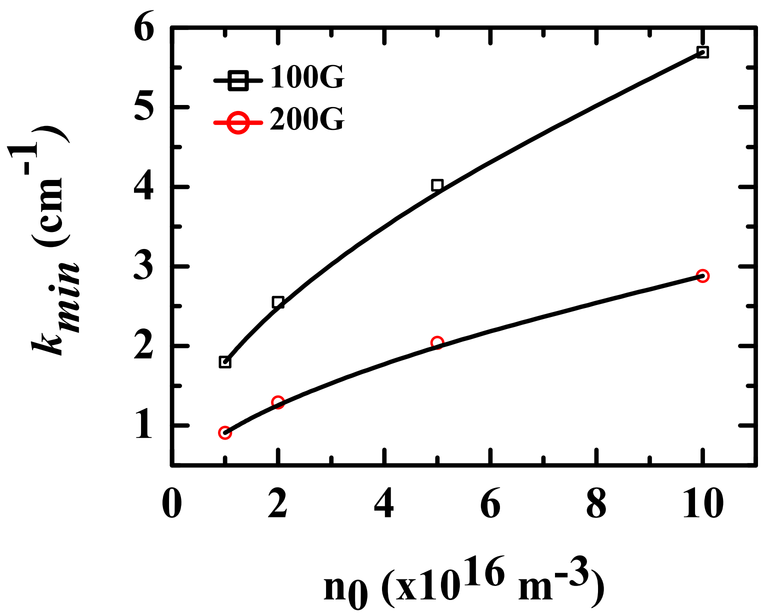

Figure 2.3: k_{min} with density keeping the magnetic field B_0 constant.

$$\Rightarrow k_{min}B_0 = \frac{2\omega\omega_P m_e}{ec} \tag{2.27}$$

For a fixed axial density (by monitoring input RF power) with increasing axial

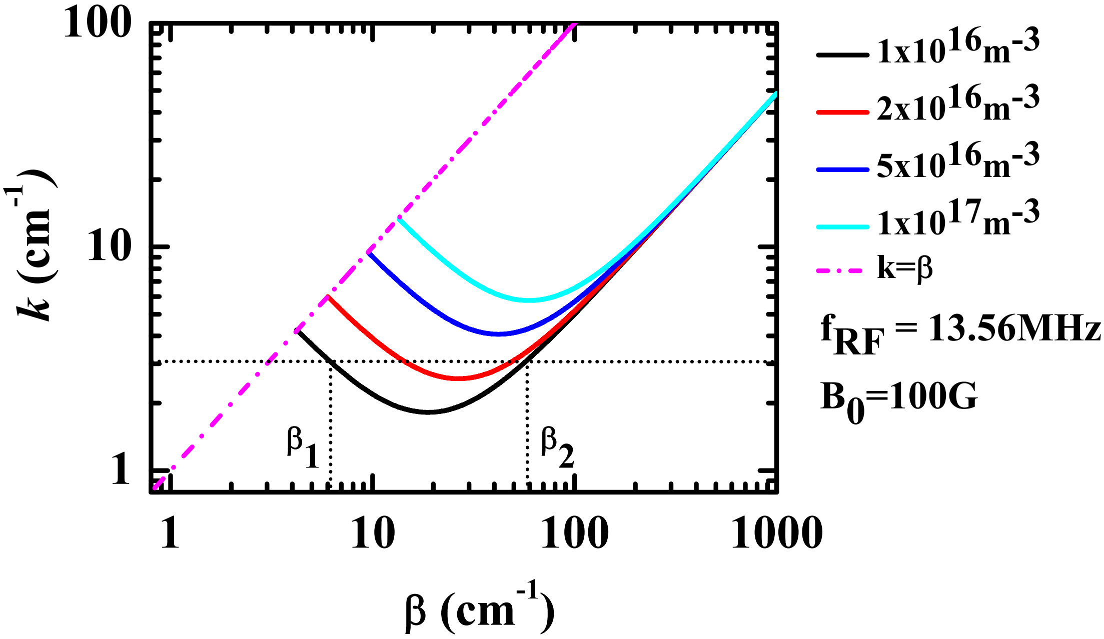

Figure 2.4: Helicon wave dispersion for various density keeping driving frequency 13.56MHz and equilibrium magnetic field ($B_0 = 100G$). The horizontal line shows the two roots β_1 and β_2 for same axial wave number (k).

magnetic field; k_{min} will follow the rectangular hyperbolic trained (equation 2.27) for a fixed frequency RF source, which is indicated in figure (2.2). On the other way, equation (2.26) can be written as the following form

$$k_{min} = \frac{2\omega}{\omega_{ce}} \frac{e\sqrt{m_e}}{\epsilon_0} \sqrt{n_0} \tag{2.28}$$

where for a fixed magnetic field (B_0) with increasing plasma density by rising input RF power, k_{min} will follow the parabolic nature (equation 2.28) for a fixed frequency source as indicated in figure (2.3). Helicon wave dispersion plots for different plasma densities with two different magnetic fields 100G and 200G respectively are shown in figure (2.4) and (2.5). Existence of two roots β_1 and β_2 are also indicated in these plots; where the lower wavenumber (β_1) corresponds to the helicon wave branch and higher wavenumber (β_2) corresponds to TG- wave

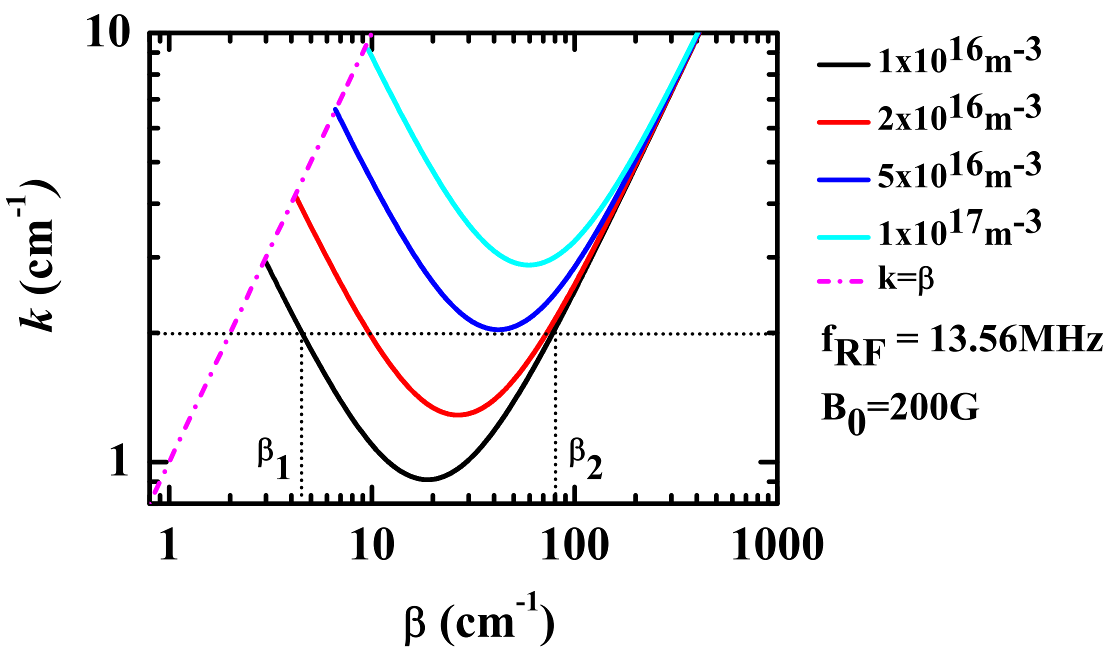

Figure 2.5: Helicon wave dispersion for various density keeping driving frequency 13.56MHz and equilibrium magnetic field ($B_0 = 200G$). The horizontal line shows the two roots β_1 and β_2 for same axial wave number (k).

branch. β is the total wave number defined as

$$\beta = \sqrt{k^2 + k_\perp^2} \tag{2.29}$$

where, $k_\perp$ is the perpendicular wave vector. The effect of the boundaries come from the radial size of the plasma chamber and the root corresponding to lower β (β_1 root) has lower $k_\perp$ or higher $\lambda_\perp$ compared to it's parallel component. On the other hand for higher β (β_2 root) has higher $k_\perp$ or lower $\lambda_\perp$ compared to it's parallel component which is indicated in figure (2.4) and (2.5).

2.3 Helicon wave fields

The above most generalized case where wave damping due to collisional or Landau damping is considered and axial electric field (E_z) arises to move electrons in the

$+z$ direction. This is taken into consideration in the j_z component of the plasma current for motion parallel to the B_0 field. When this is considered, the governing equation (2.5) replacing the electron mass with effective mass $m^* = m_e(1 + i\frac{\nu}{\omega})$ commonly known as generalized Ohm's law for wave dispersion, which is discussed in the previous section. However, for the purpose of designing antenna and plasma source density parameters, one can choose the simplest case of bounded collision-less, uniform density plasma of radius (a) and uniform density distribution $n(r) \sim n_0$, subject to an axial magnetic field B_0 in the $+z$ direction. Starting again from Maxwell's equations (2.2) and (2.3) neglecting the displacement current for helicon mode discharge as discussed before the wave dispersion is derived. In that case one more assumption is taken that the entire plasma current is carried by the $\mathbf{E} \times \mathbf{B}$ motion of the electrons where the driving frequency (ω) is much smaller than the electron cyclotron frequency (ω_{ec}) ($\omega << \omega_{ec}$) and is much larger than the lower hybrid frequency ($\omega_{LH} = \sqrt{\omega_{ce}\omega_{ci}}$), ($\omega >> \omega_{LH}$) such that ion motions can also be neglected, the generalized Ohm's law (equation 2.5) expression now be reduced to equation (2.30).

$$en_0\mathbf{E} = \mathbf{j} \times \mathbf{B_0} \tag{2.30}$$

It is also assumed that the resistivity ($\eta \sim 0$) is zero, where η is defined by $\eta = \frac{m_e \nu_{ei}}{n_0 e^2}$. Returning to Maxwell's equations (2.2), (2.3) and Ohm's law (2.30) with 1^{st} order wave perturbations of the form $e^{i(m\theta + kz - \omega t)}$, as mentioned before we have

$$i\omega\mathbf{B} = \nabla \times \mathbf{E} = \frac{1}{en_0}\{\nabla \times (\mathbf{j} \times \mathbf{B_0})\} \tag{2.31}$$

$$i\omega\mathbf{B} = \frac{1}{en_0}\{(\mathbf{B_0}.\nabla)\mathbf{j}\} = \frac{ikB_0}{en_0}\mathbf{j} \tag{2.32}$$

$$\mathbf{j} = \frac{\omega}{k}\frac{en_0}{B_0}\mathbf{B} \tag{2.33}$$

Substituting in equation (2.34)

$$\nabla \times \mathbf{B} = \mu_0 \mathbf{j} \tag{2.34}$$

$$\mathbf{j} = \frac{1}{\mu_0}\nabla \times \mathbf{B} = \frac{\omega}{k}\frac{en_0}{B_0}\mathbf{B} \tag{2.35}$$

$$\Rightarrow \mathbf{B} = (\frac{\omega}{k}\frac{\mu_0 n_0 e}{B_0})^{-1}\nabla \times \mathbf{B} \tag{2.36}$$

$$\Rightarrow \alpha\mathbf{B} = \nabla \times \mathbf{B} \tag{2.37}$$

where, α is defined as equation

$$\alpha = \frac{\omega}{k}\frac{\mu_0 n_0 e}{B_0} = \frac{k_W^2}{k} \tag{2.38}$$

which can be expressed in-terms of the electron plasma frequency (ω_P) and cyclotron frequency (ω_{ce})

$$\alpha = \frac{\omega}{k}\frac{\omega_P^2}{\omega_{ce}c^2} \tag{2.39}$$

α is defined as the total wave number, similar to β for the generalized case. This equation (2.39) is exactly same as for right handed whistler wave propagation in free space. Taking the curl of equation (2.37) yields a second order differential equation (2.40) for the plasma wave fields.

$$\nabla^2\mathbf{B} + \alpha^2\mathbf{B} = 0 \tag{2.40}$$

Substituting equation (2.37) into equation (2.34) indicates

$$\mathbf{j} = \frac{\alpha}{\mu_0}\mathbf{B} \tag{2.41}$$

that the current is parallel to the wave magnetic field; all three components of both $\mathbf{j}$ and $\mathbf{B}$ are important. The z-component of equation (2.40) in cylindrical coordinates can be expressed as

$$\frac{\partial^2 B_z}{\partial r^2} + \frac{1}{r}\frac{\partial B_z}{\delta r} + (T^2 - \frac{m^2}{r^2})B_z = 0 \tag{2.42}$$

where the transverse wave number T or $k_{\perp}$ is defined as

$$T^2 = \alpha^2 - k^2 \tag{2.43}$$

The differential equation (2.42) is Bessel's equation subject to the finite boundary condition [40] at the origin so that the z- component solution is

$$B_z(r) = CJ_m(Tr) \tag{2.44}$$

The r and θ components of the wave magnetic fields are obtained from equation (2.37) as

$$im\frac{B_z}{r} - ikB_\theta = \alpha B_r \tag{2.45}$$

$$ikB_r - \frac{\partial B_z}{\partial r} = \alpha B_\theta \tag{2.46}$$

Solving for B_r and B_θ in terms of B_z and $\frac{\partial B_z}{\partial r}$ and substituting for B_z, from equation (2.44), we have

$$B_r(r) = \frac{iC}{T^2}[\frac{m\alpha}{r}J_m(Tr) + k\frac{\partial J_m(Tr)}{\partial r}] \tag{2.47}$$

$$B_\theta(r) = -\frac{C}{T^2}[\frac{mk}{r}J_m(Tr) + \alpha\frac{\partial J_m(Tr)}{\partial r}] \tag{2.48}$$

Where m is the azimuthal mode number. Using the following Bessel recurrence relation (2.49) and (2.50)

$$\frac{m}{r}J_m(Tr) = \frac{T}{2}\{J_{m-1}(Tr) + J_{m+1}(Tr)\} \tag{2.49}$$

$$J_m^{'} = \frac{T}{2}\{J_{m-1}(Tr) - J_{m+1}(Tr)\} \tag{2.50}$$

above B_r and B_θ equations take the following simplified form.

$$B_r = \frac{iC}{2T}\{(\alpha + k)J_{m-1}(Tr) + (\alpha - k)J_{m+1}(Tr)\} \tag{2.51}$$

$$B_\theta = -\frac{C}{2T}\{(\alpha + k)J_{m-1}(Tr) - (\alpha - k)J_{m+1}(Tr)\} \tag{2.52}$$

The boundary condition for the simplest helicon wave in this case is $B_r(r = a) = 0$ at the radius $(r = a)$ of the source chamber. To satisfy this boundary condition the necessary density $n_0 \sim 6.5 \times 10^{16} m^{-3}$, 18 cm half wave right helical antenna corresponds to axial wave number $k = 17.44 m^{-1}$ with our 13.56 MHz RF at 100G are taken. Final solution of each components of helicon wave fields B_z, B_r and B_θ obtained by using this boundary condition are shown in figure (2.6).

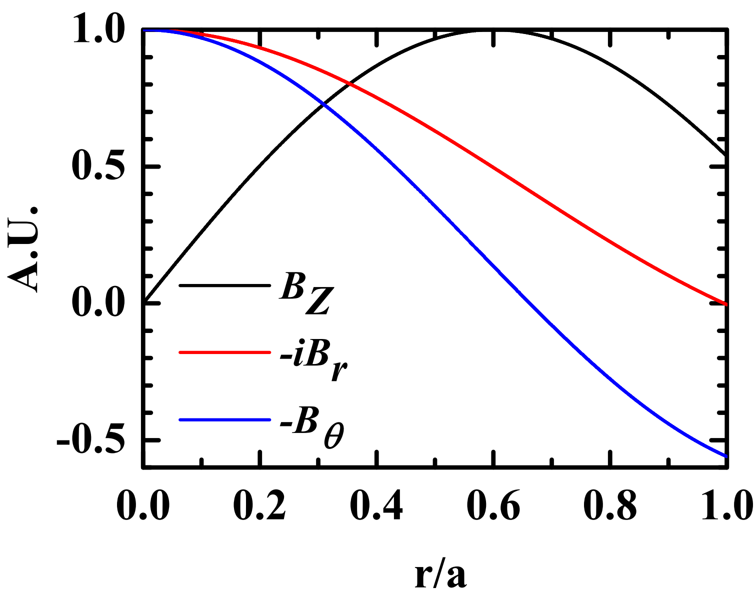

Figure 2.6: Radial profiles of the helicon wave magnetic field components for $m = +1$ mode.

2.4 Helicon wave excitation

Helicon waves are normally excited with the use of several antenna configurations. Helical antenna design parameter optimization (diameter 2a = 15cm, axial length l = 18cm) based on the calculation given by Chen et al. [40]. Various option for helicon wave excitation and antenna design has been studied [40]. To excite the helicon wave, Nagoya antenna, Boswell type antenna, Helical antenna are very common for producing plasma in a linear machine [51]. The discussion in the previous section provides an overview of the physics and wave propagation, but it does not incorporate all the practical problems of relevant physics. Plasma source efficiency, electron interaction with helicon wave, electron and ion heating, cause of potential structure formation, power distributions, asymmetries between modes etc are some of the topics pursued currently. For instance, it has been experimentally demonstrated that the $m = +1$ mode is potentially excited or it is the major contributor to mode contents by helical antenna. Furthermore, it has been shown that the $m = +1$ mode achieves a higher peak density than its counterpart $m = -1$ [51] and has a lower power threshold for high-density helicon mode operation [71]. It is desirable for these reasons to design an antenna which efficiently couples with the $m = +1$ mode. This is achieved by using a geometry that closely matches the form of that mode in space. One such possibility is the right handed half-helical antenna, shown in figure (2.7). It is denoted a half-helical antenna since the each helical arms rotate by 90^0 to connect with respective rings, with respect to their origin. Hence total 180^0 phase difference between two rings at any instant. The helicity sense of a helical antenna determines the antenna type. The antenna is called right helical as the twist to the horizontal Cu strip is in the counterclockwise direction when the observer moves in the direction of k. Therefore it can excite $m = +1$ mode when k and the external magnetic field (B_0) are parallel along $(+)Ve\ Z$ direction (from right to left of figure 2.7). However, by reversing the direction of external magnetic field i.e along $(-)Ve\ Z$ direction, same antenna can excite $m = -1$ mode. Experiments presented in this thesis are carried out in right helical antenna configuration to excite $(m = +1)$ mode.

The aforementioned condition (2.18) or (2.38) for helicon mode shows the dependence of equilibrium density (n_0) to the source radius (a).

$$\beta_1 = \frac{k_W^2}{k} = \frac{\omega n_0 \mu_0 e}{B_0 k} = \frac{3.83}{a} \tag{2.53}$$

where the symbols have their usual meanings and the numerical factor is just the first zero of $J_{m=+1}$, corresponding to the lowest radial mode. The lowest radial mode is chosen since one would expect a low-order solution to be the dominant

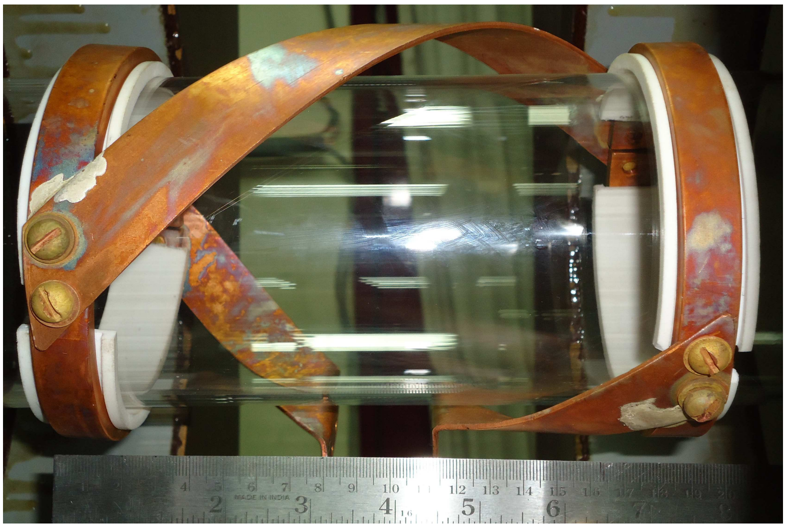

Figure 2.7: Picture of installed half wave right helical antenna.

contribution to the total solution. The density (n_0) and source radius (a) are inversely proportional when all other parameters are fixed (equation 2.53). The azimuthal mode of our interest is the $m = +1$ since it has been experimentally demonstrated that this mode is preferentially more efficient for wave excitation over $m = -1$ [51].

The antenna length determines the axial wavenumber k just as the rotational symmetries set by the azimuthal wavenumber to be launched. For design purposes, it is sufficient to neglect k^2 relative to T^2 in equation (2.43) and let $\alpha \sim T$. The dispersion relation, equation (2.38), then becomes

$$\frac{\omega}{k} = \frac{TB_0}{\mu_0 n_0 e} \tag{2.54}$$

where T is given by the approximate boundary condition $J_1(Ta) \sim 0$ (equation 2.44) for $m = +1$ modes to be zero at the boundary, yields

$$T = \frac{3.83}{a} \tag{2.55}$$

The first step is to choose the tube radius a and the phase velocity $\frac{\omega}{k}$. If $\frac{\omega}{k}$ is chosen to be near electron thermal velocity (v_{th}), the wave will be strongly damped by Landau damping. On the other hand, in helicon sources primary electrons are directly accelerated via wave-particle interactions. In that case, one would choose $\frac{\omega}{k}$ to be near the velocity of the ionizing electrons. The expression relating the axial wavelength to the energy of fast primaries is simply

$$\frac{1}{2}m_e(\frac{\omega}{k})^2 = eE_i \tag{2.56}$$

where E_i is the energy in volts. For the case of a half helical antenna, the antenna length corresponds to one-half the axial wavelength, thus the expression relating antenna length (l_A) to axial wave length k is

$$l_A = \frac{\lambda_z}{2} = \frac{\pi}{k} \tag{2.57}$$

Substituting k from equation (2.56) into equation (2.57), we have

$$l_A = \frac{\pi}{k} = \frac{\pi}{\omega}[\frac{2eE_i}{m_e}]^{1/2} \tag{2.58}$$

The most common case of discharges in Argon, which has a peak in the ionization cross section at $E_i \sim 50 - 70$V, for which the antenna length is found to be $\sim 16 - 18$cm using equation (2.58 and we kept our helical antenna length 18cm, which is shown in figure (2.7).

It has been experimentally demonstrated that the energy absorption rate is several orders of magnitude larger than what one would expect from collisional damping alone [9]. Initially Landau damping and later energy absorption via mode conversion at the boundary to Trivelpiece-Gould waves were proposed as potential damping mechanisms to account for the discrepancy [40, 58, 72]. It has been theoretically shown that the the energy absorption spectrum in k is significantly altered when one includes Trivelpiece Gould modes in antenna loading calculations. In that case the power absorption profile was shown to be hollow with most of the energy absorbed near the boundary. The absorption spectrum had a peak at k

corresponding to primary electron energies in the range $10 - 100$eV for Argon; that peak increased and broadened with density [72].

In case of low density plasmas bellow $5 \times 10^{18} m^{-3}$, Chen et al. have suggested Landau damping as the dominant mechanism for energy transfer from helicon wave to plasma electrons [40] [56]. Helicon antenna produced helicon waves have been experimentally demonstrated the power absorption mechanism via Landau damping wave particle interaction [56]. Kamori et al. have experimentally shown helicon wave phase velocity measurements, which qualitatively supported the Landau damping hypothesis in low density helicon plasmas [56]. However, Keiter et al. have argued that Landau damping may not be the a viable candidate for electron energization in their high density helicon plasmas [57]. Couple of years later, Chen at al. reported that Landau damping mechanism is incapable of producing sufficient ionization to account for the high densities produced in helicon plasmas [58]. However, in this same paper they acknowledged that for very low density plasmas, Landau damping can still be a source of heating and density production.

2.5 Power coupling

Radio frequency (RF) power transfer mechanism and its efficient way of power coupling is also another subject in this field, which has been studied from the last four decades for producing efficient high density plasma source. Principle is to introduce an RF current to a coil/antenna, where the changing magnetic field associated with the coil/antenna current induces an electromagnetic field in the similar way of transformer action. Depending on the coupling mechanism of the RF fields to the plasma, the discharge has been classified into three modes. Electrostatic coupling of RF power with the plasma is called E-mode and electromagnetic coupling of RF power with the plasma is called H-mode. In presence of external static magnetic field, these electromagnetic disturbances can propagate at low frequencies (compared to electron plasma frequency: ω_p) and charge particles can absorb energy via wave coupling, called W-mode [36].

There are many ways to generate RF electromagnetic fields for instance by applying an RF voltage across two parallel electrodes or by circulating RF currents in coils or antennas, either immersed in the plasma or separated from it through a dielectric window. The electromagnetic fields will couple to the electrons in the plasma and transfer energy to sustain the plasma. The efficiency with which power is transferred to the electrons from the power supply and the plasma uniformity both strongly depend on the design of the RF antenna. For industrial application purpose there are two classical RF reactors which commonly used for plasma processing purpose are the capacitively coupled plasma (CCP) and inductively coupled plasma (ICP) reactors. In the industry, inductively coupled plasma (ICP) systems are often use two power supplies, which provides independent control over density production and ion energy into the wafer. The first drives a coil, usually external to the plasma and separated from it by a dielectric window. The RF current flowing in the coil launches an evanescent disturbance that decays over a distance of a few centimeters into the plasma. This induces RF current in the plasma and transfers energy to electrons; i.e., it controls the plasma density. Another one biased to the wafer electrode for material processing to control the ion energy deposition. On the other hand, in CCP discharge, the coupling efficiency is markedly higher than in the single-frequency CCPs, which enables to get higher plasma density, of the order of $10^{16} - 10^{18} m^{-3}$. These two different reactor families, CCPs and ICPs, are usually associated with two regimes, called E (electrostatic) mode for capacitive coupling and H (electromagnetic) mode for inductive coupling. Inductive reactors with an external coil generally start in the E-mode and undergo an E-H transition when the plasma density reaches a critical level as power to the coil is increased. A third regime that couples energy from the RF fields to the plasma, called W -mode for wave coupling and electron densities are found to be higher than those observed in typical CCP and ICP discharges. Radio frequency disturbances do not propagate for CCP or ICP discharges in the absence of a static external magnetic field. However, adding a background steady magnetic field guided the antenna driven RF disturbances in a bounded axial system and the helicon wave belongs to this category. The propagating character of the wave implies that heating penetrates deeper in the plasma than inductive heating (localized in the skin depth (δ)) or capacitive heating (mostly localized in the RF sheaths) [36]. Wave coupling discharge achieves high ionization efficiency in large plasma volumes or long plasma columns. The helicon wave which propagates away from the antenna into the bulk plasma where the wave energy is absorbed by electrons. The coupling of energy in the W-mode achieves densities above $10^{19}m^{-3}$ and in larger volumes than can be achieved by an H-mode in ICP. Helicon reactors have therefore been used for plasma processing applications demanding high ion fluxes. They are very promising for high degree of ionization. Which has application in plasma thrusters because of their ability to produce highly ionized plasmas. Since the antenna is excited by an RF voltage, helicon plasmas may also operate in capacitive (E) mode at low power. In addition, the RF current flowing in the antenna induces fields near the antenna that tend to excite an inductive (H) mode. The H-mode usually dominates at intermediate power. The plasma eventually operates in the W-mode (where W signifies the propagating helicon wave mode) when the power is large enough to provide the required plasma density to support helicon wave propagation. Therefore, helicon plasmas are subject to E-H-W transitions. Further mode transitions are also observed within the W-mode, because of resonant wave coupling to the antenna. All these phenomena lead to abrupt variations of the electron density with the input power.

In a helicon wave produced plasma, energy is transferred from it to the plasma electrons to produce heating by collisional or collision-less mechanisms. Helicon discharges at low neutral gas pressure and moderate plasma density, the heating of electrons is predominantly by collision-less mechanisms, as the collision frequencies are too low for efficient ohmic heating of electrons. When a helicon mode passes through the plasma, charged particles are oscillated by the electric field of the wave as the disturbance moves away. The wave propagates at the phase speed, $v_\phi = \frac{\omega}{k}$, which depends on the static magnetic field and the electron density. The periodic displacement of the electron motion with the RF oscillation takes the electrons with thermal motion at speeds (v_e), under conditions $v_\phi \sim v_e$. Therefore, one can imagine that the electrons are moving at the same speed as the helicon wave in the same direction. Furthermore, electrons moving slightly faster than the wave will drive into the back edge of the crests while those moving more slowly will be swept forward by the leading edge of the crests. Although that image is a poor visualization of the interaction, it does suggest that energy could be transferred between the wave and the electrons and that the energy transfer is likely to be a function of particle velocity. So, to take this wave-particle interaction into account one must integrate the interaction over the electron velocity distribution. The most significant contributions to the result will come from those particles that have a speed close to the phase speed of the wave.

The word *mode* is used in this chapter to describe several phenomena here. Therefore, careful attention should be paid to the context in which this word is used. (i) The wave electric field rotates as it propagates, introducing an azimuthal structure to the wave fields described by a mode number m. (ii) There are transitions between the various energy coupling mechanisms: the capacitive (E) mode, the inductive (H) mode, and the helicon (W) modes. (iii) On the other way resonant coupling between the antenna and the helicon wave occurs at discrete longitudinal wavelengths (or equivalently densities). Therefore, within the W-mode, there are several longitudinal wave modes described by the mode number (W_1, W_2 etc).

3

HeX system and implemented diagnostics

3.1 Introduction

The **He**licon **eX**perimental **(HeX)** system is developed for basic studies of helicon plasma physics, current-less potential structure formation and their dynamics, ion beam generation, role of magnetic field divergence on stability determination near the throat. Several electrical and magnetic probes are developed for plasma diagnosis in this RF environment. In this chapter detail description of HeX and the necessary improvisation made on the diagnostics to make them suitable for faithful measurements in relatively low density ($\sim 10^{16} m^{-3}$) RF plasma are presented.

The rest of this chapter is organized as follows: In section 3.2 description of HeX is given which includes vacuum vessel, helical antenna, RF generator, matching network, RF shielding, grounding, axial magnetic field coils. In section 3.3 implemented plasma diagnostics is discussed, which includes high frequency magnetic probes, retarding field energy analyzer, RF compensation single Langmuir probe, double probe, triple probe, emissive probe and RF current probe.

3.2 HeX system

The Hex system composed of vacuum vessel, helical antenna, RF shielding, grounding and electromagnets. A schematic of the experimental setup is shown in figure (3.1). Detail description of each of these subsystems are described in the following subsections.

3.2.1 Vacuum vessel

The vacuum vessel is composed of two chambers. One is called plasma source chamber consists of a borosilicate glass tube of 95 mm diameter having length of 700mm in which the discharge is ignited using a helical antenna. Another one is called expansion or diffusion chamber made of stainless steel of dimensions 210 mm diameter and length 510 mm. Plasma is produced in the narrow source chamber and diffuses into the wider expansion chamber guided by the axial magnetic fields. The larger SS chamber contains numerous $40KF$ ports through which the entire plasma volume can be easily diagnosed with electric and magnetic probes. A photograph of the vacuum system indicating source and expansion chamber is shown in figure (3.2). A 1000 l/s diffusion pump backed by rotary pump is connected to the stainless steel expansion chamber (figure 3.2). The vacuum system reached upto base pressure 1×10^{-6}mbar using this diffusion pumping system. Experiments are performed using Argon gas.

3.2.2 Helical antenna

The discharge is ignited by using a right helical antenna, having 18 cm axial length, which is placed concentrically on the outer periphery of the glass source chamber. The helical antenna is made up with Cu strip of width 25mm and thickness 3mm. Helical antenna is composed of three parts to make the flexible arrangement to place it concentrically on the glass tube. Each of these parts while mounting on the glass tube in sequence is shown in figure (3.3). Horizontal mid point of this

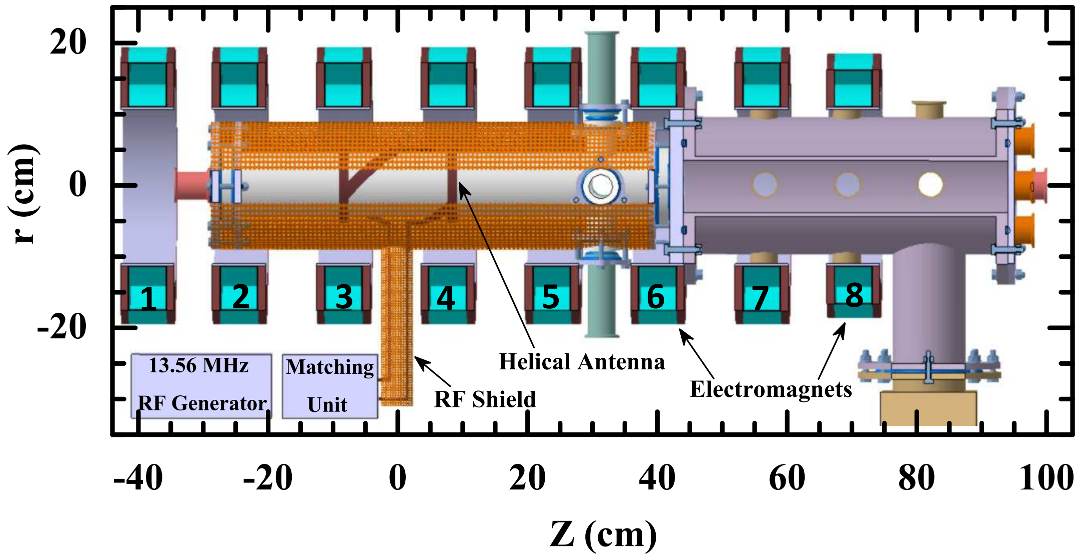

Figure 3.1: Schematic of helicon plasma experimental setup, indicating electromagnets, RF generator, matching network and RF shielding

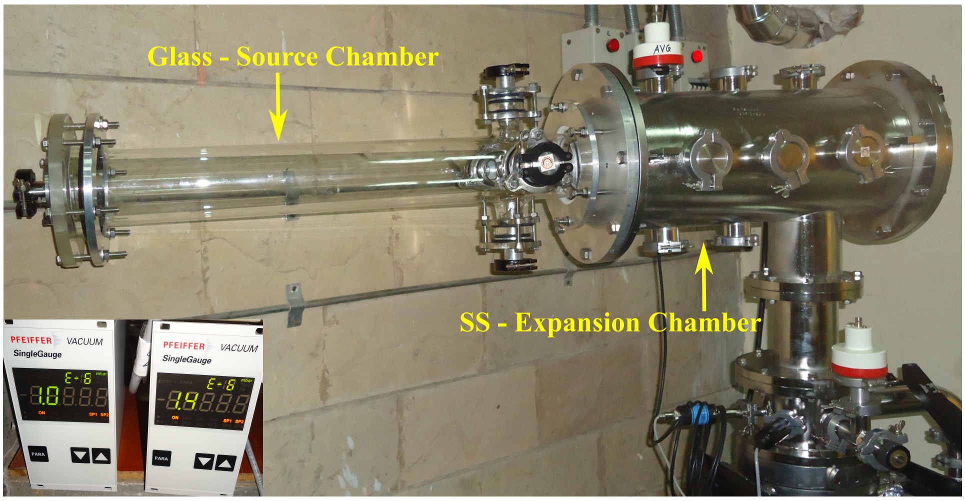

Figure 3.2: HeX vacuum system indicating glass source chamber and stainless steel expansion chamber, where diffusion pumping system is connected. Inset shows the base pressure reading of two gauges installed into the system.

antenna, concentrically with the axis of glass source tube is the reference origin for all measurement purpose.

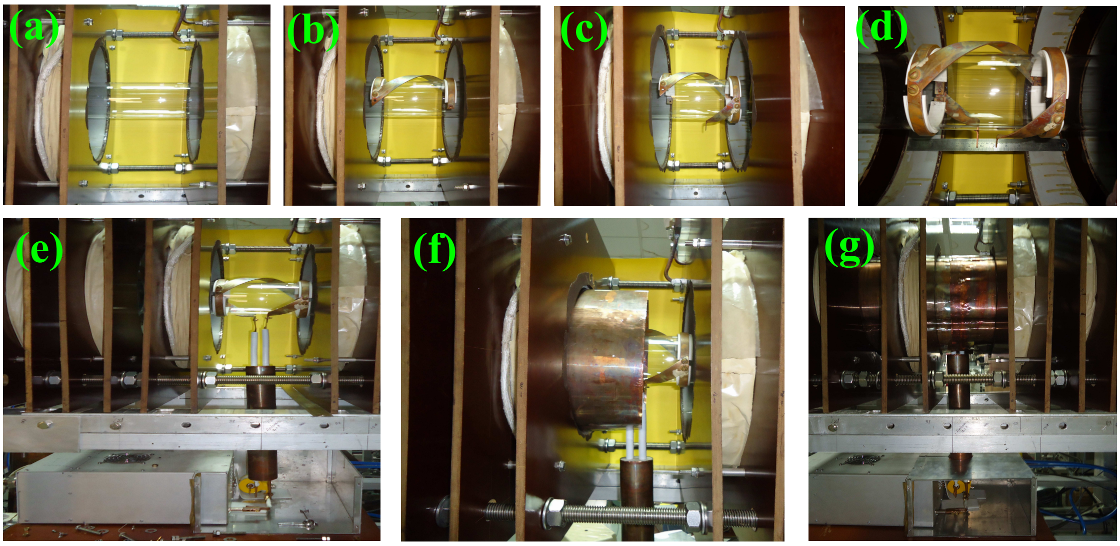

Figure 3.3: Each step of installation of helical antenna is shown. (a) is the glass source chamber where the antenna is installed. (b) One part of the helical antenna is placed, (c) second part of the antenna is connected, (d) third part of the antenna is connected, (e) helical antenna is connected to the matching network box via a transmission line, (f) Cu shielding jacket is installing, (g) antenna and associated transmission line is covered by Cu jacket.

3.2.3 RF generator and matching network

A variable power (0 to 2.5kW), 13.56 MHz RF source ($CESAR^{TM}$ Generator, Model 136, Advance Energy) with standard 50Ω output impedance is used for plasma production. However, the plasma and antenna with transmission line have impedance $\sim (\leq 2\Omega)$. Hence direct use of this RF generator for plasma production suffered itself by maximum reflected power due to impedance mismatching. Use of a matching network between the RF generator and the antenna transmission line is a common practice to reduce the reflected power by overcoming the impedance mismatch. There are different types (L-matching, Π- matching etc.) of matching networks used for impedance matching purpose. In HeX system RF power at 13.56 MHz is applied to the antenna via an L-matching network. The equivalent circuit of power transfer from RF generator to plasma load is shown in figure (3.4).

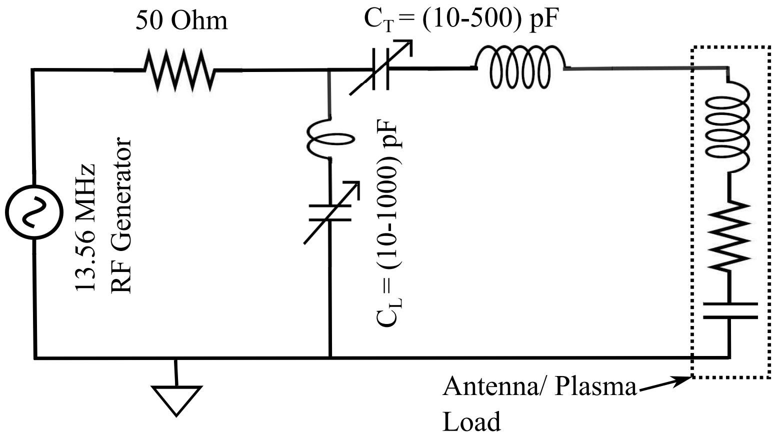

Figure 3.4: Equivalent circuit for L-Matching network, C_L and C_T respectively are the vacuum variable load and tuned capacitors.

3.2.4 RF shielding and grounding

Shielding prevents coupling of undesired radiated electromagnetic energy into the equipments. Coupling RF power with the plasma in a more efficient way through the antenna is the primary desire for most of the RF applications. It is essential to shield the antenna, transmission line along with all inter locking from the source, to inhibit undesired radiated electromagnetic energy into the other equipments. Therefore, it is important to know about the thickness of shielding enclosures and its dependency on radiated RF frequency and the choice of appropriate materials, to get the better shielding effectiveness and optimize the RF shielding design for its application on plasma production. The manner in which an electromagnetic (EM) shield transmits plane EM wave has been shown to be analogous to the manner in which a conventional two wire transmission line transmits electrical current and voltage. For plane wave shielding, EM radiation/ power can be lost via the following ways. (i) Due to penetration or absorption inside the shielding enclosure material is called penetration loss (A). (ii) If the characteristics line impedance mismatch with the input, reflection occurs at the boundary or on the surface of the shielding enclosure called reflection loss (R). (iii) The reflection loss depends on the basis of reflected wave either travels back several times by successive re-reflections, which is then more general for consideration, called internal reflection (B). Hence the total shielding effectiveness or insertion loss is defined as $(S) = A + R + B$. Penetration loss $A(dB) = 8.686\alpha l$, where $\alpha = sqrt(\pi\mu f\sigma)$, l is the thickness of the shielding enclosure, σ is the shielding material conductivity, f is the radiation frequency and μ is the permeability. Shielding enclosure will be chosen sufficiently thick enough to provide penetration loss $\sim$ 100dB so that the other reflection loss can be neglected [73]. Shielding enclosure thickness for Silver, Cu, Al and Brass with various frequencies around our 13.56MHz source are shown in figure (3.5a). For this calculation conductivity of Cu is taken $\sigma_{Cu} = 5.8 \times 10^7 S/m$. Conductivities of other materials are taken as $\sigma_{Silver} = 1.1 \times \sigma_{Cu}$, $\sigma_{Al} = 0.61 \times \sigma_{Cu}$ and $\sigma_{Brass} = 0.28 \times \sigma_{Cu}$.

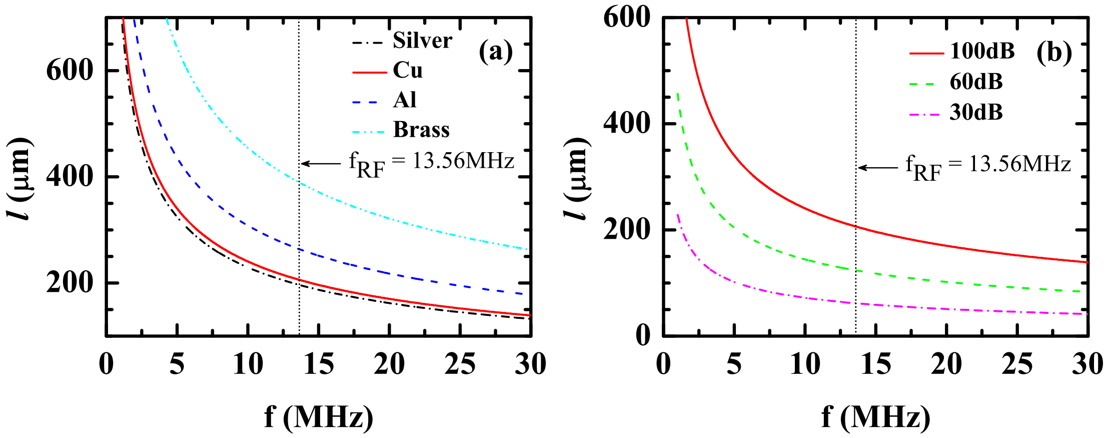

Figure 3.5: Shielding thickness (a) for Silver, Cu, Al and Brass for 100dB penetration loss, (b) Shielding effectiveness of Cu with RF frequency.

The result indicates that for 100dB penetration thickness of Silver ($195\mu m$) is little lower than Cu ($205\mu m$) for our source frequency 13.56MHz. However, the cost of Silver is more than Cu. Thickness of Al and Brass is much more than Cu. Thinner material is good for making desire shape for shielding enclosure. Figure (3.5b) shows that the shielding thickness for Cu is decreases with decreasing the penetration loss for 100dB to 30dB for 13.56MHz. At lower penetration loss other reflection loss will be pronounced. Therefore, $200\mu m$ Cu sheet has been used for making cylindrical shape enclosure for RF shielding as shown in figure (3.6b).

Initially low cost brass mesh has been used for shielding purpose. However use of Cu sheet (thickness 200μm) for our 13.56MHz RF source improved the RF shielding significantly compared to brass mesh. The radiation strength 30 cm away from the Cu enclosure is measured $\sim (2-4)$V /cm using power meter. The photograph shown in figure (3.6a), indicate the source plasma inside the brass enclosure and figure (3.6b) shows the installation of Cu enclosure for RF shielding. Experimental results presented in this thesis carried out with this Cu shielding enclosure.

A 5KVA isolation transformer is used to power the single phase (50 Hz) RF generator. The common reference in the secondary of the transformer is connected to the Cu shielding enclosure and RF generator common, which is separately grounded. The conducting SS chamber is acting as measurement reference for all diagnostics, which is also separately grounded.

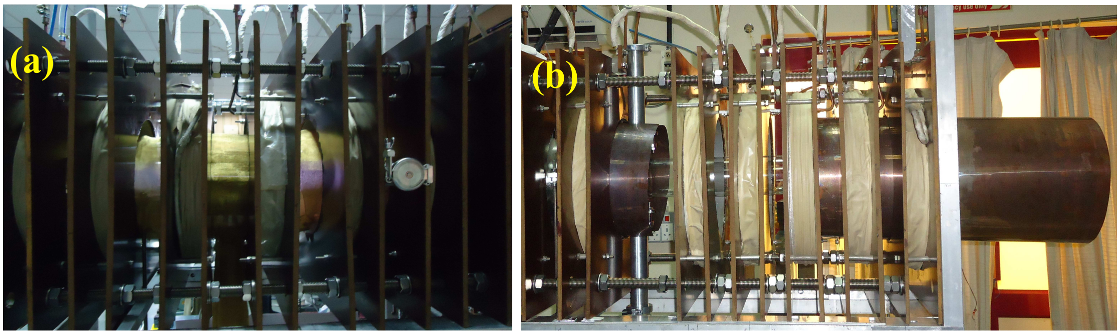

Figure 3.6: (a) Initially Brass mess was used for RF shielding, plasma is visible through this mesh. (b) Shielding effectiveness is improved significantly replacing the Brass mess with Cu jacket.

3.2.5 Magnets

Eight axis-symmetric electromagnetic coils (figure 3.1) are used to produce uniform axial magnetic field from -30 cm to $+50$ cm with respect to the antenna center. One to seven electromagnets are made identical in shape and number of turns. Cu tube has been used for making the magnet winding. Inner and outer diameter of the Cu tube are respectively 6mm and 8mm. Each of these magnets are composed of total 36 turns, distributed in 6 layers. Where each layer contains 6 number of

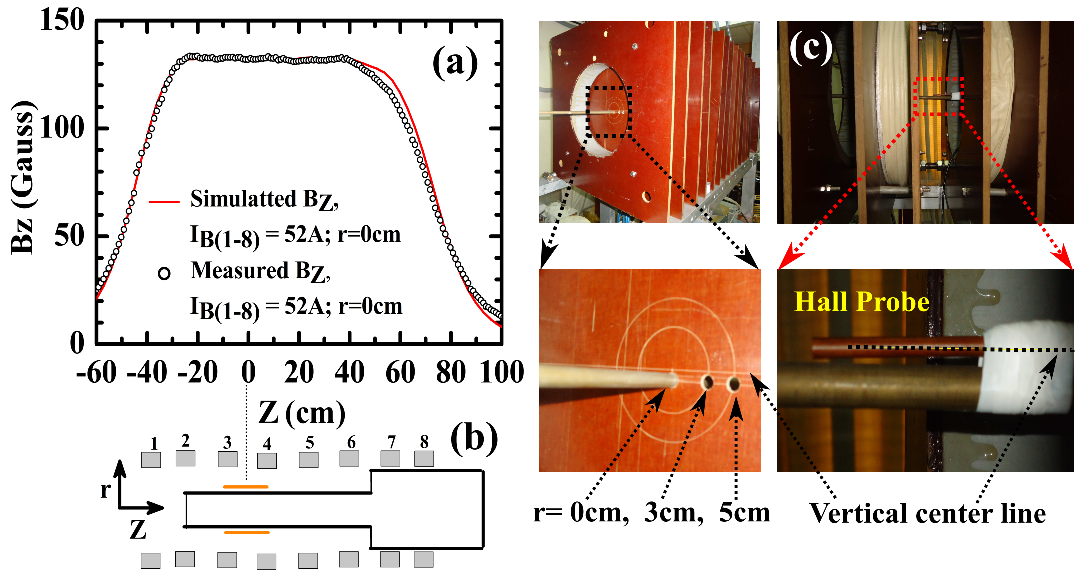

Figure 3.7: (a) Measured (circular data points) axial magnetic field and the COMSOL simulated results (red line) at $r = 0$ cm. (b) The schematic shows the location of antenna and location of electromagnets with indication of (r, Z) co-ordinate. (c) The arrangement for measuring B_z at $r = 0, 3$ and 5 cm using hall probe is shown in the photographs. 52A current is flowing through each of the eight electromagnets.

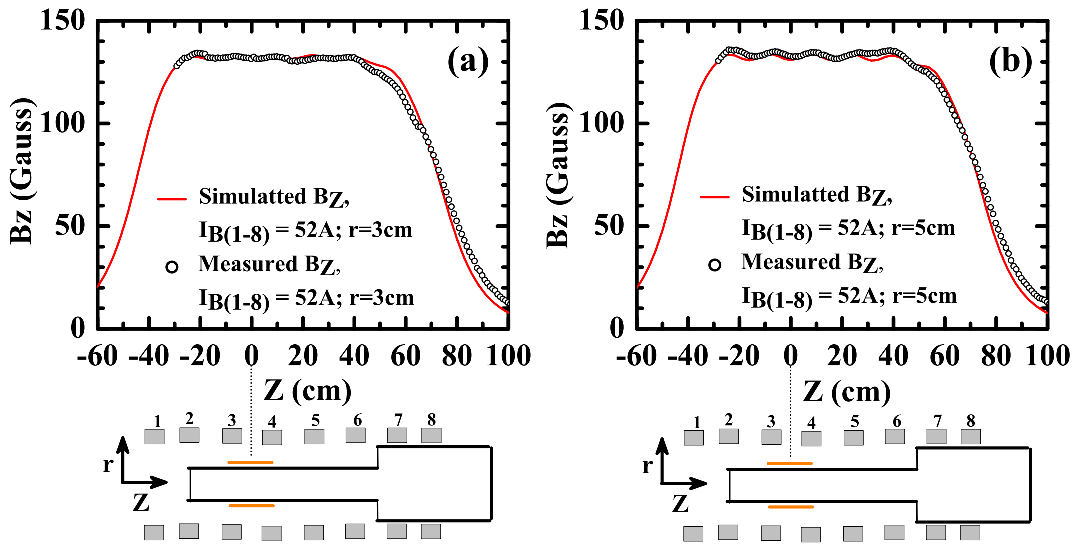

Figure 3.8: Measured (circular data points) and simulated (red line) axial magnetic field at (a) $r = 3$ cm and (b) $r = 5$ cm.

turns. Inner, outer diameter and width of each magnets are respectively 31.5 cm, 43.5 cm and 6 cm. Total 30 number of turns distributed in 5 such layers in 8^{th} magnet. Chilled water passed through the Cu tube to cool the each magnets. All magnets are positioned at simulated locations along both the source and diffusion chambers with respect to the antenna center to produce the axial magnetic field.

The COMSOL simulated magnetic field and the measured axial magnetic field using hall probe (Model no. 5180, F.W. Bell make) at r = 0 cm is shown in figure (3.7). The measurement scheme and the hall probe mounted arrangements are shown in the photographs (3.7). Magnetic field mapping is also carried out at r = 3 and 5 cm. The simulated result matches well with the hall probe measurements both at on (figure 3.7) and off-axis (figure 3.8). These electromagnets can be powered in numerous arrangements to produce different axial magnetic field configurations such as axially uniform, axially non-uniform, cusp etc. These magnetic field configurations make the system more flexible in term of controlling the source and diffusion plasma. Experiments presented in this thesis are conducted using argon gas over the pressure range $(1 \times 10^{-4} - 5 \times 10^{-3})$ mbar with variable RF power from 100 to 800 Watts.

3.3 Implemented diagnostics

The diagnostics used for the experiments presented in this thesis are the high frequency magnetic probe for wave field measurements, retarding field energy analyzer (RFEA) for ion beam energy and ion energy distribution function measurements (IEDF), RF compensated single Langmuir probe [74], double probe, triple probe [75] for local density, temperature and floating potential measurements, emissive probe [76] for plasma potential measurement, RF current probe for antenna/ plasma impedance measurement. Details of each of these diagnostics with technical know how are described in the following subsections.

3.3.1 High frequency magnetic probes

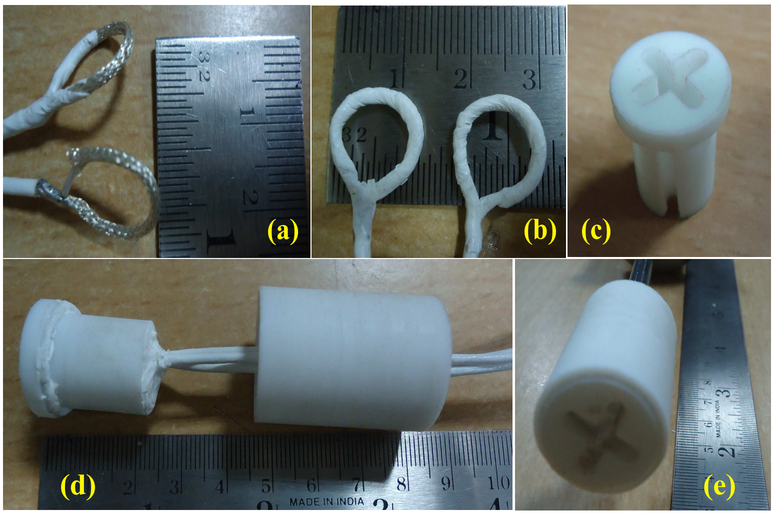

Figure 3.9: High frequency magnetic probe, (a) Single loops using coaxial cable, (b) Single loops with Teflon insulation, (c) Ceramic housing for keeping them mutually perpendicular to each other, (d) Three mutually perpendicular loops are mounted and (e) covered.

To measure the axial variation of all three components (b_z, b_θ, and b_r) of helicon wave fields, a single loop high frequency magnetic probe [51, 52] has been used. The magnetic probe is made from 1.8mm outer diameter (F196, Flu-Tef Industries) coaxial cable, with the center conductor connected to the outer conductor at the end of the coax to form a loop of about 4mm radius. The coax is covered with Teflon tape and mounted inside ceramic housing. For the axial scan of wave-field measurements, the probe housing is mounted on a SS shaft (1/4 in) bent into a dog leg to swing the probe into the plasma. The shaft is fed through a vacuum fitting in the end-plate of the conducting expansion chamber and rested $\sim$ 1cm above from the bottom of the glass source tube. In a time varying uniform magnetic field $B(t)$, the voltage induced in the magnetic probe is $V(t) = A\frac{dB}{dt}$, where A is the area of the single loop. Signal strength is linearly proportional to the area of the probe. To measure the axial variation of Z-component helicon wave field, a pair of high frequency magnetic probe [52] has been used. The axial probe has been inserted through the end flange of the expansion chamber, which can be moved along the Z-axis at $r = 3.5$ cm. The radial probe is inserted through a radial port of the source chamber and it can be moved along radius at $Z = 30$ cm. For measuring the axial variation, the radial probe acts as reference probe positioned very close to the chamber wall ($r = 4.5$ cm), whereas for measuring the radial variation, the axial probe acts as a reference.

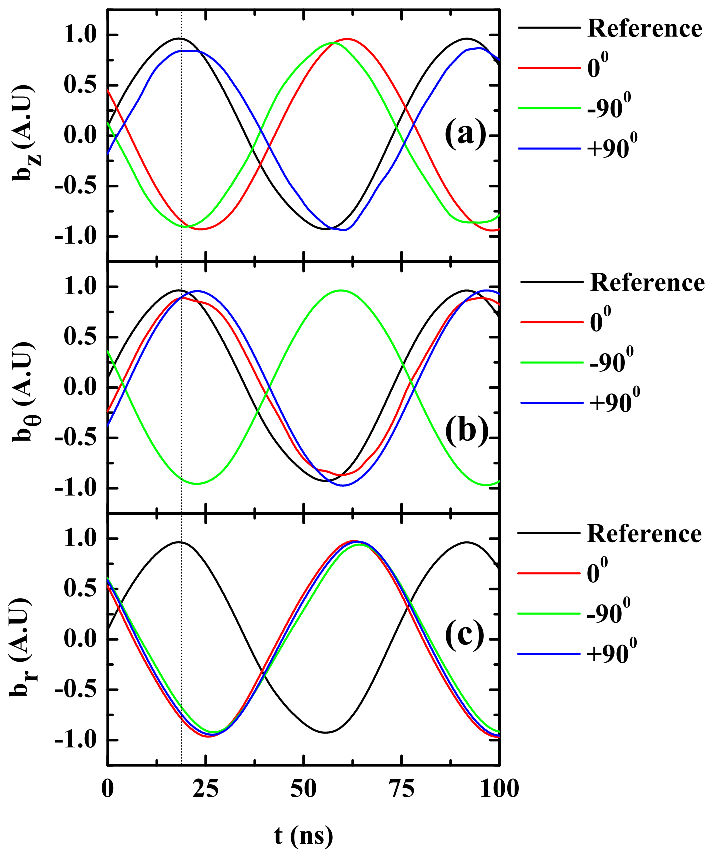

Figure 3.10: Three mutually perpendicular probes inserted from the radial port of the source chamber at $r = 30$cm. The probe housing with shaft as a whole is rotated clockwise ($+90^0$) and anticlockwise (-90^0). (a) One loop has been identified measuring with z-component of wave magnetic field (b_z), (b) Another one loop has been identified measuring with θ-component of wave magnetic field (b_θ) and the remaining third loop has been identified measuring with r-component of wave magnetic field (b_r). Direct RF antenna current oscillation has been taken as reference for all components of wave field measurement.

Three mutually perpendicular such single loops are mechanically placed concentrically inside a macor ceramic housing for simultaneous measurements of all the three components (b_z, b_θ, and b_r) of wave fields. The photograph (3.9) shows the loops, and the housing arrangements for this probe assembly. This probe assembly is inserted into the system through one radial port (at Z=30 cm). To identify which loop among the mutually perpendicular three, measures which component of wave field, the entire probe shaft is rotated in presence of plasma. The positive axial direction of our system is defined from source to expansion chamber (figure 3.1). The -90^0 angular rotation of probe shaft is defined the rotation of shaft from $+Z$ to $-Z$ anticlockwise. Similarly $+90^0$ angular rotation of probe shaft stands for clockwise rotation. Since the three loops are mutually perpendicular to each other so by right angle rotation signal of two probes must be interchange (here b_z and b_θ) (figure 3.10a, b). The remaining third loop axis is same as the axis of shaft rotation, hence no change in signal is expected (here b_r) (figure 3.10c) for this probe while rotation. RF antenna current signal is taken using a current probe (discussed at the end of this section) simultaneously with the three high frequency magnetic probe signal using a 4-channel oscilloscope (TDS-3034C, Tektronix make). This RF antenna current signal is taken as a reference (figure 3.10a, b, c) for wave phase measurement purpose.

3.3.2 Retarding Field Energy Analyzer (RFEA)

A retarding field energy analyzer (RFEA) has been designed and developed to measure ion energy distribution function (IEDF) in helicon plasma. To design RFEA, determination of shape, size of the analyzer orifice, choice of grid and their separations are discussed. The four grid energy analyzer assembly provides easy access of all internal mechanical components and electrical connections. Fundamental problems regarding acquisition of correct RFEA data and their probable solutions are discussed. Conventional Langmuir probe measures electron energy distribution function (EEDF) in plasmas. RFEA is useful diagnostic for both ion energy distribution function (IEDF) and EEDF measurements. RFEA is widely used in expanding plasma systems, particularly where ion beam is generated [77]. RFEA has been used in capacitive and inductive RF plasma to measure IEDF and local plasma potential [78]. Description of RFEA design of parallel plane four grids retarding field energy analyzer, which has been developed primarily to measure ion beam energy and plasma potential in helicon antenna produce radio frequency (RF) plasma. It is also shown that the design is flexible and provides easy mechanical and electrical access. Entering energetic electrons into the RFEA cavity, bias voltage scheme, offset adjustment, capacitive pick up problems are addressed.

3.3.2.1 RFEA design and construction

Charge particles are transmitted through an aperture, are analyzed by the retardation of electric field established through bias potentials applied to the number of grids. The entrance slit must be wide enough to permit adequate flux transmission, yet sufficiently small such that the electrostatic sheath established around the slit edges be large enough to bridge the aperture width and hence shield the aperture from the bulk plasma. After the first entrance grid, second grid repels electrons (in ion mode operation) called repeller. Third grid samples different energetic ions, called discriminator. Forth grid suppresses the secondary electrons coming due to ion bombardment on the collector surface is the suppressor followed by the collector plate. A fraction of incident ion flux is transmitted through the slit. The slit entrance plate can be kept floating or biased negative to repel thermal electrons. The schematic of RFEA bias scheme is shown in figure (3.11).

The ions of charge e, are assumed to enter from the main plasma with kinetic energy $E = eV_0$. They are retarded by the axially directed electrostatic field between the grid electrodes and collected at the collector. If $V_0 > V_d$ they will reach the plate and appear as collector current I_c; and if $V_0 < V_d$ they will be resisted. For discriminator voltage $V_d = 0$ to V_S, I_c remain constant, means all ions gain a parallel energy of (eZ_iV_S), where (eZ_i) is the ion charge and V_S is the sheath voltage, which is the plasma potential (ϕ_P) with respect to the grounded

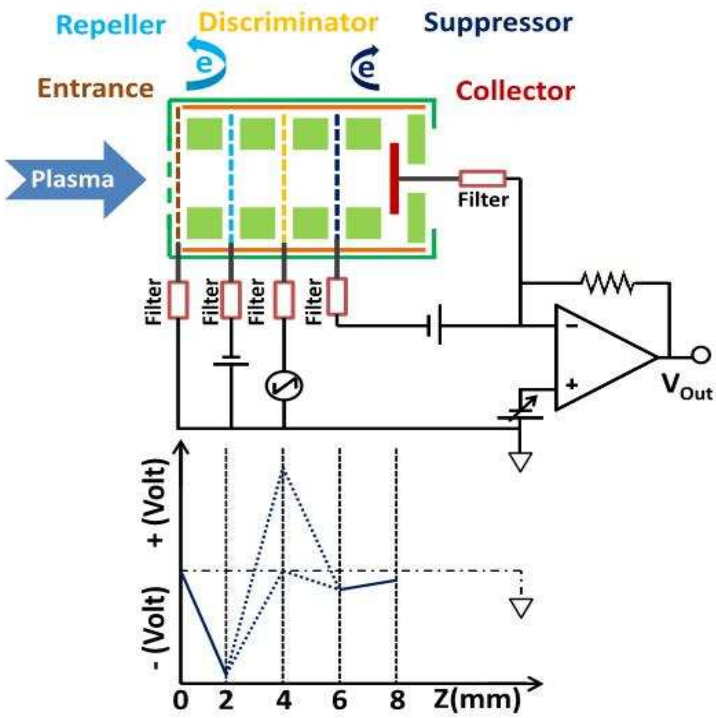

Figure 3.11: RFEA four grids electrical bias scheme.

chamber for a collision-less sheath. For $V_d > V_S$, I_c starts to decrease. I_c is expressed in equation (3.1)

$$I_C = eZ_iA_{eff}T_ET_1^4\int_{v_{min}}^{+\propto} f(v)dv \tag{3.1}$$

$$\frac{dI_C}{dV_d} = -\frac{e^2A_{eff}T_ET_1^4}{M_i}f(\sqrt{\frac{2eV_d}{M_i}}) \propto f(v) \tag{3.2}$$

Where, A_{eff} is the effective area of entrance apertures, T_E is the transparency of the entrance slit plate, T_1^4 is the transparency of the total four mesh grid, $v_{min} = \sqrt{\frac{2eV_d}{M_i}}$, v is the parallel ion velocity and $f(v)$ is the parallel ion velocity distribution. Ion energy distribution function (IEDF), as indicated in equation (3.2), is proportional to the derivative of collector current and discriminator voltage. That will be derived from the RFEA $(I_c - V_d)$ characteristics.

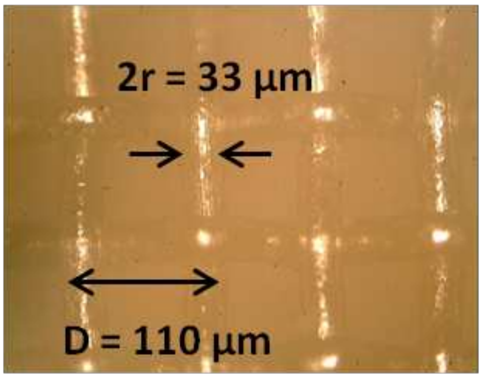

Figure 3.12: RFEA grid with microscope measurement of inter-wire spacing with wire dimension.

Mechanical drawing (3.13) and each component of RFEA assembly with internal electrical connection, insulation and RF shielding are shown in figure (3.14). Distance between entrance grid to collector of RFEA is chosen to be less than ion neutral collision mean free path (λ_{i-n}) which is $8mm$ at 3.75×10^{-3}mbar. The inner diameter (circular plasma facing front side) of the RFEA is optimized to be $5mm$, which accommodate array of holes, of diameter $d = 0.9mm$ each to make it close to satisfy the condition of electron entering into RFEA ($d \sim 2\lambda_D$) [79]. RFEA energy resolution $\frac{\nabla E}{E} = \frac{D^2}{16S^2}$ depends on the inter grid separation (S) and grid wire separation (D) [80]. Large ($\sim mm$) grid wire separation increases energy resolution. However, this leads to very poor transmission $(T) = \frac{D-2r}{D^2}$, if the grid wire radius (r) is not very thin ($1 - 10\mu m$). Grids having $D = 110\mu m$ and $2r = 33\mu m$ (figure 3.12) with grid transparency 0.49 are used in our RFEA.

3.3.2.2 DC characterization

Experiments are performed in HeX system, where plasma is produced by application of $200W$ RF power at 2×10^{-4}mbar Argon fill pressure. Initial troubleshooting experiments are carried out by applying bias to all the grids with respect to the entrance grid, which is electrically connected with the Aluminum enclosure. While doing that it is also applied suppressor grid bias (V_{Sup}) with respect to this common reference instead of suppressor grid bias with respect to collector as shown in figure

(3.11). Keeping that bias configuration, the role of repeller bias (V_R) or retarding potential on the RFEA characteristics is studied. Figure (3.15a) shows that for $V_R = -60V$, I_c increases with discriminator bias V_d from 0 to $15V$. Whereas, for $V_R = -120V$ (figure 3.15b), I_c remains constant up to the plasma potential. In both the cases, the suppressor grid is kept at same potential. In figure (3.15c), $V_R = -120V$ and $V_{Sup} = -25V$, no significant change is observed in the characteristics figure (3.15c) compared to figure (3.15b). These results indicate that there is no significant role of V_{Sup} for this biasing scheme. However, higher repeller bias significantly improves the characteristics by objecting high energy electrons entering into the RFEA. High energy electrons are restricted by the $-120V$ repeller bias (figure 3.15b) but not for $-60V$ bias (figure 3.15a). The data presented in figure (3.15a, b and c), shows a dc off-set in all cases. To adjust this off-set the bias voltage is applied into suppressor grid with respect to the collector as shown in figure (3.11). In that configuration, even a very small suppressor bias ($V_{Sup} = -1.5V$) with respect to the collector is sufficient to make the necessary off-set adjustment (figure 3.15d). Due to ion bombardment on the collector surface, secondary electron emission is enhanced. Hence the effective total current which is the sum of both collected ion and emitted electrons. At higher positive retarding voltage ($\sim 100V$) maximum ion may be reflected by this discriminator but the secondary emitted electron current will hold non-zero collector current, which causes this off-sets. However, introducing a suppressor grid between discriminator and collector and application of negative potential into this grid with respect to the collector will force those secondary emitted electrons to return back to the collector or in other word this bias arrangement will oppose emission of those secondary emitted electrons from the collector surface. Therefore, this biasing scheme is suitable for collector signal off-set adjustment. Presence of energetic ion creates this off-set with small suppressor bias. In this case suppressor bias has to rise more to adjust this off-set. Another point is that, due to negative suppressor bias some ion will also be collected by this suppressor grid. In this bias configuration (figure 3.11) collected ion current is the sum of ion current collected by the collector as well as suppressor grid. Hence the signal strength improves in this scheme. In figure (3.15a, b, c and d), measurement of collector current for both increase and decrease bias voltage are found to be almost identical nature ($I_c - V_d$) characteristics. This confirms that there is no such space charge accumulation between any grids.

3.3.2.3 AC characterization

After preliminary dc characterization and testing different bias schemes, a unipolar transistor amplifier ramp generated bias ($0-120V$) is applied to the discriminator grid to sample different energetic ions entering into the analyzer. The transistor amplifier [81] circuit is shown in figure (3.16). Low frequency ($\sim 50mHz$) ramp bias application to the discriminator essentially helps to get collector current (I_c) versus discriminator bias (V_d) keeping $V_R = -100V$ and $V_{Sup} = -5V$. A current (I) to Voltage (V) converter [82] circuit is used to measure low ($\sim nA$) ion current collected by the collector. The detail circuit for data acquisition is shown in figure (3.17). RFEA composed of parallel grids and collector having different potentials on them. The configuration is analogous to parallel plate capacitor. The time varying potential on the discriminator is very sensitive to generate unwanted capacitive pick up. When such picks up are unavoidable, generally it is tried to minimize this pick up as much as possible to get better ($\sim 10^3$) signal to pick up ratio. One way to minimize the capacitive pick is to reduce the discriminator ramp frequency ($\sim mHz$).

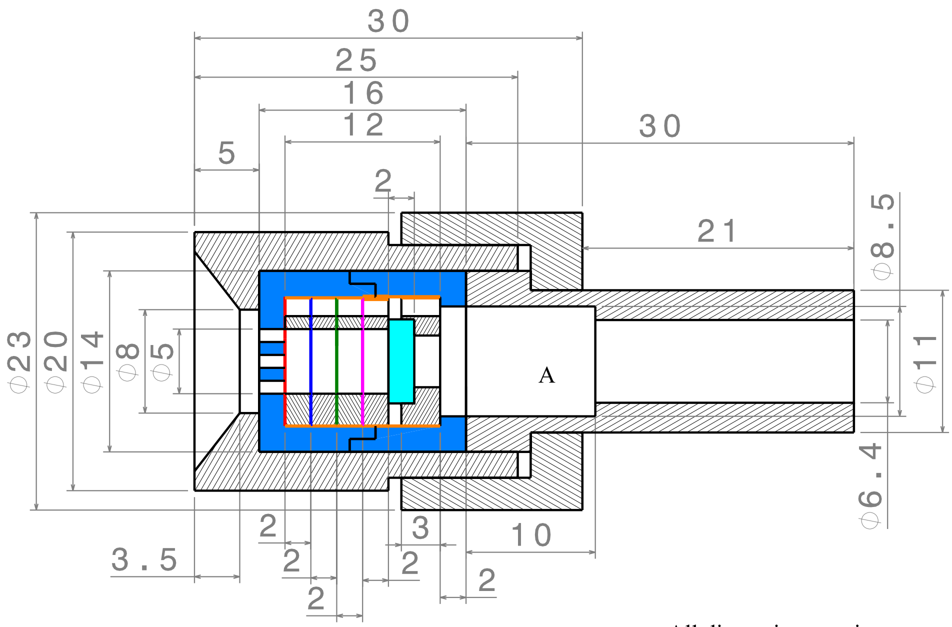

Figure 3.13: Schematic of retarding field energy analyzer (RFEA), Blue color part is the Al enclosure for RF shielding. Red, Blue, Green and Magenta color vertical lines are the four mesh grids. Cyan color part parallel to grids is the collector. The empty space with English letter ‘A’ mark accommodate RF chokes/filters.

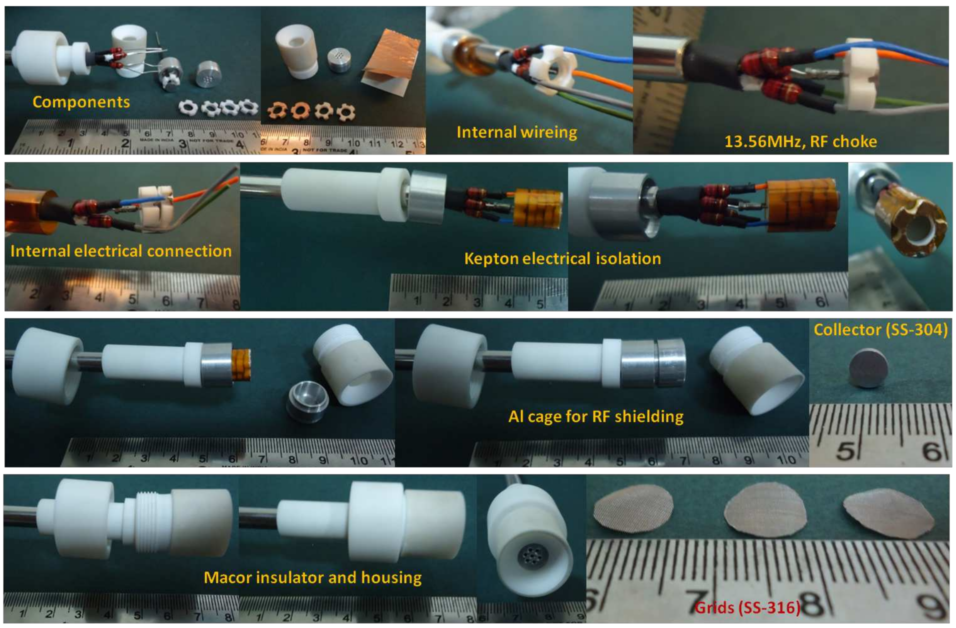

Figure 3.14: Photographs of each step of RFEA assembly.

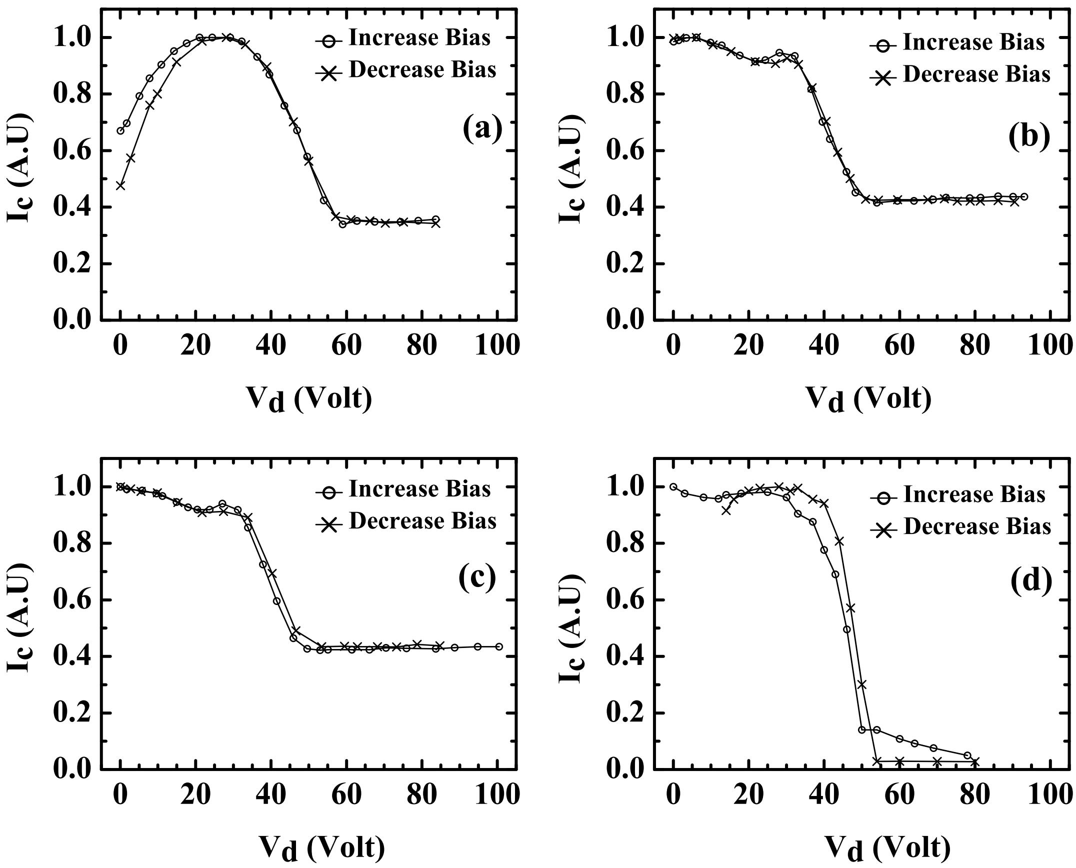

Figure 3.15: Collector current (I_c) versus discriminator bias (V_d) voltage with (a) Repeller bias (V_R) = −60V, Suppressor bias (V_{Sup}) = 0V, (b) $V_R = -120$V, and $V_{Sup} = 0$V, (c) $V_R = -120$V, $V_{Sup} = -25$V with respect to entrance grid and (d) $V_R = -120$V and $V_{Sup} = -1.5$V with respect to the collector.

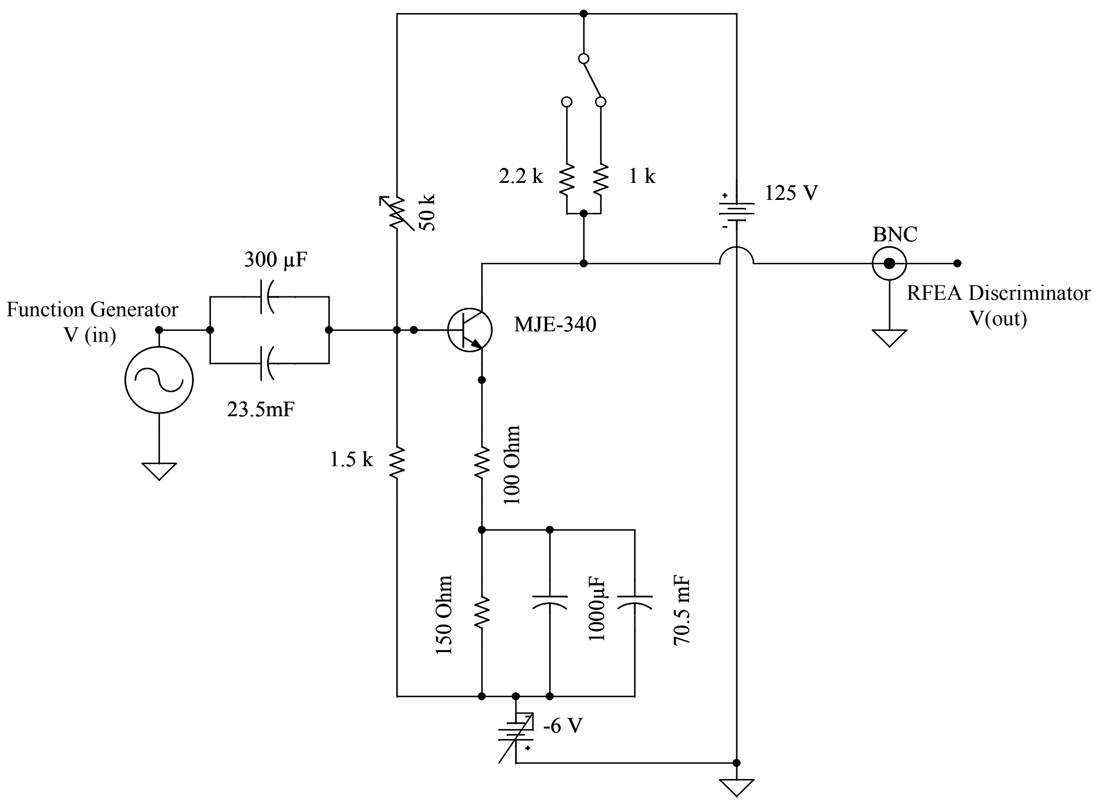

Figure 3.16: Common Emitter (CE) mode transistor amplifier circuit for unipolar ramp bias application in the discriminator of RFEA.

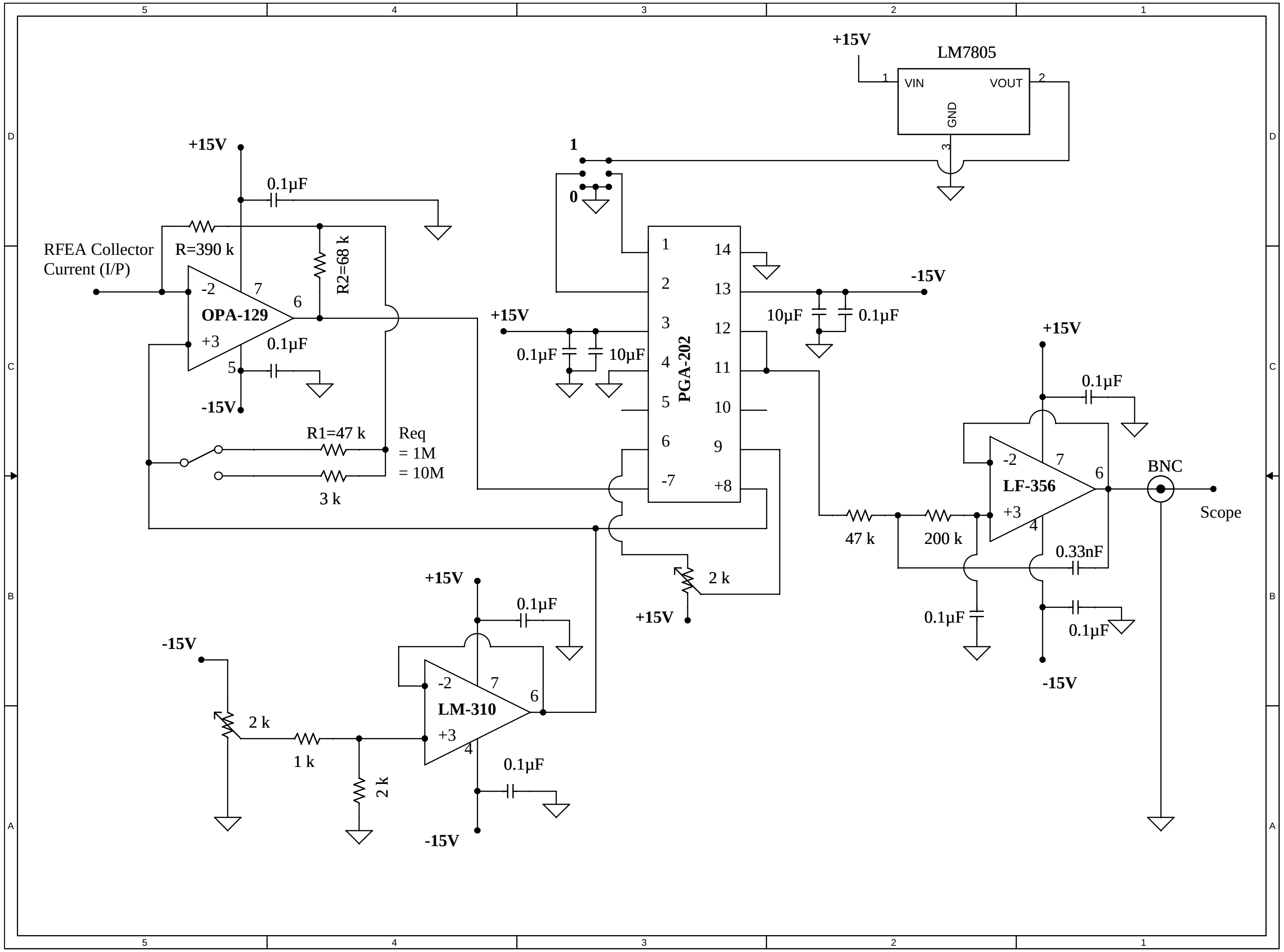

Figure 3.17: I to V converter circuit for RFEA signal measurements.

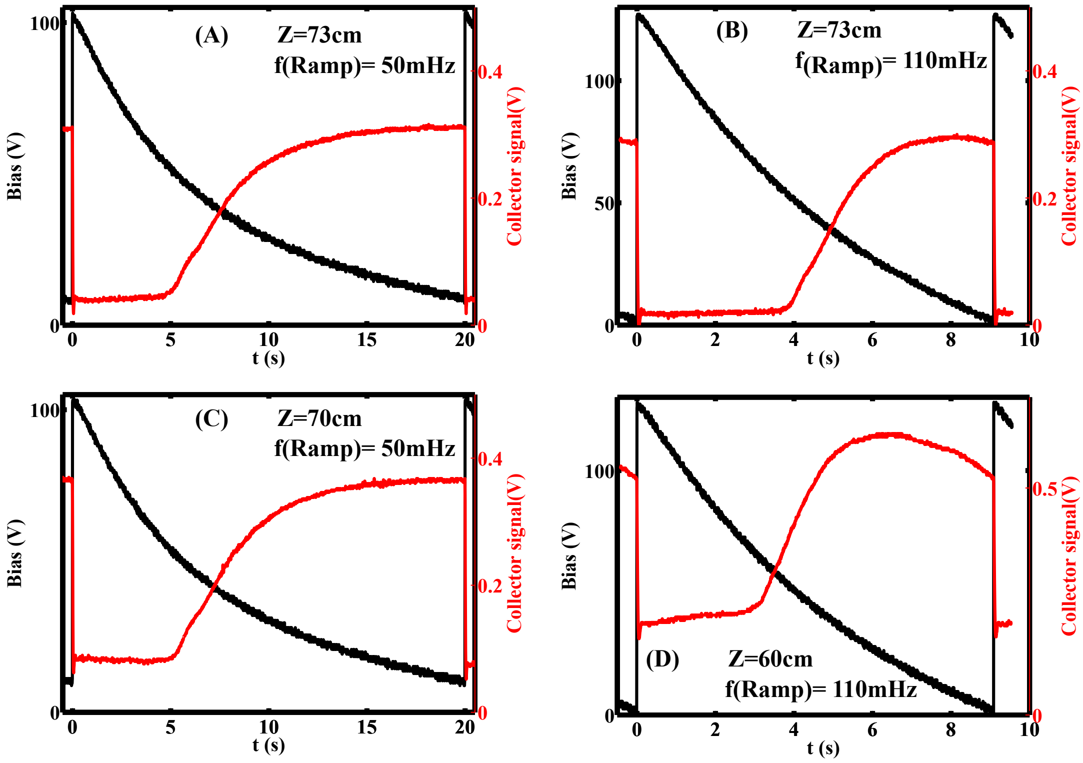

Figure 3.18: RAW RFEA characteristic with discriminator bias V_d = 130V (A) at Z = 73 cm with ramp frequency = 50 mHz, (B) at Z = 73 cm with ramp frequency = 110 mHz, (C) at Z = 70 cm with ramp frequency = 50 mHz, (D) at Z = 60cm with ramp frequency = 110 mHz.

Experiments have been carried out in presence of double layer like potential structure. RFEA is placed 73 cm away from the antenna center ($\sim$ 30 cm away from the double layer like potential structure) and the 20 second long ramp measures the RFEA characteristics. The characteristics (red curve) in figure (3.18) shows there is a small change in collector current decreasing slope (at $\sim$ 6 sec), indicate the presence of double layer generated ion beam, which will be discussed in detail in chapter 4. The collector signal reaches almost close to zero collector signal ($\sim 20mV$), at higher discriminator bias ($> 70V$) when RFEA is located at ($Z = 73cm$), known as dc offset. This dc offset in collector signal is increased from $20mV$ to $50mV$ and then $200mV$ while moving the RFEA from $Z = 73cm$ to $70cm$ and then $60cm$ respectively as shown in figure (3.18a, c and d). This is due to the fact that the energetic electron which overcome the double layer like potential hill (untapped electrons), enters into the RFEA and increases the dc offset. The data shown in figure (3.18d) is very much similar to as observed in figure (3.15a), resembling the fact of energetic electron entrance into the RFEA. Experimental results show, closure the RFEA towards the potential hill, higher the dc offset. The knee (indicating the presence of energetic ions figure 3.18a) changes with peak of ramp bias voltage as well as frequency indicating the same ion energy(figure 3.18b). This confirms the validity of our measurement and existence of double layer like potential structure. At 50 mHz discriminator ramp bias capacitive pickup reduces significantly and signal to capacitive pickup ratio is $\sim 10^3$. Therefore, the collector current signal is well resolved. The transient capacitive pickup in absence of plasma is shown in figure (3.19). In presence of plasma collector current to discriminator bias voltage RFEA characteristics are shown in figure (3.18).

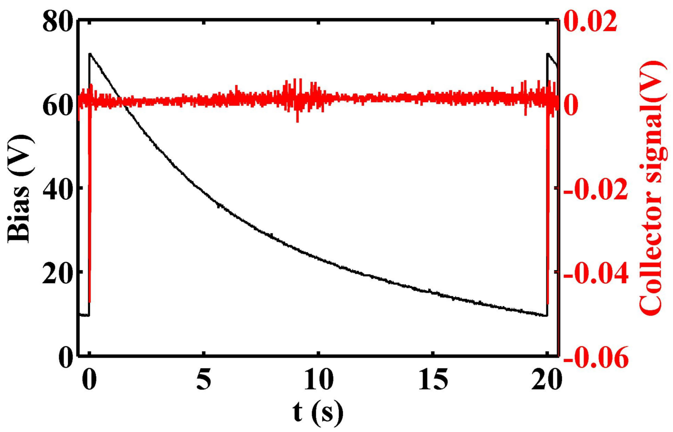

Figure 3.19: RFEA data in absence of plasma

RFEA diagnostic has been designed and developed for measuring IEDF in helicon antenna produce plasma. The designed gives flexibility to access all the electrical components, grids and electrical connections. Initial dc characterization is carried out to understand suitable repeller bias voltage and bias scheme for ion collection mode operation. A low frequency ($\sim 50mHz$) transistor amplifier circuit is used for application of bias to the discriminator and collector signal is acquired using an analog (I to V) converter circuit, which detects the ion beam generated from the double layer like potential structure.

3.3.3 RF compensated single Langmuir probe

Interpretations of single Langmuir probe measurements in electrode-less radio frequency (RF) plasmas are noteworthy tricky and require adequate compensation of RF. RF compensation of Single Langmuir probe at low density RF plasmas ($\sim 10^{16} m^{-3}$) is presented in this section. In RF driven plasmas, where the RF voltage is high ($\sim 50V$) and density is in the range ($\sim 10^{16} m^{-3}$), the primary RF compensation condition ($Z_{ck} >> Z_{sh}$) is very difficult to fulfill, because of high sheath impedance (Z_{sh}) at 13.56MHz and the construction limitation of a self-resonant tiny choke (Z_{ck}) with very high impedance. Introducing a large auxiliary electrode (A_x), ($A_x >>> A_p$), close to the small Langmuir probe (A_p) tip, connected in parallel with probe via a coupling capacitor (C_{cp}) (figure 3.20 and 3.21), significantly reduces the effective sheath impedance (Z_{sh}) and allows probe bias to follow the RF oscillation. Dimensional requirements of the auxiliary electrode and the role of suitable coupling capacitor are discussed in this section. Observations show proper compensation leads to estimation of more positive floating potentials and lower electron temperatures compared to uncompensated probe. The electron energy probability function (EEPF) is also obtained by double differentiating the collected current with respect to the applied bias voltage using an active analog circuit.

Apart from basic plasma studies, the electrode-less RF plasma sources are widely used in semiconductor industries and material processing, coating, etching etc. And single Langmuir probe remains the most commonly used diagnostics for plasma density and temperature measurements. However, their uses in radio frequency plasmas are not very straightforward. There are primarily two issues which make the use of this diagnostics complicated; 1) there is no reference electrode and 2) the plasma potential (V_S) oscillate with the RF source with respect to the instantaneous probe bias voltage [83]. Placing a reference electrode having area larger than probe dimension or conducting plasma enclosure may resolve the first issue. But the later one requires much more attention as it is very crucial for proper Langmuir probe data interpretation.

Significant progresses have been made since last 50 years on implementation of various techniques for removing RF modulations from the Langmuir probe characteristics in RF plasmas. In 1992, Godyak et al. [84] removed the 13.56 MHz RF modulation and its first harmonic at 27MHz by placing a self-resonating choke [85] very close to the probe tip. In that paper they have also reported electron energy probability function (EEPF), presence of hot electrons and their Bi-Maxwellian distribution in RF discharges. However, these kinds of self resonance chokes suffers limitation from high impedance side and are difficult to construct in tiny sizes to be placed very close to the probe tip. As a result this RF compensation technique is successful in high density ($\sim 10^{17} m^{-3}$) plasmas. In 1994, Sudit et al. [74] used the similar technique with placing an additional electrode, having larger area than the probe tip. Presence of additional electrode with a coupling capacitor close to the probe together with the self-resonating chokes satisfied the necessary impedance requirement criteria for RF compensation. However, the quantitative description regarding the dimension of additional electrode with which one can achieve RF compensation at lower densities ($\sim 10^{16} m^{-3}$) is unavailable. In this section, quantitative description of dimensional requirements of additional electrode and successful RF compensation at low density ($\sim 10^{16} m^{-3}$) RF plasmas are presented.

Radio frequency plasma is produced by applying 13.56MHz RF power into a right helicon antenna concentrically placed on outer surface of a cylindrical glass chamber. External magnetic field has been used for confining both electrons and ions in the source chamber. Langmuir probes are used to measure the local density and temperature and EEPF of the plasma. The cylindrical Langmuir probe is made of tungsten wire and is 4 mm long and 0.5 mm in radius. Langmuir probe

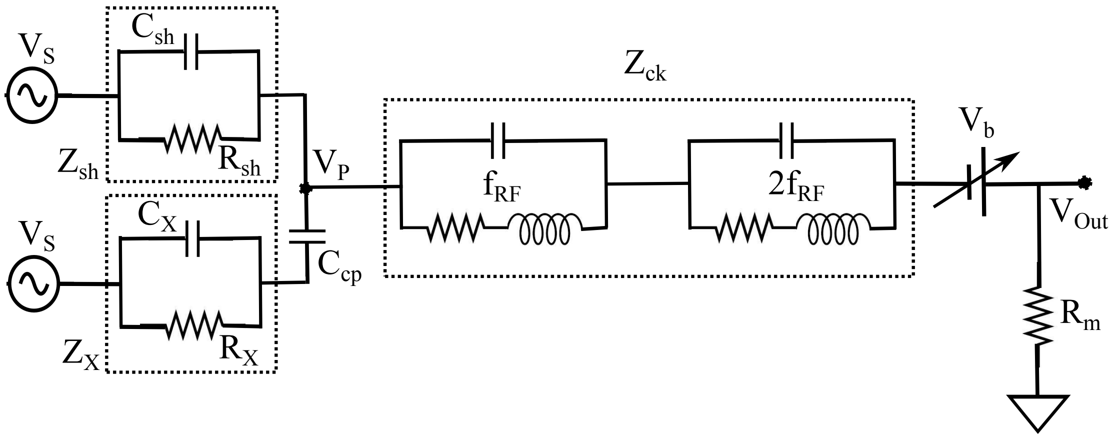

Figure 3.20: Equivalent RF Compensation circuit

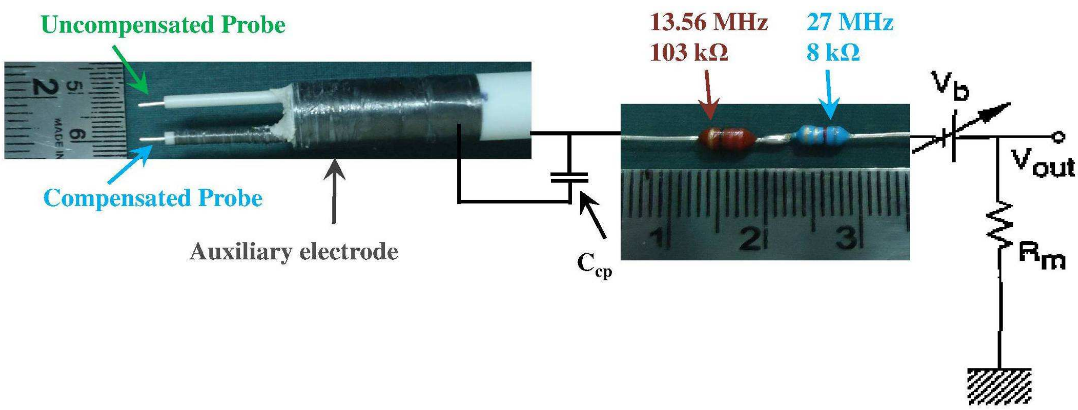

Figure 3.21: Physical dimension of single Langmuir probe, auxiliary electrode, and self resonance chokes with circuit architecture for RF compensation.

traces are obtained applying $\pm110V$ ramp (frequency 11Hz) bias to the probe with respect to the grounded conducting expansion chamber. Data analysis of raw $(I - V)$ trace and logarithmic electron current with respect to bias voltage, determines electron temperature (T_e) and ion density (n_i). Ion density is calculated from the ion saturation current from the Langmuir probe using the formula $I_i^{sat} = 0.6en_iA_p\sqrt{\frac{T_e}{M_{Ar}}}$ [86]. Where I_i^{sat} is the ion saturation current, e is electron charge, n_i is the bulk ion density, A_p is the probe collection area for ions, M_{Ar} is the mass of Argon ion. Electron temperature is measured by fitting a straight line to the exponential region of logarithmic electron current. [86–88].

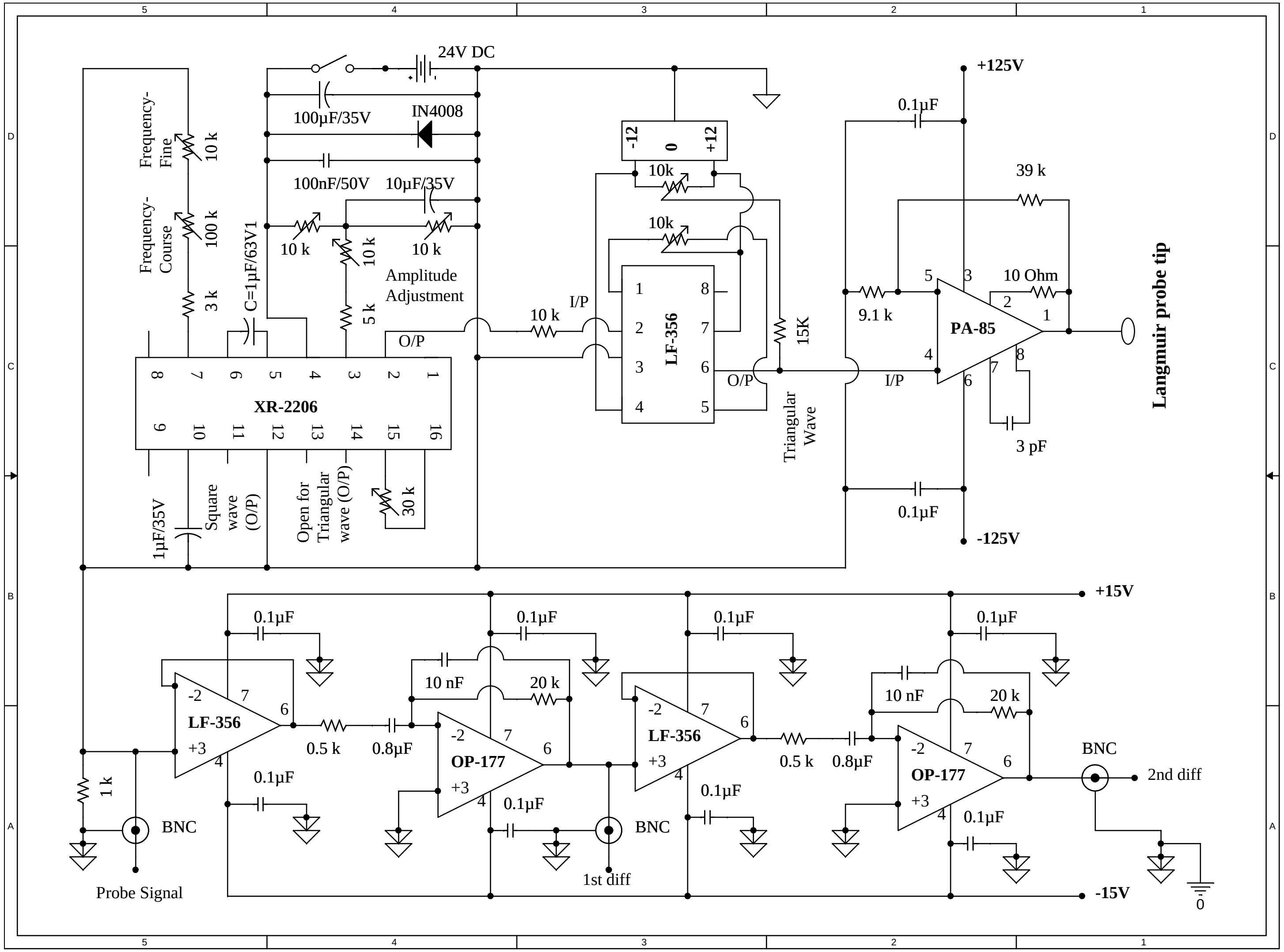

Figure 3.22: RF compensated single Langmuir probe circuit for electron energy probability function (EEPF) measurement.

3.3.3.1 RF compensation

To avoid large voltage swings in probe potential, V_P, it is customary to add resonant chokes near the probe tip which offers large impedance to the RF oscillations and low impedance for low frequencies. Two tiny self-resonating chokes are used for compensating 13.56 MHz and 27 MHz having measured impedances of $103k\Omega$ and $8k\Omega$ respectively. Figure 3.20 shows the equivalent circuit of the Langmuir probe and associated auxiliary electrode sheaths. Where, V_S is the space or plasma potential, V_P is the probe potential, V_b is the probe bias voltage and V_{out} is the output voltage across the current measuring ($R_m = 1k\Omega$ in our case) resistance. The sheath impedance (Z_{sh}) is the parallel equivalent of sheath resistance (R_{sh}) and sheath capacitance (C_{sh}). The impedance of two self-resonating chokes connected in series is represented as (Z_{ck}). Impedance (Z_X) of floating auxiliary electrode is coupled to the probe tip by a coupling capacitor (C_{cp}).

The RF compensation criteria using equivalent circuit analysis is given in equation (3.3).

$$Z_{ck} >> Z_{sh}(\frac{eV_{RF}}{KT_e} - 1) \tag{3.3}$$

$$R_{sh} = (\frac{2\lambda_D^2}{\varepsilon_0 A_P V_B}) \tag{3.4}$$

In our case $R_{sh} \sim 148k\Omega$, $Z_0(= \frac{1}{\omega_{C_0}}$, $c_0 = 0.054\text{pF})$ is the probe capacitance without $V_{RF}) \sim 214k\Omega$ for $T_e \sim 6eV$, $n_i \sim 1 \times 10^{16}m^{-3}$, gives $Z_{sh} \sim 725k\Omega$ for $V_{RF} \sim 50V$. In this situation, without having a choke of impedance $Z_{ck} > 725k\Omega$, it is very difficult to block the RF modulation. Availability of tiny choke of $\sim 103k\Omega$ leaves us with two options; either to reduce Z_{sh} by placing an additional electrode in parallel with the probe or to procure another tiny high impedance choke, which may not be readily available. Sheath resistance relation (equation 3.4) shows that the sheath resistance is inversely proportional to the density and the collection area. Therefore, at low densities R_{sh} increases and takes Z_{sh} away from fulfilling the RF compensation criteria. Placing an auxiliary electrode (A_X) close to the probe having larger area than the probe area ($A_X >>> A_P$) reduces the effective sheath impedance. The Langmuir probe used has an area $(A_P) \sim 1.48 \times 10^{-6}m^2$ and it is chosen an auxiliary electrode with area $A_X \sim 1.58 \times 10^{-3}m^2$. With these parameters, the sheath impedance for the auxiliary electrode in the same plasma is calculated using $R_{sh}(X) \sim 0.148k\Omega, Z_0 \sim 0.214k\Omega$, giving $Z_{sh}(X) \sim 725\Omega$ for $V_{RF} \sim 50V$. Hence, effective parallel equivalent sheath impedance $(Z_{sh(eff)} = Z_{sh} \parallel Z_{sh}(X))$ is reduced to 724Ω. Which is much less than the impedance of the available self-resonating choke and satisfies the necessary RF compensation criteria (equation 3.3). The coupling capacitor has been chosen $10nF$, which allows the high frequency 13.56MHz ($X_C = \frac{1}{2\pi f C_{cp}} = 11.74\Omega$) to pass, but stops the low frequencies. This coupling capacitor plays an important role by stopping the low frequency or the dc current collected by the large auxiliary electrode. Otherwise, it will distort the entire single Langmuir probe characteristics.

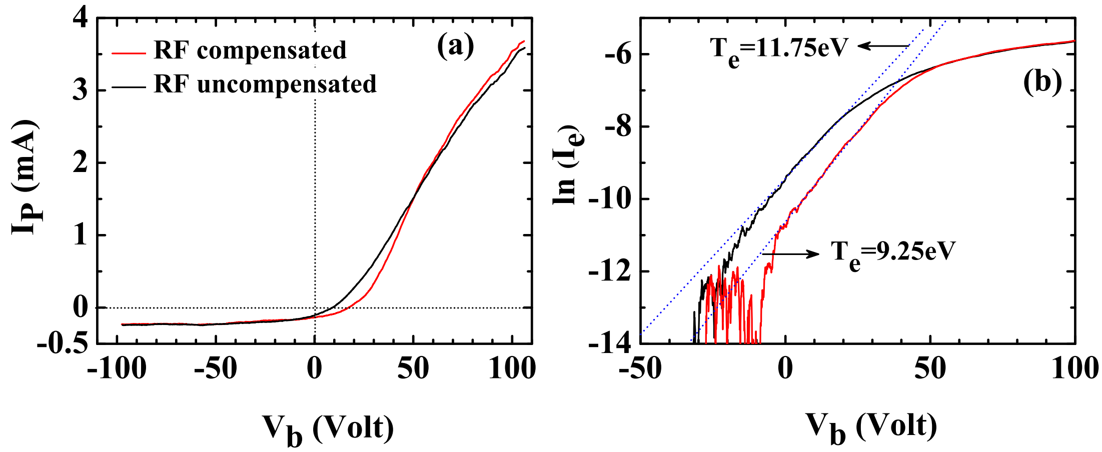

Figure 3.23: Represents the comparison of single Langmuir probe (I-V) traces for RF compensation and RF un-compensation at $(r, Z) = (0, 60)$ cm, 200W and 2×10^{-4}mbar pressure, (b) represents the corresponding semi-logarithmic electron current plots to determine electron temperature, in 3 to 7 magnets configuration.

Implementing the circuit architecture as shown in figure (3.21), the probe assembly has been inserted in the experimental system. Plasma is produced at 200W with Argon fill pressure 2×10^{-4}mbar. Langmuir probe is biased using a ramp signal generated by XR2206 IC with output amplification by power amplifier PA85 IC to get $\pm 110V$ at 11Hz frequency. The LP current is measured across a current measuring resistance ($1k\Omega$) giving the $I - V$ characteristics. Data has been acquired using TDS3034C oscilloscope. To obtain the measurement of electron energy probability function (EEPF), the output signal across $1k\Omega$ is fed into a two stage analog differentiator circuit, where each stage is separated using buffer ICs to get-rid from the impedance mismatching in between the cascading stages. The final output signal after double differentiation gives EEPF. The electron temperature can be measured from the semi-logarithmic plot of electron current obtained after subtracting the ion current contribution from the entire I-V characteristics versus bias voltage [86–88]. Electron temperature can also be measured from the semi-logarithmic plot of analog EEPF signal with bias voltage. The inverse slope of the linear regime of this plot gives the measurement of electron temperature. Presence of different linear regimes in this plot may indicate the existence of drifted or Bi-Maxwellian distribution of electrons. Both the techniques is used to verify the electron temperature measurements as well as to find the electron distribution function. RF compensated single Langmuir probe signal is processed and analyzed writing a MATLAB code, developed using inbuilt subroutine in it. Two symmetric Langmuir probe tips $\sim$ 5 mm apart are mounted on macor ceramic housing and inserted into the helicon plasma as shown in figure (3.21). One of them is equipped with RF compensation with an auxiliary electrode connected to it, while the other one is uncompensated. Advantage of keeping these two probes together is to obtain real time comparison between the compensated and uncompensated probes. This first hand comparison is important to realize the actual achievement of RF compensation. I-V characteristics from both probes with (red solid line) and without (black solid line) RF compensation is shown in figure 3(a). The probes are placed at $(r, Z) = (0, 60)$ cm. It is clearly seen from figure (3.23a) that the compensated probe showed more positive floating potential ($\sim 10V$ higher) compared to the uncompensated probe. After subtracting the ion current from the whole probe current characteristics for each of the two probe signals, the semi-logarithmic electron current plots versus the bias voltage clearly shows two different slopes as shown in figure (3.23b) for different probes. The linear region of the uncompensated (black dotted line) signal gives electron temperature (T_e) $\sim 11.75eV$, whereas, compensated (red dotted line) gives $T_e \sim 9.25eV$. Significant compensation ($\sim 2.5eV$) in electron temperature compensation is achieved by using ($A_X >>> A_P$) even with the impedance limitation of the available self-resonating choke in low density plasma. Ion density (n_i) calculated from the RF compensated probe is $\sim 3.3 \times 10^{16} m^{-3}$.

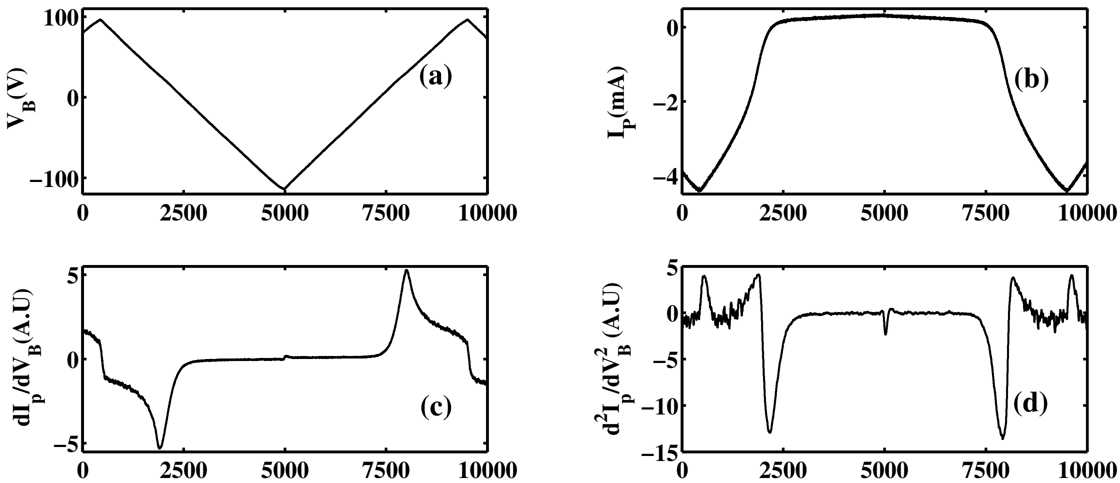

Figure 3.24: (a) Raw data for four simultaneous measurement of applied triangular wave bias voltage, (b) RF compensated probe signal, (c) 1^{st} differential and (d) 2^{nd} differential signal of probe current with bias voltage at $(r, Z) = (7, 65)$ cm, 400W, 2×10^{-4}mbar. X-axis of each plots are the samples, sample interval $= 20\mu s$

.

3.3.3.2 Electron Energy Probability Function (EEPF)

Electron energy distribution function (EEDF) ($f(\varepsilon)$) describes the amount of electrons per unit energy in unit volume. EEDF is found to deviate from Maxwellian at low pressure plasmas. For isotropic electron distribution, taking electron kinetic energy $\varepsilon = \frac{1}{2}mv^2$, where m is the mass and v is the electron thermal velocity, the electron density can be found by the following equation (3.5).

$$n = \int_0^{\propto} f(\varepsilon) d\varepsilon \tag{3.5}$$

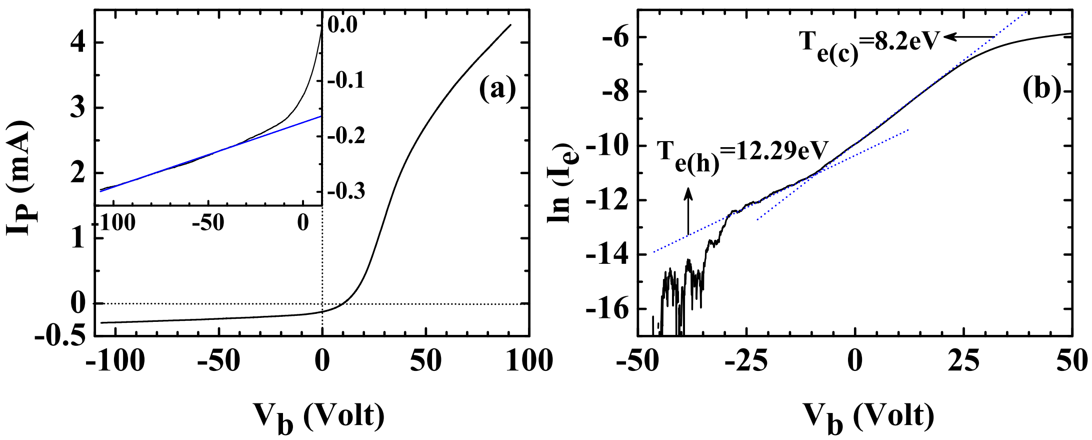

Figure 3.25: (a) Represents the RF compensated single Langmuir probe $(I - V)$ trace at $(r, Z) = (7, 65)$cm with 400W RF power, 2×10^{-4}mbar. The ion current part is magnified in the inset and blue line is the ion current contribution, which is subtracted from the entire probe current. (b) The semi-logarithmic plot of remaining electron current with bias voltage in 3 to 7 magnets configuration.

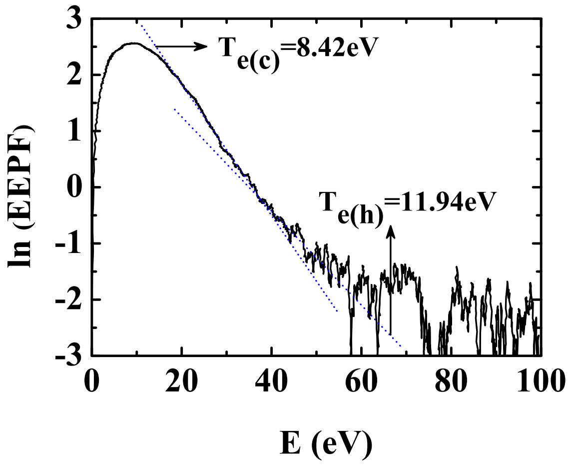

Figure 3.26: Semi-logarithmic plots of electron energy probability function (EEPF) with the electron energy is taken at $(r, Z) = (7, 65)$cm with 400W RF power, 2×10^{-4}mbar.

where Maxwellian electron energy distribution is defined as

$$f(\varepsilon_e) = \frac{2}{\sqrt{\pi}}(kT_e)^{-3/2}\sqrt{\varepsilon_e}e^{-(\varepsilon/kT_e)} \tag{3.6}$$

The function $g(\varepsilon) = \frac{f(\varepsilon)}{\sqrt{\varepsilon}}$ is often referred to as the *electron energy probability function* (EEPF).

$$g(\varepsilon) = \frac{2}{\sqrt{\pi}}(kT_e)^{-3/2}e^{-(\varepsilon/kT_e)} \tag{3.7}$$

The relation between the second derivative of probe current (I_P) to the probe bias voltage (V_b) was given by Lieberman (equation 3.8) [89].

$$g(\varepsilon_e) = \frac{f(\varepsilon_e)}{\sqrt{\varepsilon_e}} = \frac{\sqrt{8m_e}}{e^{3/2}A_P}\frac{d^2I_P}{dV_b^2} \tag{3.8}$$

Where $\varepsilon_e = e(V_S - V_b)$ is the electron energy in eV, with $V_b \leq V_S$. Equation (3.8) represents the direct second differentiation of electron current with the bias voltage is the normalized EEPF. Analog double differentiator circuit has been used to determine the second derivative of probe current with respect to bias voltage. Numerical double differentiation is also another way, however numerical differentiation enhances the noise already present in the raw Langmuir probe ($I-V$) characteristics, which is ignorable in many cases. To avoid large amount of data smoothing, which often introduce error while determining plasma parameters. Thus analog differentiation has been adopted. Direct analog differentiation of probe current to the bias voltage incorporates the ion contribution as well. However, the EEPF measures energy of electron from plasma potential, where the ion contribution is negligibly small. Moreover, this method of determining EEPF is found to be more reliable for (a) most of the plasmas including plasma having non-Maxwellian distribution [89], (b) valid for any geometry such as planner, cylindrical or spherical shape (equation 3.8), (c) this method does not depend on the ratio of probe dimensions to debye length (λ_D) (equation 3.8). For a Maxwellian distribution the logarithm of the EEPF is directly proportional to the inverse electron temperature (equation 3.7) as indicated in equation (3.9).

$$\ln g(\varepsilon_e) = \ln(\frac{d^2I_P}{dV_b^2}) + Constant = -(\frac{\varepsilon_e}{kT_e}) + Constant \tag{3.9}$$

Where the inverse slope in the semilogarithmic plot of $(I-V)$ double differentiation with electron energy gives the electron temperature.

To measure the electron energy probability function (EEPF), RF compensated Langmuir probe system has been inserted to the system off-axis ($r = 7cm$) from one end. An analog double differentiator circuit is used to differentiate the compensated probe current with respect to bias voltage for direct measurement of EEPF. Hardware differentiators score over the traditional numerical techniques, which are inherently noisy and generally yields poor results [90]. The ramp bias and the probe signals are shown in figure (3.24a) and (3.24b). A triangular waveform is generated from XR2206 ICs and amplified using PA85 power amplifier to bias the Langmuir probe. One segment of the triangular waveform consisting of a rising and a falling-part and the corresponding Langmuir probe I - V characteristics are acquired using TDS3034C (Tektronix make) oscilloscope, having 10k data storage length equally distributed between rising and falling ramp voltage. Corresponding to the triangular biasing pulse, the first and second order differentiated signals are also simultaneously acquired in other two channels of the oscilloscope, which are shown in figure (3.24c) and (3.24d). During the descend of the bias voltage from 100 V to -120 V, the probe current rises sharply till floating potential (V_f) and then vary very slowly in the ion region. When the bias voltage ascends from -120 V to 100 V, the probe current first vary slowly in the ion region and decreases sharply then after (figure 3.24b). First differentiation of the probe current shows a negative peak and positive peak (figure 3.24c) corresponding to rising and falling part of the probe current. Note that the differential circuit is an inverting one. The output of the second differentiator shows two negative peaks (figure 3.24d) corresponding to two positive slopes appeared in the positive and negative peaks of the first derivative of the probe current. The second differentiator is also an inverting one. At $\sim 35V$ of bias voltage, the first derivative of probe current maximizes and the second derivative attains zero values. This voltage represents the plasma potential. Simultaneous acquisition of all the four time series data are analyzed using the subroutines in MATLAB. The RF compensated Langmuir probe (I-V) characteristic is plotted in figure (3.25a). After proper subtraction of ion current (shown in the inset of figure 3.25a) from the entire probe current, electron temperature is estimated from the semi-logarithmic plot of electron current with bias voltage. Figure (3.25b) clearly shows two distinct linear regimes, representing two different electron populations in the helicon plasmas diagnosed with RF compensated Langmuir probes. The slope near the plasma potential (V_S) represents the cold or Maxwellian electrons and the slope away from the V_S represents the electron temperature for drifted Maxwellian distribution. The presence of drifted Maxwellian electrons are further verified by analyzing the double differentiated signals. The direct double differentiation of the $(I - V)$ characteristics gives the electron energy probability function (EEPF). The electron temperature is obtained from the semi-logarithmic plots of EEPF with the electron energy as shown in Figure (3.26). Figure 3.26 also shows two distinct linear regions which correspond to two electron population with different temperatures. The slope near the low energy electrons represents cold or Maxwellian electrons and the slope with high energy tail represents the drifted Maxwellian electron temperature. The cold electron temperatures ($T_{e(c)}$) estimated from figure (3.25b) and figure (3.26) are respectively $8.2eV$ and $8.42eV$. The hot electron temperatures ($T_{e(h)}$) estimated from figure (3.25b) and figure (3.26) are respectively $12.29eV$ and $11.94eV$. Both cold and hot electron temperatures, estimated by applying two techniques, are found to be in close agreement. This confirms the production of two component electrons in our helicon antenna produce radio frequency plasma. Ion density (n_i) considering cold electron temperature ($8.2eV$) is $\sim 4.3 \times 10^{16} m^{-3}$.

Experimental results showed in this section established that it is possible to get RF compensation by increasing the area of the auxiliary electrode particularly at low density plasma ($\sim 10^{16} m^{-3}$), when there are limitations from getting very high impedance ($\sim 500k\Omega$) self resonant tiny choke. Two temperature plasma is observed in our low density helicon antenna produce radio frequency plasma. Hot electrons are observed only at off-axis as the on-axis measurement (figure 3b) does not have any indication of presence of energetic electrons.

3.3.4 Double Langmuir probe

Langmuir probes in different configurations namely single Langmuir probe (SLP), double Langmuir probe (DLP), triple Langmuir probe (TLP) are universally used to measure plasma parameters of low temperature laboratory plasmas such as plasma potential (V_p), floating potential (V_f), plasma density (n_p), electron temperature (T_e) [91], and electron energy distribution function (EEDF) [92–94]. Single Langmuir probe having only one metallic pin generally requires an application of voltage sweep to obtain current (I)-voltage (V) characteristics of the probe, from where it is possible to estimate aforementioned plasma parameters. However it requires a well-defined voltage reference and also the temporal resolution is limited by the sweeping time of the applied voltage. This problem can resolved by using a symmetric double probe [95] in which two metallic pins are kept close to each other assuming floating potential does not vary in the region where the probe exists and biased with respect to one another hence removing the requirement of any alternative reference.

In double Langmuir probe, any two metallic pins of the triple probe assembly are biased with respect to each other to obtain a current-voltage (I-V) characteristics curve. For Maxwellian plasma, T_e can be obtained from this I-V characteristics using the equation (3.10) [89].

$$T_e = \frac{I_{isat}}{2\frac{\delta I_p}{\delta V_B}\mid_{V_B=0}} \tag{3.10}$$

$I-V$ characteristics obtained using the double probe configuration using all three available combinations of two pins in the diffusion and source chamber respectively are shown in figure (3.27a), (3.27b) and (3.27c). Identical nature of the $I-V$ characteristics of any two probe-pin combinations confirms that all the three probes are symmetric and sampling same plasma region. T_e has been calculated from the slope of the $I-V$ characteristic curve using equation (3.10) and T_e values for all three possible double probe configurations have been tabulated in table 3.1. The table 3.1 also shows the density values estimated by the double probe in the source

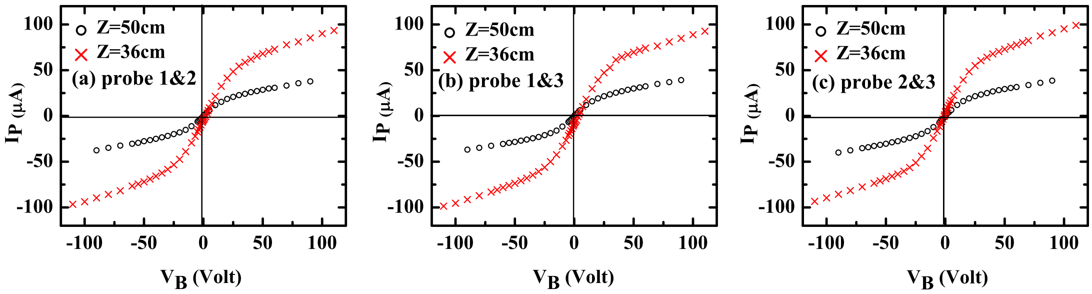

Figure 3.27: Double probe characteristics both at source ($Z = 36cm$) at the diffusion chamber ($Z = 50cm$) at 5.5×10^{-4} mbar and 200W. (a), (b) and (c) are showing ($I - V$) characteristics of active probe-pin combination 1&2, 1&3 and 2&3 respectively

and diffusion chamber.

3.3.5 Triple Langmuir probe

In double probe either manual or electronically voltage sweep is required like the single probe to obtain I-V characteristics which again limits its temporal resolution and analysis is time consuming. Triple Langmuir probe overcomes this limitation, which uses three metallic pins and neither requires any extra reference nor the voltage sweep to measure electron temperature, density and floating potential. Hence it allows instantaneous measurement of electron temperature (T_e), density (n_p) and floating potential (V_f), as well as their fluctuations [96]. Triple probe gives enhanced temporal resolutions compared with other configurations [97] and are better suited for measurements of plasma densities and temperatures in time varying plasmas [98]. Further, it eliminates tedious procedures usually required for obtaining plasma parameters from measured $I - V$ characteristics in both single and double probes.

Although, the conventional triple probe method is very much useful for instantaneous measurements, but due to non-uniform potential distributions of three probes [99] and inappropriate choice of bias voltage, it underestimates or overestimates electron temperature compared to double and single probe measurements in different situations and require compensation to obtain correct temperature values. Compensation of electron temperatures using triple probes are often neglected and there are very few studies mentioning departures from double probe measurements are available in literature [100]. The compensating factor, W can be estimated theoretically as described in reference [99] and shown to be depending on floating potential at the probe location, working gas and bias voltages applied to the probe pins. However to the best of our knowledge, systematic experimental verification of compensating factor and their dependence on the above mentioned parameters to obtain proper matching of temperature values between triple and double probes are not available. Hence it is important to carry out tailored experiments to obtain dependency of compensating factor on floating potential and bias voltages on probe-pins experimentally. Results showed the departure of electron temperature values measured by triple probe compared to that obtain by double probe, determination of proper compensation factor and its dependency on the bias voltage on probe-pins in different experimental conditions [75]. It is observed that temperature overestimation by triple probe compared to double probe is more pronounced when the relative (between probe-pins 1 and 3) bias voltage (V_{d3}) is closely comparable with potential between probe-pins 1 and 2 (V_{d2}). The experiments are carried out in helicon plasma experimental system [101], where there exists substantial variation of plasma floating potential (V_f) in the axial direction facilitating the comparison between triple and double probe in absence and presence of compensating factors at different floating potentials.

A triple Langmuir probe having three cylindrical metallic pines of radius (a) 0.5 mm and exposed length (d) 4 mm made up of tungsten separated by 5 mm from each other. The top view of the probe head with photographs of triple probe are shown in figure (3.28). The three pins are kept far enough from each other so that the plasma sheaths of the individual probes do not overlap but not too far that the pins sample the different plasma regions. All the three pins are kept electrically isolated from the grounded conducting metallic diffusion chamber. This assembly of three pins can be used as double and triple Langmuir probes; when only two pins are biased with respect to each other to obtain an I-V characteristics, the assembly acts as a double probe whereas when all the three pins are used the assembly give instantaneous measurements of electron temperature in the triple probe configuration. The electron temperature has been measured along the axis at both source and diffusion chamber of the machine using the above mentioned assembly using both double and triple probe configurations. The assembly is inserted using a high vacuum feed-through from the open end of the diffusion chamber and can be moved axially up to around 15cm inside the source chamber. RF compensated single Langmuir [74] probe having cylindrical metallic pins of radius (a) 0.5 mm and exposed length (d) 4 mm made up of tungsten is also used to measure the plasma parameters.

The exposed lengths of the probe pins are kept along the direction of externally applied axial magnetic field, to avoid the shadowing effect of one probe tip to other. However, electron collection will be better, keeping the probe tip perpendicular to the magnetic field. Depending upon the strength of the magnetic field, probe operation and analysis can be classified generally in three categories, such as weak magnetic field or classical regime, strong magnetic field ($\rho_e \sim a + s$) and very strong magnetic field ($\rho_e < a + s$) [102, 103], where ρ_e is the electron Larmor radius. In very strong magnetic field and high pressure collisional plasma, diffusion is an important parameter which strongly depends on the electron mean free path, Larmor radius as well as shape, size and orientation of the probe [104]. In weak magnetic field ($\rho_i \gg a + s, \rho_e > a + s$) and low pressures ($\lambda \gg a + s$), where ρ_e and ρ_i are the Larmor radius for electron and ion respectively, a is the probe radius, s is the sheath thickness and λ is the mean free path, the classical probe theory holds good. In our case $\rho_e = (1.2 - 0.7)$mm, $\rho_i = (32 - 18)$mm, satisfies $\rho_e > a + s$ and $\rho_i \gg a + s$, and also electron mean free path (λ) $\sim$ few meter at pressure $\sim 1 - 9 \times 10^{-4}$ mbar fulfills $\lambda \gg a + s$. Hence classical probe theory is valid in our experiments. A schematic of the electrical diagram along with potential distribution on both the pins are shown in figure (3.29a). The schematic of potential distribution in three pins of triple probe configuration is shown in figure (3.29b). The pin 1 is biased positively with respect to pin 3 and pin 2 has

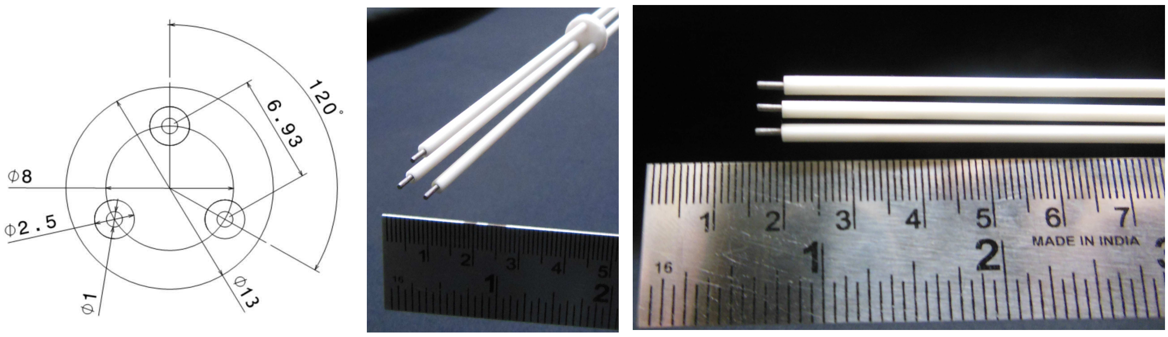

Figure 3.28: Top view of the designed cylindrical triple probe and probe assembly.

kept floating as it is connected to pin 1 through a 10MΩ resistance. The potential at pin 1 with respect to pin 2 is the V_{d2}. The current flowing in all the three probes are given as follows:

$$I_1 = -I_{1e}exp(-\frac{V_1}{T_e}) - I_{1i} \tag{3.11}$$

$$I_2 = I_{2e}exp(-\frac{V_2}{T_e}) + I_{2i} \tag{3.12}$$

$$I_3 = I_{3e}exp(-\frac{V_3}{T_e}) + I_{3i} \tag{3.13}$$

Where I_1, I_2, I_3 are the current flowing through probe-pins 1, 2 and 3 respectively, negative and positive signs represent electron and ion current collection. V_1, V_2 and V_3 are the potentials at the respective probe tips. As pin 1 and 3 remains in the double probe configuration the current flowing through both of them remains the same, i.e. $I_1 = I_3$. Rearranging the above equations (3.11, 3.12, 3.13) along with the condition $I_1 = I_3$ is obtained as

$$\frac{I_1 + I_2}{I_3 + I_1} = \frac{-[I_{1e}exp(-\frac{V_1}{T_e}) + I_{1i}] + [I_{2e}exp(-\frac{V_2}{T_e}) + I_{2i}]}{[I_{3e}exp(-\frac{V_3}{T_e}) + I_{3i}] - [I_{1e}exp(-\frac{V_1}{T_e}) + I_{1i}]} \tag{3.14}$$

All the probe-pins are of equal dimensions, they collect equal electron and ion saturation currents ($I_{1e} = I_{2e} = I_{3e} = I_e$) and ($I_{1i} = I_{2i} = I_{3i} = I_i$). Further as pin 3 is connected to pin 2 through a high 10MΩ resistance, it draws negligible current ($I_2 = 0$), maintaining its floating nature. Hence equation (3.14) reduces to

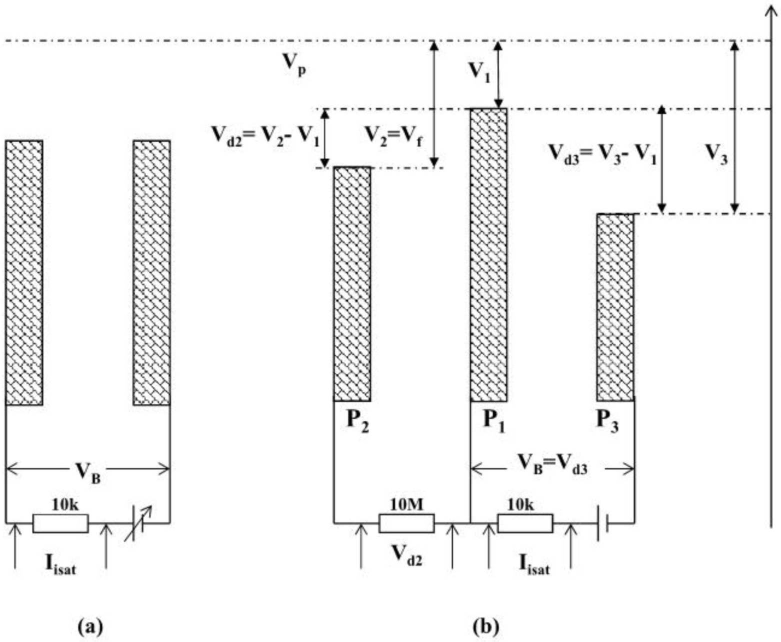

Figure 3.29: (a) is the double probe electrical measurement scheme and (b) is the triple probe potential distribution with electrical measurement scheme.

simplified equation (3.15).

$$\frac{1 - exp(\frac{-V_{d2}}{T_e})}{1 - exp(\frac{-V_{d3}}{T_e})} = \frac{1}{2} \tag{3.15}$$

Where $V_{d2} = (V_2 - V_1)$ and $V_{d3} = (V_3 - V_1)$. When V_{d3}, which is $\sim V_B$ is large compared to V_{d2}, the temperature can be estimated from the following relation (equation 3.16).

$$T_e = \frac{-V_{d2}}{ln(1/2)} = 1.44V_{d2} \tag{3.16}$$

Hence, measuring potential of probe 1 (which is at highest potential) with respect to probe 2, gives the direct measurement of electron temperature (equation 3.16). However, this analytical expression does not involve the small variation of potential dependent sheath expansion on individual probe pins of triple probe.

3.3.6 Comparison of single, double and triple Langmuir probe measurements

To carry out the comparison study of electron temperature measurements using RF compensated single Langmuir probe, double probe and triple probe, measurements are taken at source and diffusion chamber. As the measurement of floating potential in the source and diffusion chamber of the device along the axial direction showed that there exist noticeable variation in floating potential ($V_f = -10V$ to $-30V$) at two different locations in our helicon plasma system while moving from diffusion chamber to source chamber. Hence this region is mainly scanned with double and triple probe for studying the electron temperature mismatch. $I - V$ characteristics obtained using the double probe configuration using all three available combinations of two pins in the diffusion and source chamber respectively are shown in figure (3.27a), (3.27b) and (3.27c). T_e has been calculated from the slope of the I-V characteristic curve using equation (3.10) The electron temperature measurements have been repeated using three probe-pins in the triple probe configuration at the same location keeping all other parameter constant. The T_e values measured with triple probe are found to be substantially higher than those measured by double probe in both source and diffusion chambers. Comparison of uncompensated electron temperature measurement using triple probe with those using double probe for two different floating potential values are presented in first two columns of table 3.2.

The deviation in double and triple probe measurement is due to the fact that in triple probe configuration, close to the ion saturation, three probe-pins are at three different potentials and hence have different ion sheath structure forming around them according to the potential on the pins. The growth or decay of the ion sheath region around the probe increases or decreases the effective area of the probe, which leads to current variation through the pins. For a cylindrical geometry, with collision-less sheath, the incoming ions in the attractive central force of the probe has initial velocity components at the sheath edge $-v_r$ and $-v_\phi$

as indicated in the figure (3.30). Where a is the radius of the cylindrical probe, r is arbitrary radial distance, s is the sheath thickness around the probe. $-v'_r$ and $-v'_\phi$ are the respective velocity components at the surface of the probe. As there is no collision is taking place between the sheath entrance and the probe surface, so energy will be conserved (equation 3.17) and using the momentum conservation ($sv_\phi = av'_\phi$), one can get equation (3.18).

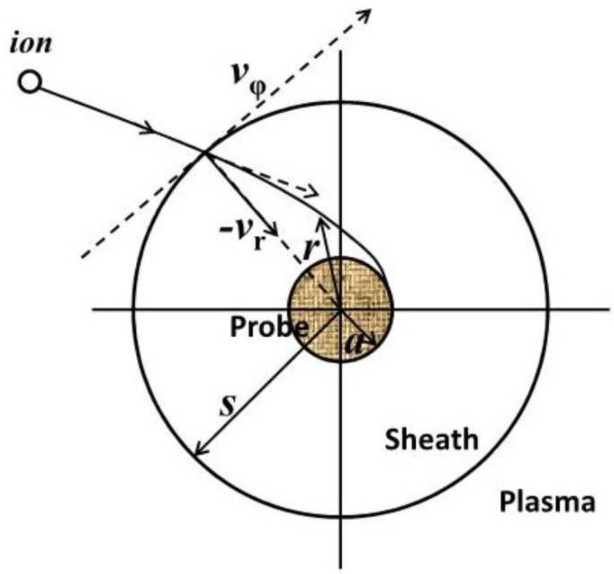

Figure 3.30: Ion collection from plasma to a cylindrical probe

$$\frac{1}{2}M(v_r^2 + v_\phi^2) + e \mid V_p - V_B \mid = \frac{1}{2}M(v_r'^2 + v_\phi'^2) \tag{3.17}$$

$$v_r'^2 = v_r^2 + v_\phi^2\{1 - (\frac{s}{a})^2\} + \frac{2e}{M} \mid V_p - V_B \mid \tag{3.18}$$

Only those ions will reach to the probe, which has $\mid v_\phi \leq v_{\phi 0} \mid$, where $v_{\phi 0}$ is the critical velocity bellow which ion can reach the probe (equation 3.19). When they are reaching at the probe surface, kinetic energy of those particle will be zero ($v_r'^2 = 0$) (neglecting the heating effect and secondary emission from probe surface).

$$v_{\phi 0} = \{\frac{v_r^2 + \frac{2e}{M} \mid V_p - V_B \mid}{(\frac{s}{a})^2 - 1}\}^{\frac{1}{2}} \tag{3.19}$$

In our case, one can assume sheath thickness $s \geq 10\lambda_D \geq 1.25$mm, probe radius $(a = 0.5)$mm, probe length $(d = 4)$mm, $\frac{s}{a} \geq 1$ and $\frac{s}{d} \leq 1$. Hence the infinite cylindrical approximation is valid in our case [89]. If the bias voltage (V_B) which is usually large for ion saturation current. In that situation, one can take the approximation $v_r^2 \ll \frac{2e}{M} \mid V_p - V_B \mid$ and equation (3.19) reduces to equation(3.20).

$$v_{\phi 0} = \frac{a}{s}\{\frac{2e}{M} \mid V_p - V_B \mid\}^{\frac{1}{2}} \tag{3.20}$$

Current collected by the probe can be written as $(i = n_s e v_{\phi 0} A)$, Where n_s is the density at the sheath edge and A is the probe collection area. Substituting $v_{\phi 0}$, one can get potential dependent current equation (equation 3.21). Where probe collection area $A = sd$.

$$i = e n_s a d \frac{a}{s}\{\frac{2e}{M} \mid V_p - V_B \mid\}^{\frac{1}{2}} \tag{3.21}$$

$$i^2 \propto \mid V_p - V_B \mid \tag{3.22}$$

Equation (3.21) is independent of sheath thickness (s), electron temperature (T_e) and ion temperature (T_i). Therefore, the square of the pin current $[I_i(V)]^2$ depends linearly on the bias potential V_{d3} [89, 99].

As define in equation (3.24), β is the gradient of the square of the ion current with potential.

$$\beta = \frac{1}{\Delta V}\frac{[I_i(V)]^2 - [I_i(V_f)]^2}{[I_i(V_f)]^2} \tag{3.23}$$

Geometrical factor (β) depends on the shape, size of probe and condition of the plasma being measured. As the three probe-pins of triple probe are at three different potentials, the ion current collection will be different in all three pins and will depend on this β factor. The ion currents for all the three probe-pins can be written as

$$I_i(V) = I_i(V_f)(1 + \beta \Delta V)^{\frac{1}{2}} \tag{3.24}$$

Probe 2 is at floating potential $V_2 = V_f$.

$$I_i(V_1) = I_i(V_f)[1 - \beta V_{d2}]^{\frac{1}{2}} \tag{3.25}$$

$$I_i(V_2) = I_i(V_f) \tag{3.26}$$

$$I_i(V_3) = I_i(V_f)[1 + \beta(V_{d3} - V_{d2})]^{\frac{1}{2}} \tag{3.27}$$

Incorporating this β factor, equation (3.15) gets modified and can be written in the following form [99].

$$\frac{1 - W(\beta, V_{d2}, V_{d3}) exp(\frac{-V_{d2}}{T_e})}{1 - exp(\frac{-V_{d3}}{T_e})} = \frac{1}{2} \tag{3.28}$$

Where 'W'is called a compensation factor and is given by

$$W(\beta, V_{d2}, V_{d3}) = \frac{[(1 - \beta V_{d2})^{\frac{1}{2}}] + [1 + \beta(V_{d3} - V_{d2})^{\frac{1}{2}}]}{2} \tag{3.29}$$

and

$$\beta = \frac{1 - \frac{exp(\frac{2V_f}{T_e})}{(0.657)^2(\frac{M_i}{m_e})}}{V_f - \frac{T_e}{2}} \tag{3.30}$$

Incorporating the correction factor W and β to the temperature values obtained using triple probe at different pressures, i.e. at different floating potentials, it is obtained the compensated T_e values from triple probe measurement. It can be seen from the table 3.2 that the percentage of overestimation of T_e is $\sim$ 45% in diffusion chamber, where the floating potential V_f $\sim$-9.5 V and $\sim$ 21% at source chamber, where V_f $\sim$-29V with V_{d3} kept constant at $\sim$ 52 V. The compensated electron temperature measurement using triple probe match quite well with those using double probe as tabulated in column 6 of table 3.2.

Table 3.1: Double probe analyzed results

Probe location	Probe combination	Slope $(\frac{\delta I}{\delta V_B})\mid_{V_B=0}$	T_e (eV)	$I_{isat}(\mu A)$	$n_i \approx n_i(m^{-3})$
Diffusion chamber	1 & 2	1.22×10^{-6}	6.96	17	3.89×10^{15}
	1 & 3	1.23×10^{-6}	6.504	16	3.79×10^{15}
	2 & 3	1.28×10^{-6}	6.64	17	3.99×10^{15}
Source chamber	1 & 2	2.46×10^{-6}	10.36	51	0.958×10^{16}
	1 & 3	2.49×10^{-6}	10.64	53	0.983×10^{16}
	2 & 3	2.62×10^{-6}	10.11	53	1.008×10^{16}

Table 3.2: Comparison of electron temperature (T_e) measurement using double probe and triple probe at 5.5×10^{-4} mbar, 200W

Probe location	$DLP\ T_{e(av)}$(eV)	$TLP_{(Uncom)}T_e$(eV)	β	W	V_f(Volt)	$TLP_{(Com)}T_e$(eV)	Overestim(%)
Diffusion chamber	6.70	9.31	0.0704	1.37	-9.54	6.39	45.60
Source chamber	10.37	13.24	0.0282	1.16	-28.88	10.90	21.40

The observed electron temperature at the source chamber is $\sim$ 11eV at pressure 5.5×10^{-4}mbar. Inductive RF plasma sources can produce plasmas with Bi-Maxwellian [92], or other distributions, depending upon the different parameter regimes mainly in terms of fill pressure. However, It has been carried out comparison experiments above $\sim 3 \times 10^{-4}$mbar fill pressure, where plasma distribution remains Maxwellian. In this regime I-V characteristic (figure 3.31a) of RF compensated single Langmuir probe confirms Maxwellian distribution with insignificant contribution from the hot electrons as shown in figure 3.31b. Temperatures estimated from this RF compensated single Langmuir probe measurements are $\sim$ 12eV. Temperatures $\sim$ 10 eV are obtained in other inductive RF plasma systems in low fill pressures [105][106]. In the device floating potential in the source

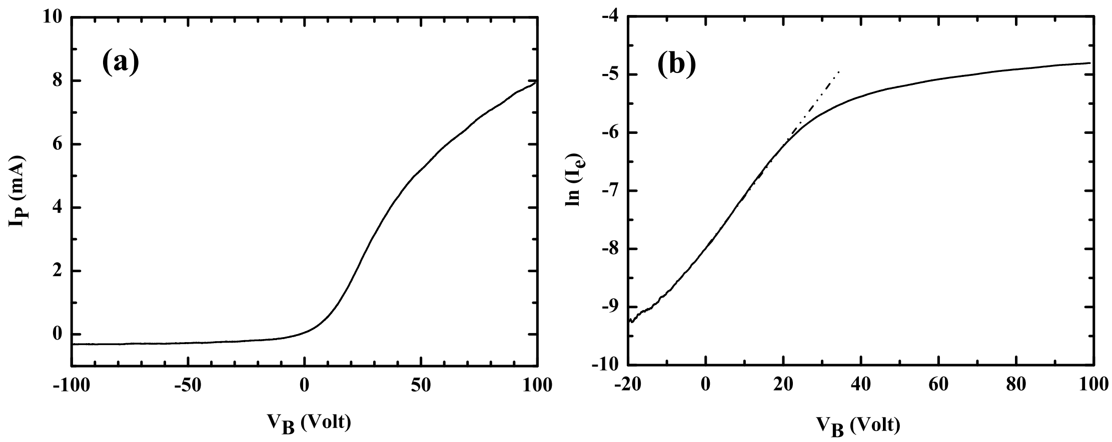

Figure 3.31: (a) RF compensated single Langmuir probe (I-V) characteristic and (b) $ln(I_e)$ with bias voltage, Electron temperature $T_e = 11.88$eV at 5×10^{-4}mbar.

and diffusion chambers can be varied by changing the gas fill pressure. To observe the effect of floating potential on the temperature estimation using triple probe and also on the correction factor and β in a systematic way, measurements are made at two different axial locations one in source and one in diffusion chamber with pressure variation in the device. The two locations of measurement are 36 cm (source chamber) and 50 cm (diffusion chamber) identified with their distance away from the antenna center. The variation in plasma floating potential V_f with pressure at these locations are shown in figure (3.32). It is clear from the figure that the floating potential varies from $(-15$ to $-30)V$ and $(-10$ to $-2)V$ in the source and diffusion chamber respectively. Electron temperature measurements at these pressures enable us to obtain temperature measurements at different floating potentials. The uncompensated values of temperature obtained using triple probe with V_{d3} kept fixed at $52V$ at the above mentioned pressure range is plotted in figure (3.33). As the parameter β depends on the floating potential and the correction factor W depends on β, V_{d2} and V_{d3} (kept constant $\sim 52V$), both are plotted verses the pressure in figure (3.34a and b) respectively essentially to obtain their values at different floating potentials in source and diffusion chamber. Again incorporating the respective values of W and β at different floating potentials it is obtained the compensated values of T_e as a function of pressure as plotted in figure (3.35). The overestimation of electron temperature without the correction factor is shown in figure (3.36). Measurements indicate (figure 3.36) that when plasma V_f is more negative $(< -15V)$, percentage of overestimation introduced into the temperature measurement using direct display triple probe is less $\sim$ (20 to 25)% compared to less negative $V_f(> -10V)$, where the percentage of overestimation is $\sim$ (40 to 70)%.

Further it is observed that although the criteria $V_{d3} > V_{d2}$ is necessary for the temperature measurements using triple probe as described in equation 3.16, it is not sufficient for obtaining similar values as measured by double probe. The discrepancy is coming due to the dependency of compensation factor (W) on bias voltage V_{d3} and hence it is important to choose appropriate V_{d3} for correct triple probe measurements. The compensated and uncompensated electron temperatures measured with triple probe as a function of V_{d3} at three different pressures have been plotted in figure (3.37). The double probe T_e measurements are indicated by the horizontal dash- dot line. It is clearly evident from the figure (3.37) that at higher bias voltage (V_{d3}), even the compensated T_e by the triple probe is giving higher value and below a certain bias voltage, it is giving lower electron temperature, compared to the corresponding double probe measurements. The

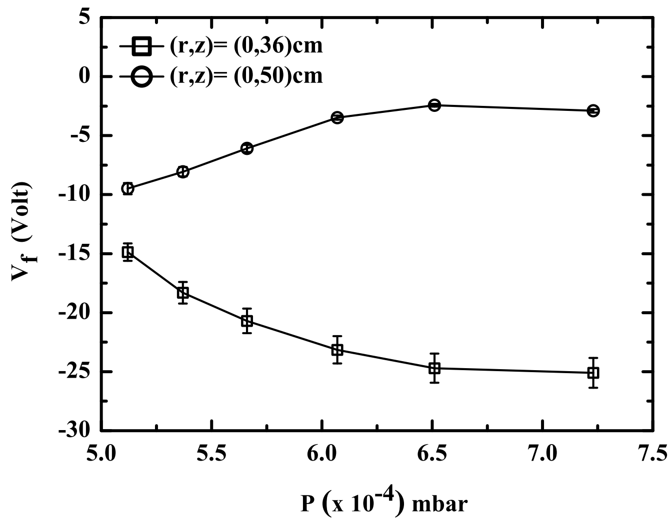

Figure 3.32: Floating potential (V_f) variation with pressure both at source and diffusion chamber.

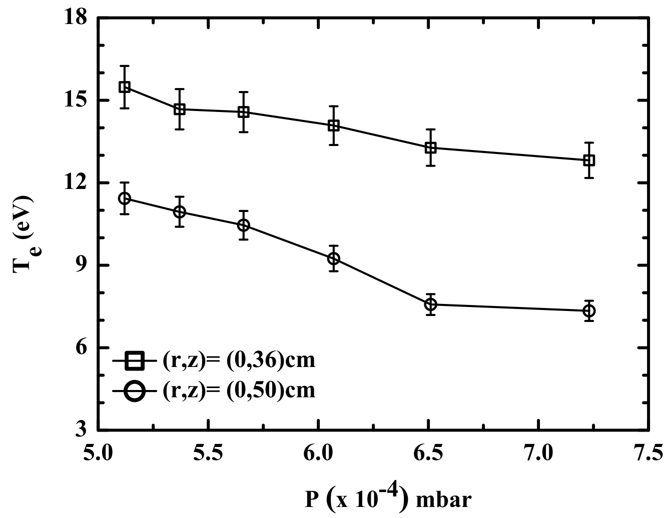

Figure 3.33: Triple probe overestimated electron temperature (T_e) variation with pressure both at source and diffusion chamber.

compensated T_e with triple probe and T_e measured with double probe are found to be matching fairly well in a range $5V_{d2} < V_{d3} < 10V_{d2}$ of the bias voltage (V_{d3}) in three pressure ranges, i.e. with three different plasma floating potentials. If the bias voltage (V_{d3}) is above $10V_{d2}$, compensated T_e values using triple probe are higher than double probe values whereas if the bias voltage (V_{d3}) is less than $5V_{d2}$,

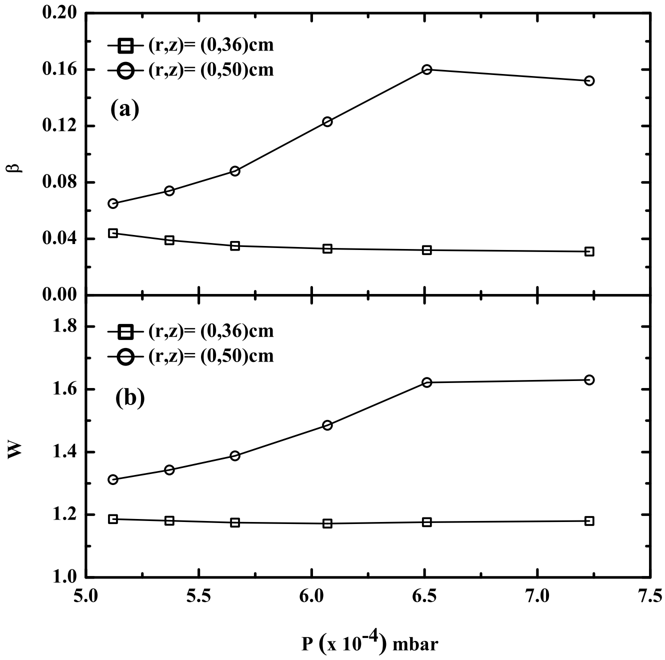

Figure 3.34: (a) Geometrical (β) and (b) compensation factor (W) with pressure both at source and diffusion chamber.

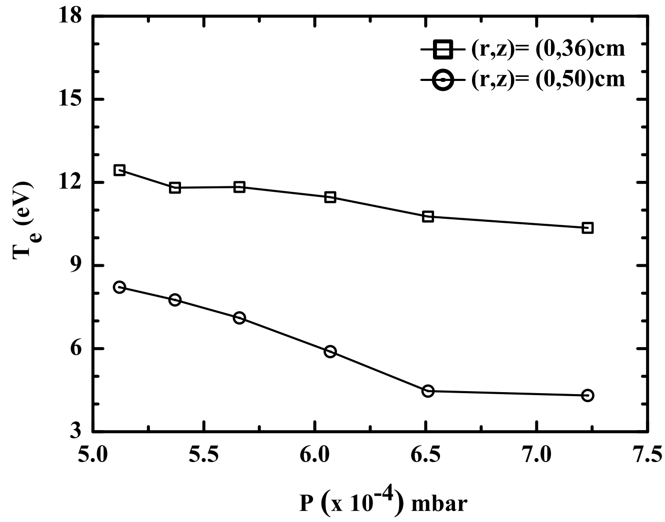

Figure 3.35: Triple probe compensated electron temperature (T_e) variation with pressure both at source and diffusion chamber.

compensated T_e values are found to be less than the corresponding double probe measurements. This may be due to the fact that the relation $I^2 \propto V_B$ remains

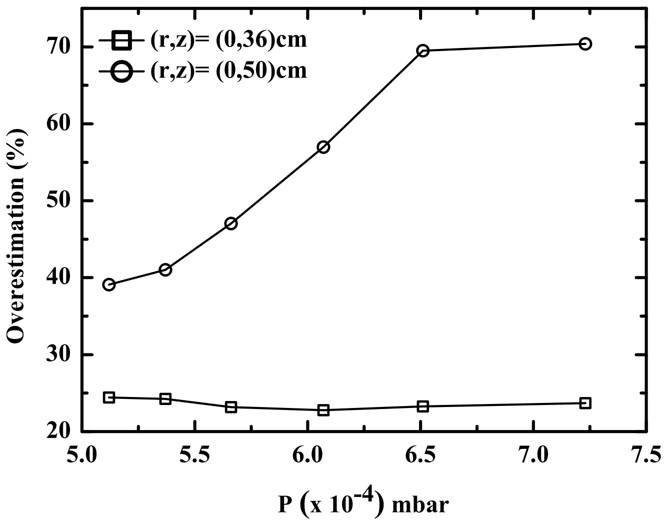

Figure 3.36: Triple probe electron temperature (T_e) overestimation both at source and diffusion chamber.

linear only in an intermediate bias voltage range for cylindrical probe [107]. At lower bias when $V_{d3} < 5V_{d2}$ probe is at a potential which is quite bellow that of its ion saturation, whereas at higher bias particularly when $V_{d3} > 10V_{d2}$, ions enters to the sheath too fast to be absorbed by the probe therefore creating a space charge limited zone around the probe.

Choosing proper bias voltage i.e. V_{d3} the compensated electron temperature measurements using triple Langmuir probe along with respective measurements using double probe versus pressure are plotted in figure (3.38). Both values match fairly well at all pressures i.e. at all floating potentials. Requirements for different V_{d3} is also shown in the same figure for getting the proper match between triple and double probe electron temperature measurements.

The observed anomaly in the electron temperature measurements using double and triple Langmuir probe has been resolved by properly compensating the measured temperature values by triple probe. It has been shown experimentally that the compensation factor (W) is not a constant factor in a plasma where there exists substantial variation in plasma floating potential (V_f). When the plasma floating potential (V_f) is more negative ($< -15V$) then the overestimation of T_e

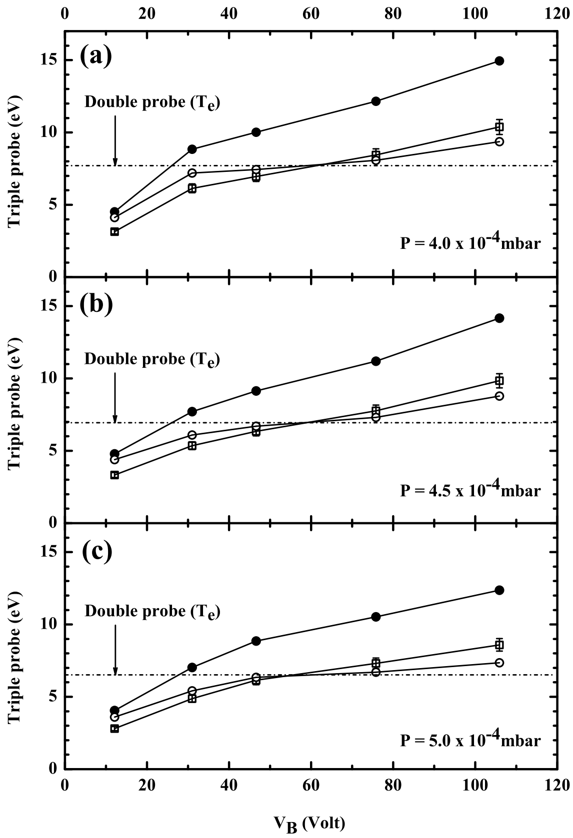

Figure 3.37: Triple probe electron temperature at three different pressures (a) 4×10^{-4}mbar, (b) 4.5×10^{-4}mbar, (c) 5×10^{-4}mbar with bias voltage. Open square data points are the V_{d2} measurement, solid circle data points are the uncompensated T_e and open circle data points are representing compensated T_e. Double probe T_e measurement indicated by the horizontal dash-dot line at three pressure plots.

using triple probe is less dominant ($< 25\%$) and the value of compensating factor W approaches towards unity. However for floating potentials above ($> -10V$), the overestimation increase with increase in floating potential and reaches up to $\sim 70\%$ at floating potential near $0V$ and the compensating factor also has to increase substantially to obtain temperature estimate similar to that measured by double probe. As the compensating factor depends on floating potential of the plasma where the measurements are made and also on the bias voltage (V_{d3}) applied to the two pins of the triple probe, it has been shown that the bias voltage

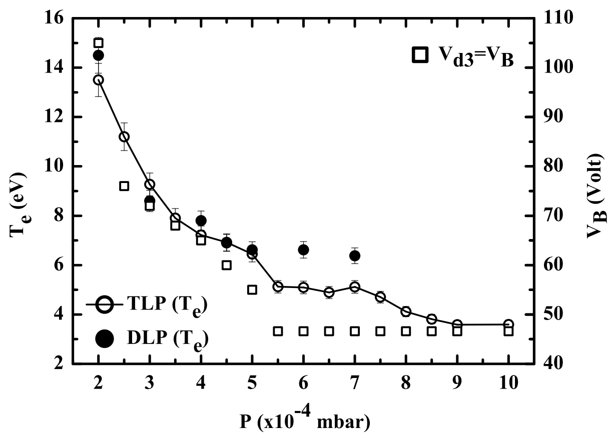

Figure 3.38: Triple probe and double probe electron temperature comparison with appropriate choice of triple probe bias voltage.

(V_{d3}) has to be in the range $5V_{d2} < V_{d3} < 10V_{d2}$ to get proper compensation. Keeping the bias voltage V_{d3} more than 10 times V_{d2}, the temperature values are under-compensated and become more than the double probe values whereas keeping V_{d3} less than 5 times V_{d2}, the temperature estimates using triple probe remain under-compensated and gives lower values than double probe values. The properly compensated T_e values measured using triple probe with keeping the V_{d3} in the range $5V_{d2} < V_{d3} < 10V_{d2}$ matches fairly well with measured values using double probe in a wide range of $(0 \text{ to } -30)V$ floating potential.

In the helicon plasma experimental system, the plasma is created inside a smaller source chamber and expanded into a large diffusion chamber using external axis- symmetric diverging magnetic fields. As in any isothermal system, if the volume gets expanded then to maintain heat conservation, temperature has to drop down, so it is expected to have warm plasma $\sim (10-13)$eV inside the source chamber and relatively cold plasma $\sim (4-8)$eV in the diffusion chamber. The temperature measurements of $\sim 10eV$ and $\sim 6eV$ in source and diffusion chambers respectively using double probe and compensated triple probe matches quite well with the expected values.

3.3.7 Emissive probe

Electron emission from probe or filament provides direct measurements of the plasma or space potential (V_S). When the emitted probe/ filament bias is less than the plasma potential, electrons will escape into the plasma and appear as an effective ion current. When the filament bias is more positive than the local plasma potential, electrons emitted from the probe are reflected back to the probe. This process is not sensitive to plasma flow because it depends directly on plasma potential rather than electron kinetic energy and it is also less sensitive to probe surface contamination when heated surfaces provide electron emission [86]. Due to emission of electron by the heated filament in the plasma, it attends more positive potential. Therefore, the heated filament emits electrons into the plasma and with increasing filament heating current electron emission increases. As the more electrons are emitted from the filament surface, they leave more positive potential at the filament surface. Hence the potential difference between the probe and the plasma potential (which is the most positive potential in plasma) decreases. At lower heating current when the emission is small then these electron will easily move inside the plasma due to acceleration by the higher plasma potential. Whereas at relatively higher emission current (near the filament saturation emission current of 0.125mm tungsten filament), the filament potential reaches close to the plasma potential. The emitted electrons will then be confined near the filament surface regime and creates a space charge. This negative space charge will not allow farther electrons to emit from the filament surface. When this situation is reached then potential of the filament will reach to a saturation, which is the plasma potential at that location of the plasma. This characteristic is shown in the figure (3.39a), where the potential reached to the saturation $\sim 3.3A$ filament current and the plasma potential is 78V. This method of measuring plasma potential is known as floating potential method with large emission current. There are other methods such as inflection point method and separation technique. In inflection point method filament is heated below its maximum emission current and take the current voltage characteristic like single Langmuir probe and its first differentiation shows a peak near the knee of the electron saturation is called the plasma potential. This method is useful to reduce the space charge effects associated with the maximum emission floating potential method. Taking the similar I-V characteristic with various moderate heating current in inflection point of the emitting probe and extrapolate a straight line fit to the zero emission gives more accurate measurement of plasma potential. However, it is difficult to identify inflection points when noise or RF oscillation is present. The inflection point method can not measure temporal variations easily and is difficult to use in high energy density plasmas. Moreover this method is very time consuming to measure plasma potential at one location, compared to floating potential method. Typical separation technique measures collecting and emitting currents with the bias voltage and the point corresponding to a bias voltage from where the separation starts, called the plasma potential. Plasma potential measured using this method is focused to be higher compared to other two methods. The floating point method can measure the potential in a sheath and in presence of beam and double layer plasma. In this method the floating potential is measured across a high ($\sim M\Omega$) resistance connected between the emissive probe and ground, which makes the measuring resistance much higher than the sheath resistance. Therefore, the probe floats at the floating potential and makes the measurement accurate.

$I - V$ characteristics of emissive probe is taken at various filament heating current as shown in figure (3.39b). When the emission current is zero called cold probe characteristic. With increasing heating current electrons starts emission from the filament which is opposite to the ion collection by the probe. Therefore, by increasing the filament current electron emission is increased and the total effective ion current ($I_i - (-I_{e-emit})$) increase in the negative bias regime of the cold probe characteristic. The floating potential point which is the balance potential to make the total zero electron and ion current will move towards the more positive side of the bias voltage and when this V_f reached to the plasma potential ($I_i = 0, I_{e-emit} \sim I_{e-collection}$). All the characteristic curve with different filament emission current

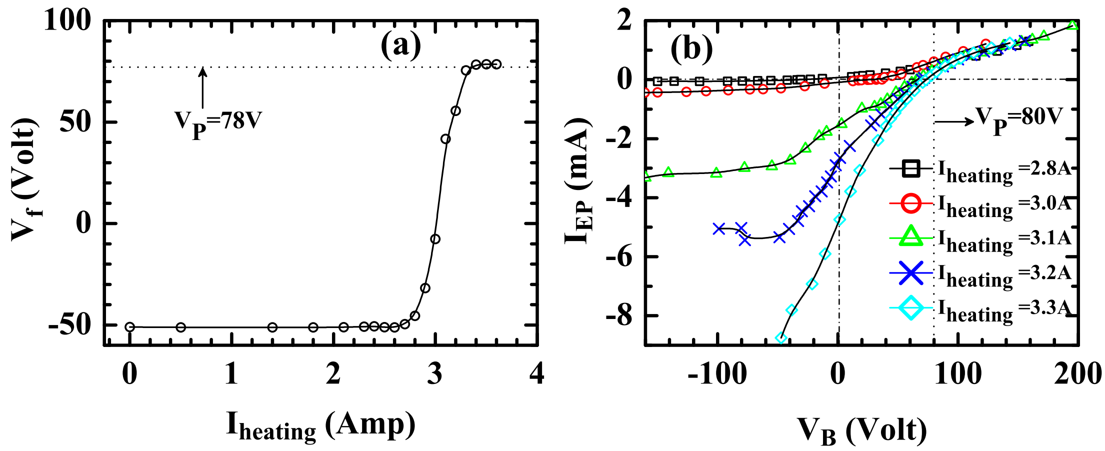

Figure 3.39: (a) Emissive probe (EP) characteristics and (b) comparison of plasma potential measurement with different filament heating currents.

fulfill this condition at a floating potential called the plasma potential. In our case all those curve passed through a point ($V_P \sim 80V$) (figure 3.39b). Which is very close to the ($V_P \sim 78V$) (figure 3.39a) measured from the heating current with V_f characteristic.

There are various method of heating filament such as direct Joule heating, laser heating, RF heating etc. It is used Joule heating for thermonical emitting electrons from the surface of thoriated tungsten wire. Shape of the filament and its housing and electrical connection are also very important for probe to operate long time in plasma. The detail of filament housing inside a double bore ceramic housing is shown in figure (3.40). Where the tungsten filament is push fitted into two Cu tube via two tiny ceramic beads. The opposite end of this Cu tube is connected to the two current carrying wires inside the double bore ceramic tube. This electrical arrangement overcome the difficulties of connecting tungsten filament with the Cu wire. Moreover this simple tungsten to Cu push fit arrangement provides flexibility on easy replacement of filament after long hours of plasma operation. Important role of using two small ceramic beads between the Cu tube and tungsten filament have been experimentally investigated. Experiments are carried out for emissive probe plasma life time using both with and without ceramic beads. In the case

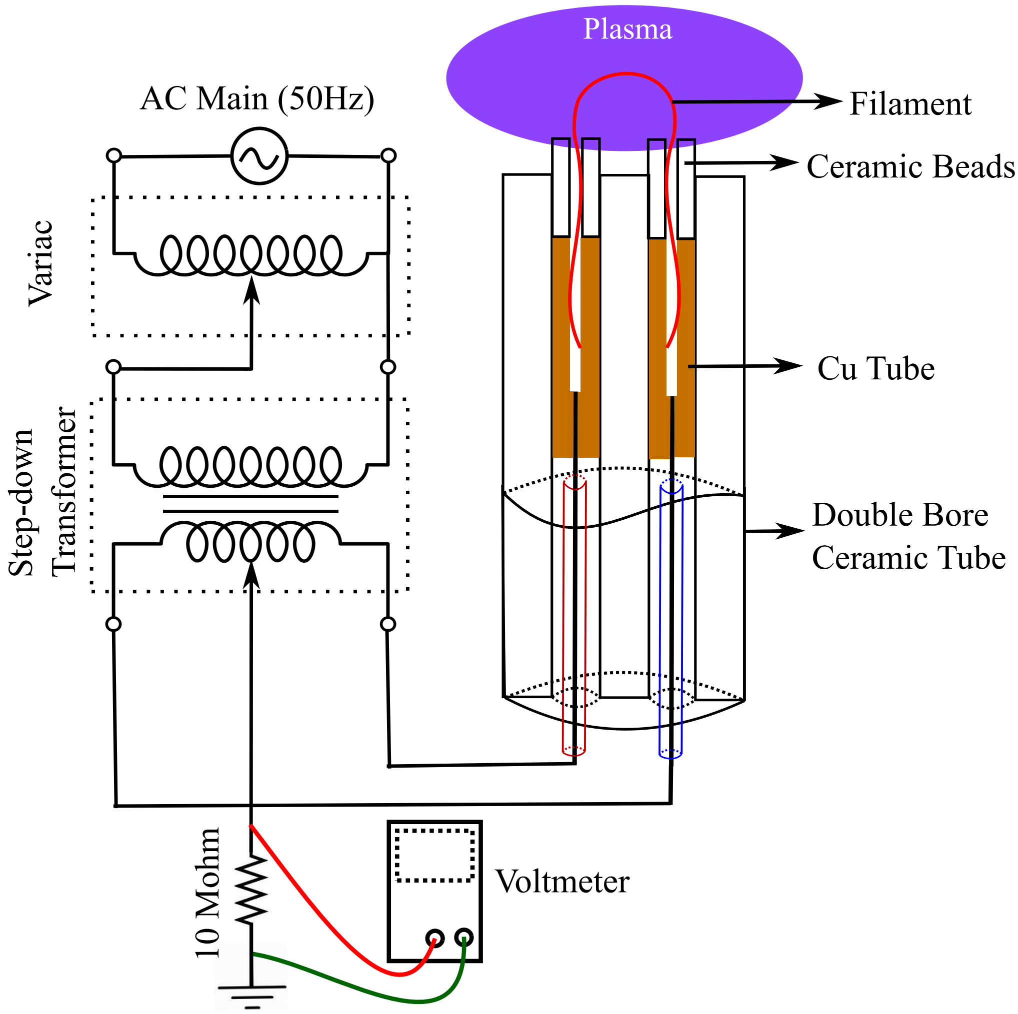

Figure 3.40: Schematic of emissive probe circuit diagram with filament heating current controlled by a variac with 5A/25V step-down transformer. Emissive probe tungsten filament is mounted through ceramic beads and electrically connected to the current carrying wire through Cu tubes, which is housed inside a double bore ceramic tube.

without use of ceramic beads the filament is burned/ broken in every (2-3) hours probe under plasma operation. The filament life time in plasma is observed to be increased by $\sim$ 10 times after introducing two ceramic beads between the plasma exposed filament to the Cu tube. In the case of without ceramic beads case, emission starts from the edge of the Cu tube, and bring some Cu and coated into the tungsten attached ceramic walls. As the time goes under the plasma operation the area of coating with Cu increases on the ceramic walls. Therefore, the electron collection at the V_P will be more than the emission due to large collection area by the Cu coating. Hence the potential on the probe surface will drops down from V_P and to maintain V_P when the filament voltage is increased to increase more emission this Cu coating will even more increased (as shown in figure 3.41b) and electron collection will also be more and probe potential will drops down in few minuets of operation. To compensate this the heating voltage is increased (50Hz) using variac, then heating current will increase and reach to its maximum thermionic emission current, when filament burns. By introducing ceramic beads in between the filament exposed into the plasma from the beads so the emission starts only after the ceramic beads. So the coating of Cu on the wall of ceramic is avoided by introducing these beads and increase the filament plasma lifetime significantly. The photograph shown in figure (3.41), indicates the coating of Cu on the outer wall of the ceramic which has been confirmed by Scanning Electron Microscopic (SEM) examination. The miniaturized filament exposed axial length $<$ 3mm. Therefore the axial resolution is good enough for V_P profile measurement with successive measurement between two points $\sim$ 5mm.

A thoriated tungsten of diameter $0.125mm$ is used for emissive probe. A miniaturized emissive probe filament with plasma exposed length $< 5mm$ has been mounted at the open end of the double bore ceramic tube (OD $4mm$). Two tiny ceramic beads placed on each of the two bores of ceramic tube, significantly improved the working lifetime of the emissive probe. The plasma potential is obtained using floating potential method [76].

3.3.8 RF current probe

The current probe is used to measure the RF current flowing in the antenna, which is needed to determine the effective antenna resistance, and hence find the power transfer efficiency. The current probe used is an (MODEL no. CM-10-P, Serial no. 6130401-1, Ion Physics make) current monitor, which is attached within the RF

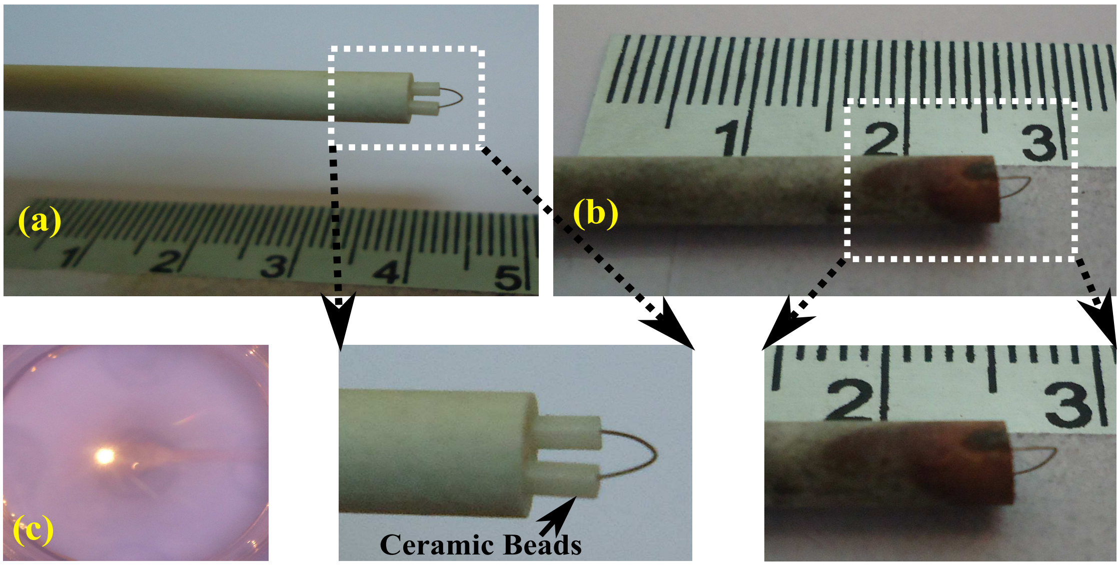

Figure 3.41: Emissive probe (a) with ceramic beads and (b) without ceramic beads. Inset of (b) shows the Cu coating at outer surface of the double bore ceramic attached with the filament. (c) The filament glow in presence of Argon plasma.

shielding enclosure as shown in figure 3.42, and is located into the antenna transmission line. It has a bandwidth of 45MHz, and can measure peak currents of 5kA. The probe consists of an induction coil (similar in many regards to the magnetic probe discussed in Section 3.3.1) that couples to the magnetic field produced from the current carrying conductor, and outputs a voltage signal proportional to the current magnitude. This output signal is acquired using the TDS3034C digital oscilloscope via a 50Ω coaxial cable connected to the BNC output on the RF current probe. A photograph of the current probe is shown in figure 3.42.

The current probe comes pre-calibrated, with a sensitivity factor of 0.1 V/A when plugged into an oscilloscope with a 50Ω feed-through terminator. This terminator is necessary to match the 50Ω design output of the current probe with the much larger $1M\Omega$ input impedance of the oscilloscope. The calibration factor is used to convert the measured voltage from the oscilloscope to an actual current flowing in the antenna. When the antenna/plasma system is matched, the reflected power, P_r , is very small, typically less than 1% of the forward power, P_f , thus almost all of the forward power must be dissipated by the antenna/plasma resistance,

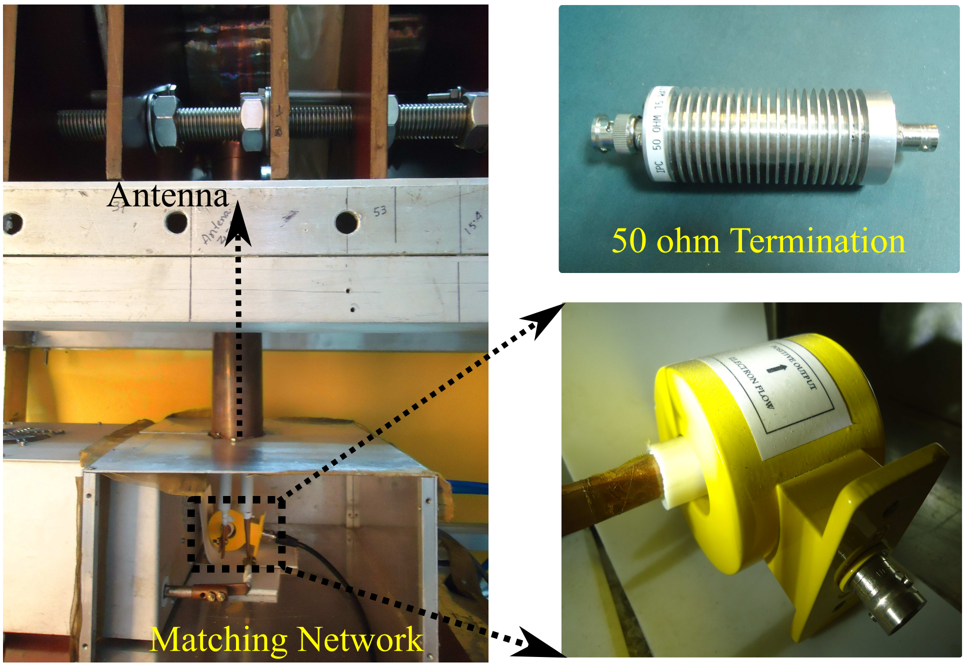

Figure 3.42: Photograph of the RF current probe inserted into the antenna transmission line. Inset shows the probe with BNC output connector. The signal is acquired through this connector, connecting into oscilloscope via the 50Ω, 15Watts termination.

which can be found from $P_f - P_r = I^2_{RMS} R_T$ where $I_{RMS} = I_0/2$ is the root mean square current (measured using the current probe). Here $R_T = R_{ant} + R_p$ is the total antenna, matching network and plasma resistance. Plasma resistance is defined as R_p, and a circuit resistance (antenna and matching network) is R_{ant}. Here R_p represents the effective resistance of all processes that deposit power within the plasma (i.e. capacitive, inductive, and wave coupling). R_{ant} represents the circuit resistance of the antenna/matching network, and includes, ohmic resistance, eddy-current losses, and any contact resistance losses that occur within the matching network between certain components that are joined with a friction fit. Antenna with matching network impedance is measured using the above formula, keeping the chamber pressure $\sim 1 \times 10^{-6}$mbar. Application of RF power into the antenna with suitable adjustment of load (C_L) and tune (C_T) capacitor of the matching network one can make the reflected power (P_r) bellow 1%. In that situation measuring the current monitor signal from oscilloscope and converting the voltage signal with its sensitivity factor to get the rms RF current ($I_{RMS} = 8A$). Using this formula $P_f - P_r = I_{RMS}^2 R_{ant}$ our antenna impedance is calculated is $\sim 0.31\Omega$. The power transfer efficiency, η, is defined as the ratio of the power absorbed by the plasma, P_{abs}, to the total input power from the generator, P_0, and can be written as $\eta = \frac{P_{abs}}{P_0} = \frac{R_P}{(R_P + R_{ant})}$. Helicon wave coupled plasmas have the higher power efficiency (as high as 80 - 90%) [108] [109] compared to inductive or capacitively coupled plasma [110].

4

Multiple Axial Potential Structure (MAPS) formation

4.1 Introduction

In astrophysical system energetic flow of ions has been observed, known as solar corona [111], the Aurora Borealis [5] or extra-galactic jets [7]. One source of these fast ions has been identified as a spatially localized potential drops, called double layer. The spontaneous formation of electrostatic potential structures in a geometrically expanding plasma has great importance to study the ion beam formation mechanism [25, 26]. These structures can have useful application in space plasma thruster. Plasma double layers have been deeply investigated during the last three decades and growing divergingly experimental [2, 4, 112–117], theory [118] as well as simulation [119–121]. In a quasi-neutral plasma it does not allow to have an electric field, but if the plasma quasi-neutrality is locally violated, then plasma will have a local potential gradient. This layer of non-neutral plasma separates two quasi-neutral plasmas called the double layer. This electrostatic potential structure can be static or transient, which forms inside the bulk plasma far away from the sheath edge plasma boundary. One single step double layer is commonly observed in expanding helicon plasma system. However, there is one observation which shows indirect evidence of the existence of more than one double layer [122]. As mentioned earlier in chapter 1, under certain experimental conditions two or more subsequent double layer can be formed [27–29, 31, 32]. These double layers are related with one another and they are called as multiple double layers. In this chapter, it is shown that the multiple double layer like structure has been created in a controlled way.

The rest of this chapter is organized as follows: In section 4.2 double layer like potential structures along with location of maximum of magnetic field gradient, pressure, power and magnetic field strength are discussed. In section 4.3 ion beam generation is presented. Transition from single to multiple axial potential structure with parametric study is presented in section 4.4. Discussion is carried out in section 4.5 followed by summary in section 4.6.

4.2 Double layer like potential structures

Experiments are performed in **he**licon **ex**perimental **(HeX)** system, described in chapter 3. Although the HeX- system composed of 1 to 8 electromagnets, only 3 to 7 among them are used for specific potential structure formation experiments, which is presented in this chapter. The configuration is shown in figure (4.1). Diagnostic used for these experiments are the emissive probe for local plasma potential (V_P) measurements, RF compensated single Langmuir probe for electron energy distribution function (EEPF) measurements, triple probe for local electron temperature and density measurements and retarding field energy analyzer (RFEA) for ion beam energy measurements.

4.2.1 Potential structure with location of $\nabla B_z|_{max}$

Experiments are carried out to find out the double layer like potential structures in this HeX- system. Careful inspection for the formation of double layer like potential

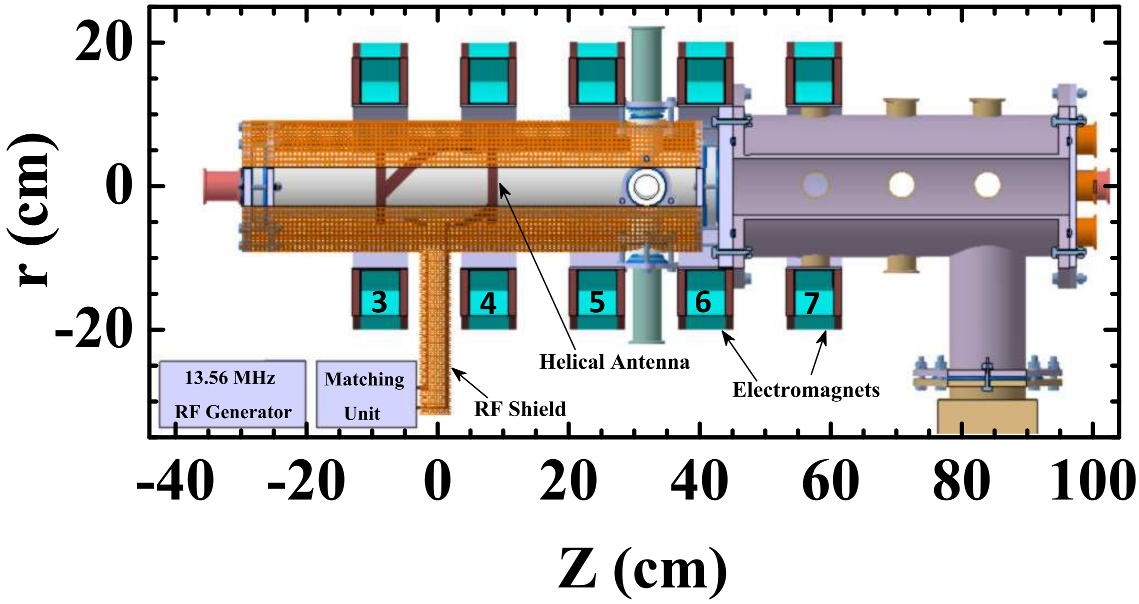

Figure 4.1: 3D-schematic of helicon plasma experimental setup

structures are found to be very sensitive to the magnetic field configuration. For this specific experiment, three different axial B_Z configurations are chosen, as shown in figure (4.2). *Config. 1*: where the maximum of ∇B_Z located inside the source chamber ($Z \sim 30cm$). *Config. 2*: where the maximum of ∇B_Z located close to the geometrical aperture point ($Z \sim 46cm$), we called this as *close magneto geometrical aperture* (CMGA) configuration. *Config. 3*: where the maximum of ∇B_Z located inside the diffusion chamber ($Z \sim 62cm$). *Config. 1* (Black curve) is created by powering only 3 to 5 magnets, *Config. 2* (Red curve) by powering only 3 to 6 magnets and *Config. 3* (Blue curve) where only 3 to 7 magnets are powered.

Axial plasma potential (V_P) measurements are carried out for all the above three configurations at low power (100W) and low magnetic field (220G), shown in figure (4.3). Axial potential profile corresponding to *Config. 1* (Black data points) and *Config. 3* (Blue data points) clearly shows monotonic change of axial plasma potential. It is also to be noted that the overall potential is found to be less for *Config. 3* compared to *Config. 1*. This is due to improvement of confinement time

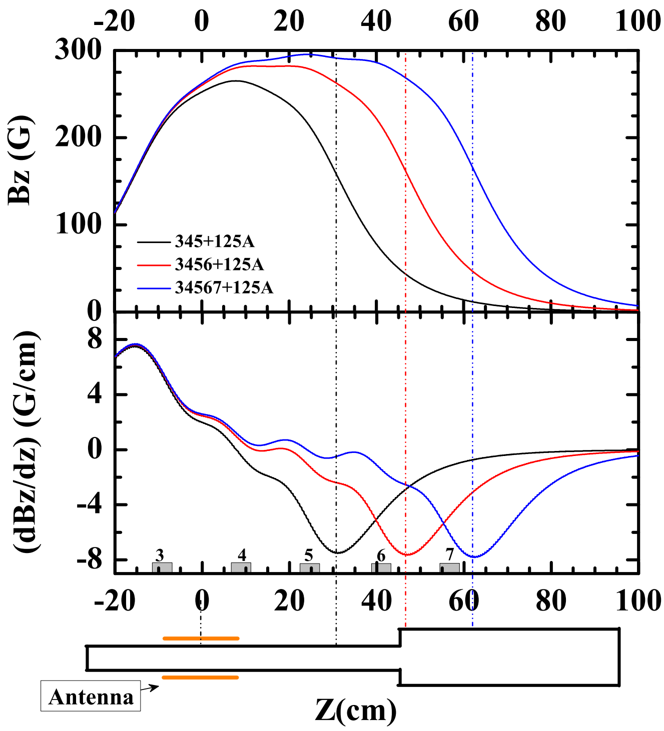

Figure 4.2: Simulated B_z profile showing three different configurations with location of $\nabla B_z|_{max}$ at Z = 30 cm (Black curve), Z = 46 cm (Red curve) and Z = 62 cm (Blue curve).

in *Config. 3*. Negatively charged electron loss rate is more in *Config. 1* compared to *Config. 3*, as the magnetic field lines are touching the conducting wall very close to the throat expansion compared to *Config. 3*. Therefore, electrons will leave more positive potential in the bulk, hence V_P in the bulk plasma is found comparatively high in *Config. 1*. On the other hand, *Config. 2* (Red data) shows a sharp potential fall compared to other two configurations. To validate this results, similar experiments have been carried out at relatively high source magnetic field (290G) (figure 4.4). The results obtain at this parameter space also produce the similar trained. Therefore, these set of experiment resembles the sharp axial plasma potential fall only when the maximum magnetic field divergence closely coincide with the geometrical aperture.

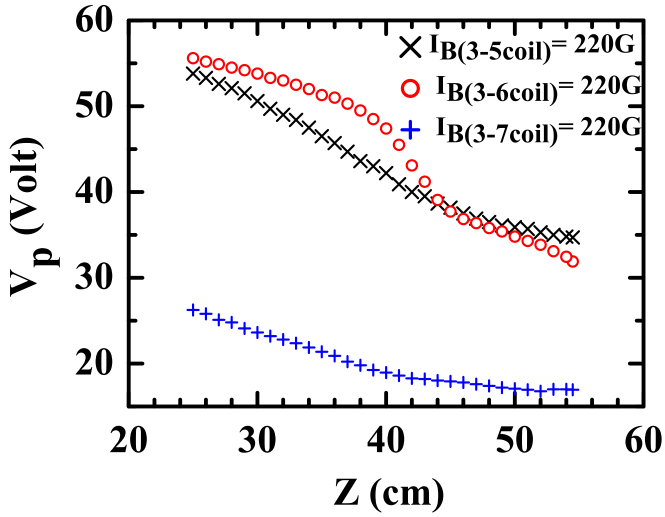

Figure 4.3: Axial plasma potential profile at 2×10^{-4}mbar, with 220G source magnetic field with three different configurations, and 100W RF power.

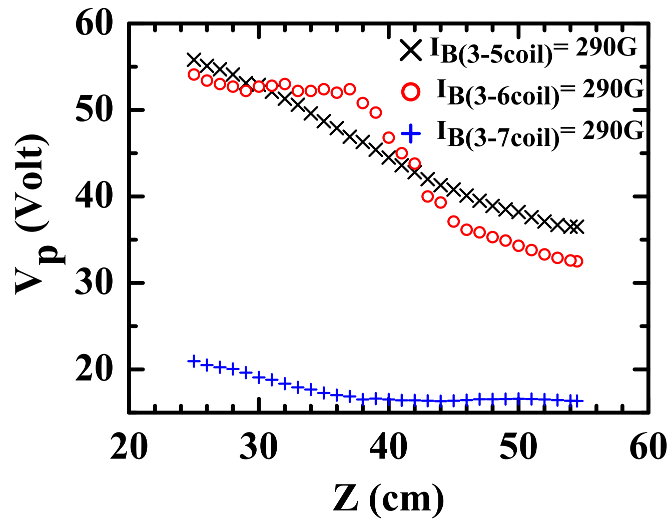

Figure 4.4: Axial plasma potential profile at 2×10^{-4}mbar, with 290G source magnetic field with three different configurations, and 100W RF power.

4.2.2 Potential structure with pressure and magnetic fields

Keeping the maximum magnetic field divergence closely coincide with the geometrical aperture (*Config. 2*), axial potential profile is measured with low ($1 \times 10^{-4} mbar$) as well as high ($1 \times 10^{-3} mbar$) Ar fill pressure (figure 4.6). Potential fall is observed

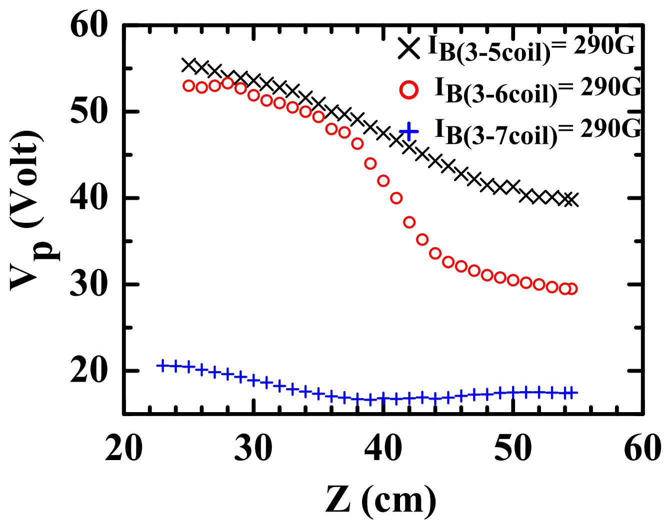

Figure 4.5: Axial plasma potential profile at 2×10^{-4}mbar, with 290G source magnetic field with three different configurations, and 200W RF power.

only at low pressure like the others have reported [4, 123]. Associated density profile is also shown in figure (4.6). Plasma potential can be calculated knowing the axial density profile by using the Boltzmann relation $V_P(z) = V_P(z_0) + T_e ln[\frac{n(z)}{n(z_0)}]$. At high pressure the calculated V_P profile (taking the experimental electron temperature profile) closely matches with the experimental uniform axial potential profile. Whereas at low pressure the experimental V_P drops much faster than the calculated Boltzmann potential values. This is the classical definition of double layer like potential structure. It is also observed in our experiment that there is a threshold magnetic field for each source dimension, above which strong or sharp fall in axial potential is observed. The ion Larmor radius (ρ_i) calculated 6.5 cm, 1.32 cm, 0.84 cm, 0.5 cm respectively for above four source magnetic fields, considering ion temperature 0.2eV [124]. Our source radius is 4.75 cm. Ions are magnetized in all three cases except the 45G source magnetic field. Therefore, for each source dimension, there is a critical source magnetic field value, above which the ions radial loss rate will be very less and axial geometrical expansion location will be the open source end. This is the most favorable condition for the formation of double layer and ion beam generation [125]. In our source dimension (radius 4.75 cm),

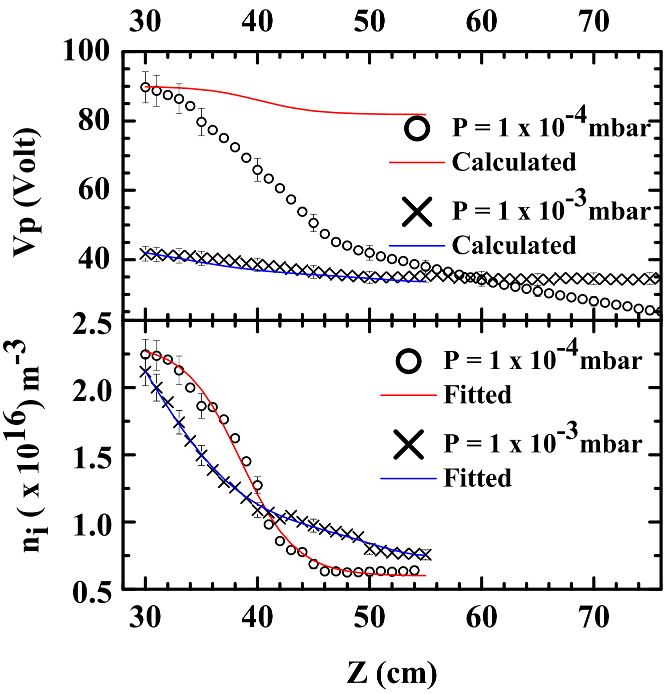

Figure 4.6: Axial plasma potential profile and density variation at high (1×10^{-3})mbar and low (1×10^{-4})mbar pressure at 100W RF power with 220G source magnetic field in 3-6 magnets configuration.

the threshold magnetic field for double layer like potential structure formation is $\sim 150G$ because ion Larmor radius ($\rho_i \sim 2cm$). When ions are magnetized in the same chamber the radial ion loss are restricted and there is only one way to loose ion from the system is along the axial direction. Experimental results in figure (4.7) show that at 45G, there is only $\sim$ 7V drop in 10 cm, when ions are unmagnetized ($\rho_i \sim 6.5cm$), But for 220G potential drop increases by $\sim$ 3 times than the 45G case. At 220G $\rho_i \sim 1.32cm$ and ions are magnetized above this magnetic field ions radial motion even more restricted, and appropriate for double layers. The axial plasma potential profiles for all the four source magnetic fields (45G, 220G, 345G and 545G) are shown in figure (4.7). It is observed that although potential gradient is present in all four cases, it is much weaker in case of low magnetic field ($45G$) compared to other three cases.

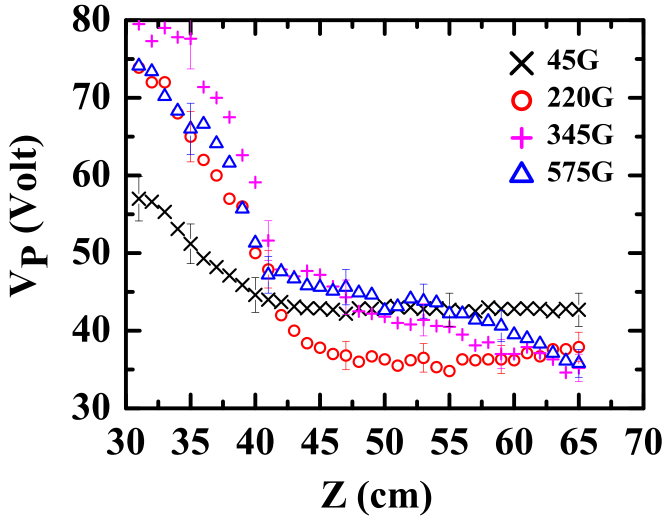

Figure 4.7: Axial plasma potential profile for different source magnetic fields in 3-6 magnets configuration at low (4×10^{-4})mbar pressure at 200W RF power

4.3 Ion beam generation

Axial potential fall at the inter-junction between source to diffusion chamber accelerate ions from the source side upstream high potential to low downstream potential and a ion beam having energy equal to the potential height is expected at the downstream. Electrons at the upstream, having energy less then the potential hill are essentially trapped. A RFEA is kept at 73 cm away from the antenna when the double layer like potential structure forms at ∼40 cm away from the antenna. RFEA raw collector signal with the discriminator bias (at 50mHz) is shown in figure (4.8). The slope change at ∼ 4.5 sec of the characteristics indicate the presence of ion beam into the system. To find out the energy of this ion beam, the same data is acquired only upto 10 sec without changing the ramp frequency to magnify the slope. The data along with the first differentiation which is the measurement of ion energy distribution function (IEDF) are shown in figure (4.9). The first peak fit at ∼37V represents the local plasma potential measurement and the second peak fit at ∼50V represents the beam potential (V_b). The energy of the ion beam is $E_b = e(V_b - V_P) = e(50 - 37)V = 13eV$. Associated plasma potential

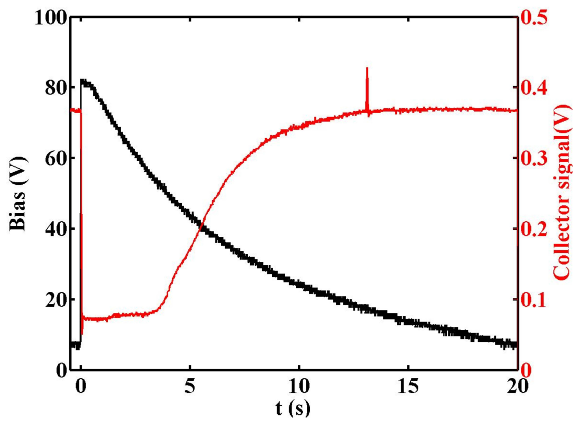

Figure 4.8: Raw RFEA signal indicating the presence of ion beam at 200W RF power at 2×10^{-4}mbar pressure with 220G source magnetic field in 3-6 magnets configuration.

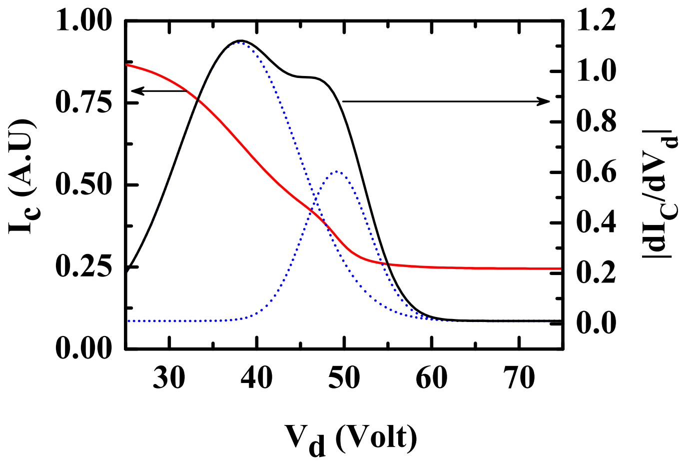

Figure 4.9: Analyzed RFEA data indicating the IEDF (Right Y-axis), first peak from left corresponds to the local plasma potential and second peak corresponds to the ion beam potential corresponding to figure (4.8).

profile corresponding to this ion beam energy is shown in figure (4.11), for zero 7^{th} magnet current ($I_{B(7)} = 0$). The local plasma potential measurement (Black data points) using emissive probe at 73 cm away from antenna is also ~35V, which is closely matches with the RFEA plasma potential measurements. The axial plasma potential profile measurement shows ~17V sharp potential drop in 4.5 cm and the

RFEA ion beam energy located ∼33 cm away from the location of double layer like potential structure, strongly evident that the ion beam is generated by this potential structure.

4.4 Transition from single to multiple axial potential structure (MAPS)

It is observed from the experimental results presented in the previous section that for the formation of double layer like potential structure, a magnetic field is required, which is strong enough to make the ions magnetized for the source. The physics of helicon plasma governs by the magnetic field line where it touches the grounded conducting expansion chamber, as there is no ground path in the source chamber. Keeping the *Close Magneto Geometric Aperture (CMGA)* configuration, application of reverse current to the 7^{th} magnet creates a cusp magnetic field structure. The last continuous field line which is coming all the way from source chamber and touches the expansion chamber at ∼75 cm in 3^{rd} to 6^{th} magnets configuration, is now touches the expansion chamber at $\sim$ 53 cm in cusp configuration shown in figure (4.10). The data presented in figure (4.11) shows there is a double layer like structure (Black data points) when there is no current passing through the 7^{th} magnet except 3^{rd} to $6^{th} = 95A$. Application of −40A current through the the 7^{th} magnet, the potential structure pushed little inside the source chamber and the strength reduces. Further increase of −20A more current, the potential falls from 67V to 50V in 10 cm and maintains uniform potential upto next $\sim$ 15 cm and then again potential drops to 38V in next 12 cm. Thus two distinct potential fall is observed with a uniform potential zone. Further increase of 7^{th} magnet reverse current the uniform potential zone disappears and the upstream potential rises. Two distinct potential structures again folded into single with increasing the cusp strength. With increasing the cusp strength electrons will loss to the wall very close to the expansion throat ($\sim$ 55) cm, hence the confinement time will be less

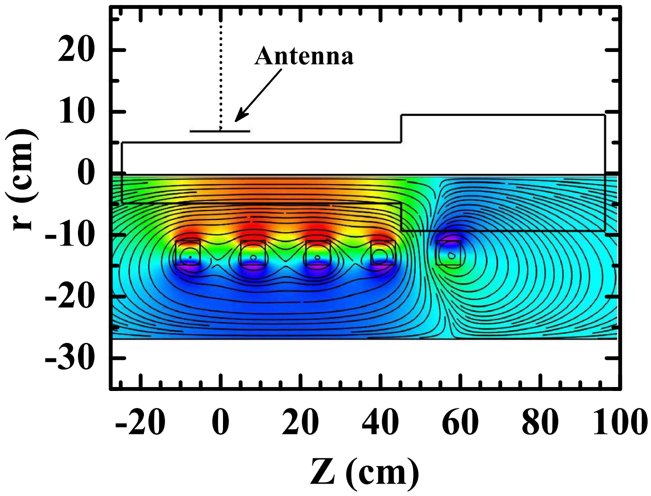

Figure 4.10: CUSP magnetic field configuration.

in that cusp configuration compared to diverging case. As the more electrons are getting lost by the wall through field line, they will leave more positive potential into the bulk plasma. Hence the plasma potential at the upstream increases and the first potential structure disappears and second one only sustains. To validate this multiple axial potential structure (MAPS), parametric space is explored to study the evolution of these structures keeping the magnet current configuration 3^{rd} to $6^{th} = 95A$ and $7^{th} = -60A$ same.

4.4.1 Parametric study

With decreasing fill pressure from 2×10^{-4} mbar to 1×10^{-4} mbar, both the structures are found to more stronger than increasing fill pressure from 2×10^{-4} mbar to 4×10^{-4} mbar, which is shown in figure (4.12). This results are very much similar to the results obtained for single double layer as it is discussed in previous section. With increasing radio-frequency power both the structures are found to be more stronger than decreasing power as shown in figure (4.13). With increasing power probably the threshold density requirement condition (which will be discussed in the discussion section) is meeting the condition well for producing stronger double layer. Experiments are carried out to study the effect of multiple

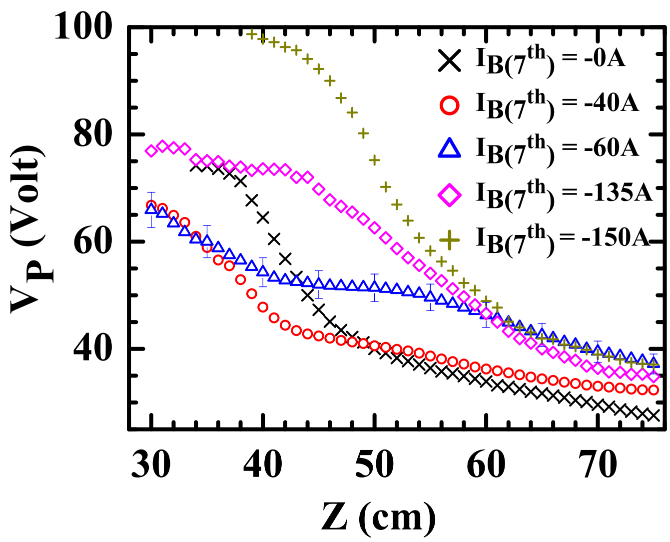

Figure 4.11: 200W, 3-6 magnets 220G source, (-)Ve current in 7^{th} magnet at 2×10^{-4} mbar, Transition from single to multiple axial potential structure (MAPS) by creation of cusp magnetic field profile.

axial potential structures formation with the magnetic field gradient. Keeping the current ratio $[\frac{I_{B(3-6)}}{I_{B(7)}} = 1.53]$ (figure 4.14), with decreasing the gradient strength both the structures are found to more stronger than increasing gradient as shown in figure (4.15). At higher ∇B_Z again due to similar reason of electron lossy channel or lower confinement, plasma potential at the upstream raised up and the second structure is become dominant over the first.

4.4.2 Validation of MAPS

Simultaneous measurement of axial density and temperature distributions are also taken in presence of multiple axial potential structure (figure 4.16). It is observed that there exist non-uniform density distributions and the upstream density rise consistent with the higher potential of each double layer like structure. Associated electron temperature profile shows a peak profile at a location ($\sim 35cm$) where the density has a trough. The similar observation is also noticed in another gradient ($\nabla B_z \sim -6.16$)G/cm configuration (figure 4.17). In both the gradient experiment application of the Boltzmann equation incorporating the axial temperature

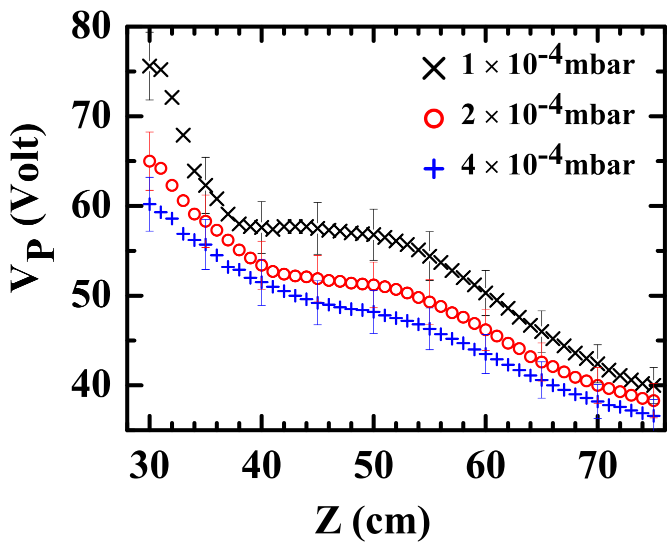

Figure 4.12: Evolution of MAPS with fill pressure at 200W with $I_{B(3-6)}$= 95A and $I_{B(7)}$= -60A.

variation, solve the complete integral equation (4.1)

$$V_P(Z) = \int_{z_0}^{z} T_e(z) \frac{\partial(\ln(n_i))}{\partial z} dz \tag{4.1}$$

to find out the axial plasma potential. The experimental plasma potential profile shows more drops than the calculated (red curve) plasma potential profile, resembling the existence of the additional potential structure together with the relatively stronger potential structure. Details about this density and electron temperature distribution will be discussed in chapter 5.

4.5 Discussion

Experimental results (figure 4.3, 4.4 and 4.5) established that the double layer like potential structure is only be observed when the magnetic expansion closely coincide with the geometrical expansion, which is different from the experimental result reported by Sutherland et al. [116]. In their experiment, their magnet system is mounted on a movable tray. When this tray is moved from diffusion chamber

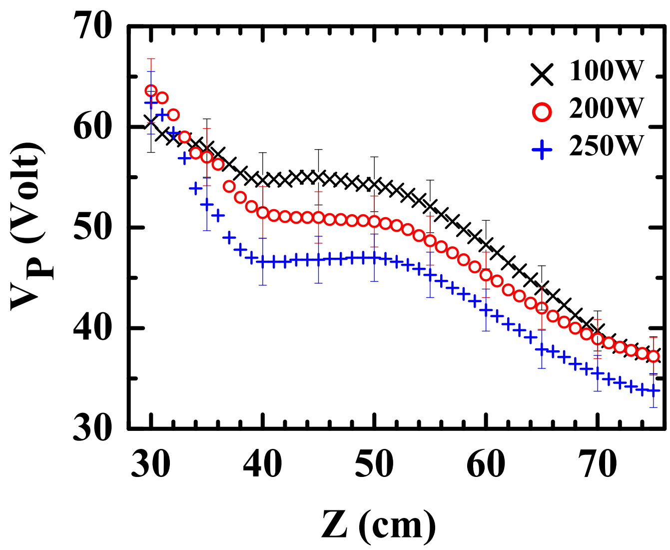

Figure 4.13: Evolution of MAPS with RF power with $I_{B(3-6)}$= 95A and $I_{B(7)}$= -60A at 2×10^{-4}mbar.

toward the source chamber or the location of maximum magnetic field divergence then the location of double layer is also shifted inside the source chamber. In their case formation of double layer is independent of the geometrical expansion. Numerical simulation also suggested that the formation of current free double layer is predominantly controlled by the increased ion loss in the diverging magnetic field region [120]. However, our experimental result shows that the formation of double layer is a cumulative effect of the both geometric and magnetic expansion. Our results are consistent with the experimental results obtained in VINETA [117]. In that experiment, they have changed both the location of geometry and maximum of magnetic field gradient and found that the stronger double layer like structure is observed only when both these two expansion closely coincide with each other.

Plasma expansion may be associated with complex transport phenomena including double layer like potential structure formation and instabilities. In this kind of systems, ionization dominates mainly in the source chamber and geometrical expansion leads to a gradient in the plasma density, decreasing from source to the expansion chamber. In these expanding plasmas, generally the electrons closely obey the Boltzmann equilibrium and the gradient of density is accompanied by a

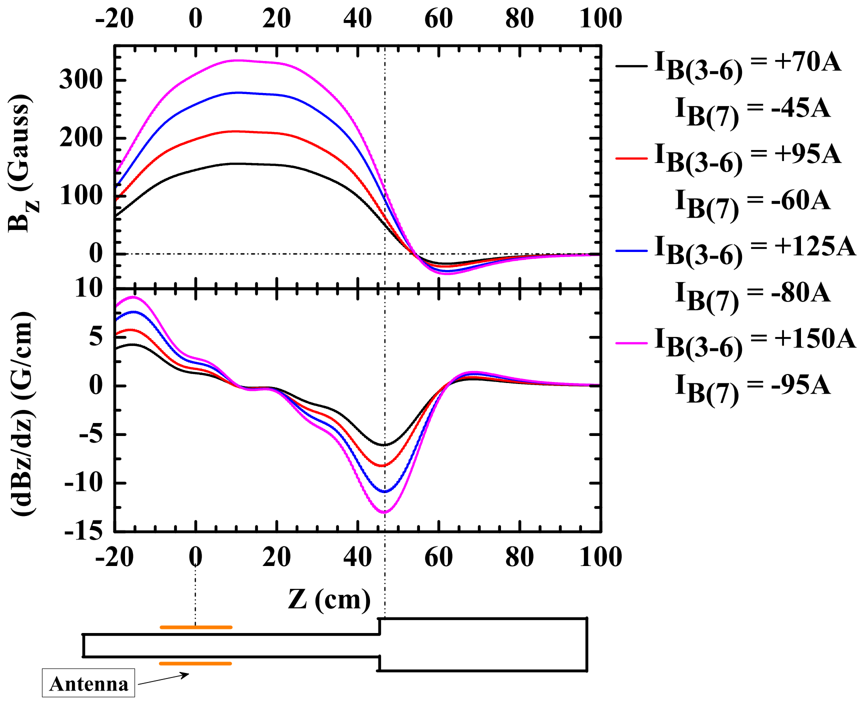

Figure 4.14: MAPS simulated gradient strength, keeping $\frac{I_{B(3-6)}}{I_{B(7)}} = 1.53$ constant.

very weak gradient in DC plasma potential. Consequently, a very weak electric field accelerates positive ions out of the source. In general the plasma remains quasi-neutral during the expansion and the ion acceleration remains insignificant in this case. Adding strong magnetic divergence together with the geometrical expansion leads to enhancement of ion acceleration and generation of supersonic ions. Plasma permittivity is given as [89] equation (4.2)

$$\epsilon_p = \epsilon_0 k_p = \epsilon_0 \{1 - \frac{\omega_{pe}^2}{\omega(\omega - i\nu_m)}\} \tag{4.2}$$

For $\omega >> \nu_m$ and $\omega_{pe}^2 >> \omega^2$ the above equation reduced to

$$\epsilon_p = \epsilon_0 \frac{\omega_{pe}^2}{\omega^2} \tag{4.3}$$

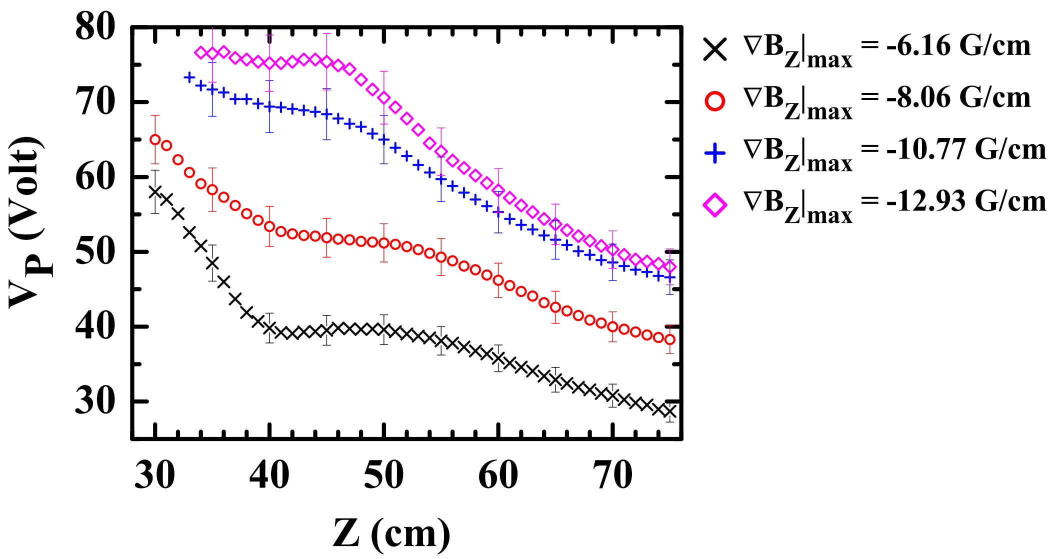

Figure 4.15: Evolution of MAPS with magnetic field gradient strength at 200W with $I_{B(3-6)}$= 95A and $I_{B(7)}$= -60A at 2×10^{-4}mbar.

Electric field in plasma is defined as [89]

$$E_{plasma} = \frac{J_T}{i\omega\epsilon_p} \tag{4.4}$$

Where J_T is the total current density. Taking $J_T = nev_d$ the modified electric field becomes

$$E_{plasma} = \frac{m_e\omega}{ie}v_d \tag{4.5}$$

Which indicates that the electric field is directly proportional to the drift velocity. Usually divergence or gradient increase the velocity components. Presence of magnetic and geometric divergence together with raise this velocity component effectively [$v_d = \sqrt{\frac{2e}{M}(V_{up} - V_{down})}$], where V_{up} and V_{down} respectively are the upstream and downstream of double layer potentials. As a result this potential difference $(V_{up} - V_{down})$ is also increase. Therefore, this configuration is better suited for producing stronger potential structure.

A critical upstream density is required for maintaining the double layer potential structure [31]. Multiple double layers have been observed at high pressure glow

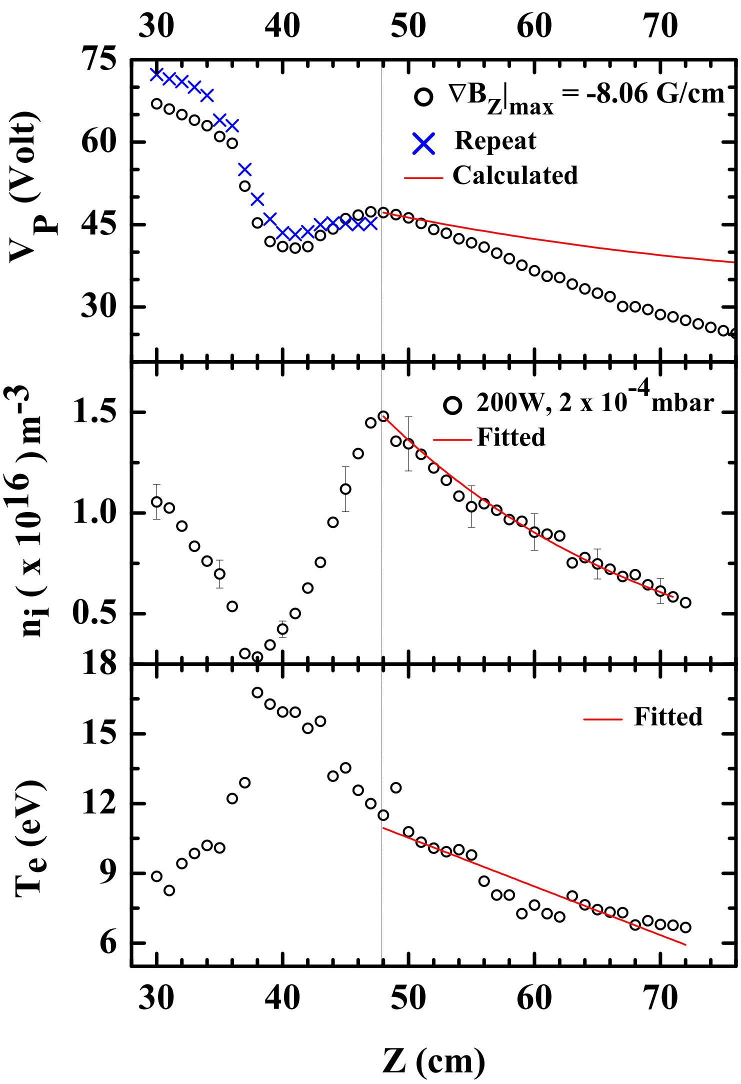

Figure 4.16: Axial plasma potential, density and electron temperature variation at 200W RF power, $I_{B(3-6)}$= 95A and $I_{B(7)}$= -60A, 2×10^{-4}mbar.

discharge plasma, where the energetic electron overcome the first potential step, are getting sufficient ionization length to make the ionizing collision to maintain this critical density above the critical limit for the formation of another double layer adjacent to the first potential step. In our case those energetic electrons overcoming the first potential hill, will not get sufficient ionization length for making ionization to its adjacent. As the ionization length for our low pressure $\sim 10^{-4}$mbar

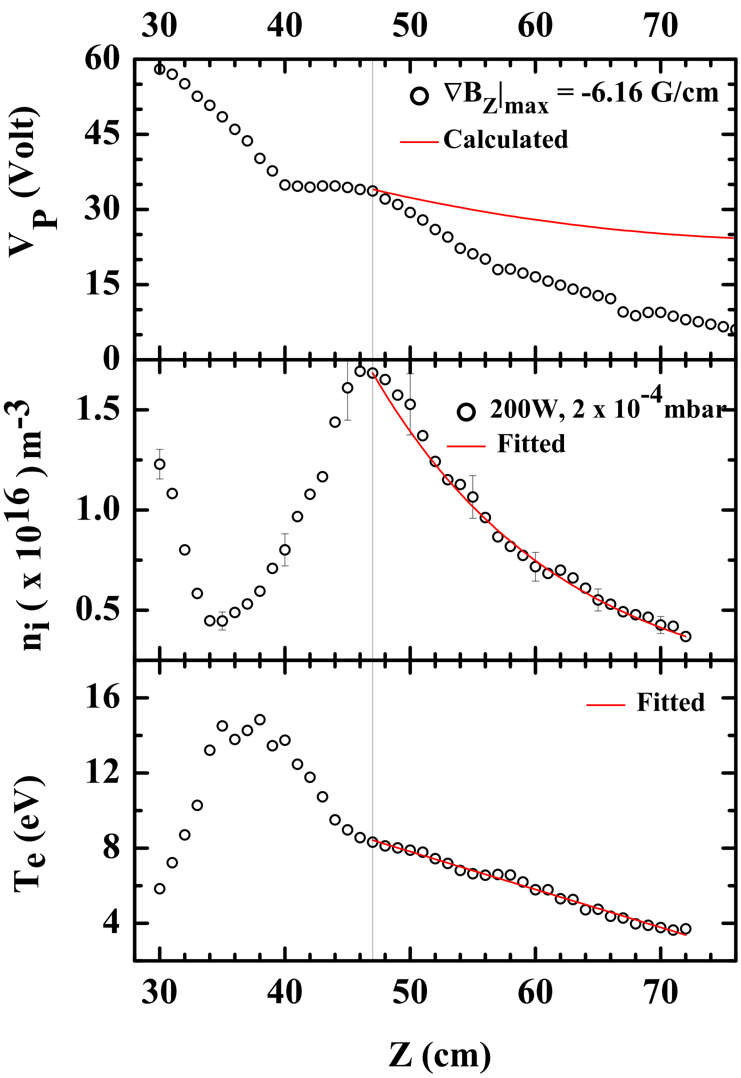

Figure 4.17: Axial plasma potential, density and electron temperature variation at 200W RF power, $I_{B(3-6)}$= 75A and $I_{B(7)}$= -40A, 2×10^{-4}mbar.

plasma is $\sim$ 10 meters. In this experiment, electrons are heated up away from the antenna center. Since electrons are heated up locally they try to escape the volume they are being heated due to increase of kinetic energy. A local density trough is created at that location. Therefore, the axial density distribution is now become non-uniform. Generation of cusp like magnetic field configuration controls the rise of downstream density (which may be consider another upstream for the second potential structure) to form the second potential structure. Theory of double layer is far from complete. Double layer solutions are belong to the class of BGK solutions of the Vlasov-Poisson equation [118], however the actual physics governing the double layer can not yet revealed from such solutions. Potkalitsky et al. [126] suggested the use of a boundary layer theory to describe the double layers in a long system. Chung and Noah [28] experimentally demonstrated that the boundary conditions can determine the characteristics of the double layer. Many analytical treatment on double layer, assume infinite plasma, while numerical simulation consider small system ($L \leq 100\lambda_D$) [6]. However, long system ($L >> 100\lambda_D$) can produce multiple double layers. For example, striations, which is a series of double layers, commonly observed in glow discharge plasma [127] as it is discussed before. Chung and Noah [28] showed that the number of double layers for a given set of boundary condition depends on the parameter $\epsilon = (\frac{\lambda_D}{L})^2$. They have experimentally shown that multiple double layer can be formed in a specified boundary if the parameter $\epsilon \sim 1\times10^{-5}$. Our system size $\sim$ 1.2m and $\lambda_D \sim$ 0.2mm, which if far bellow than this critical limit. Therefore, boundary condition and and our working parameter range fall well inside the formation of the multiple axial potential structures. Peter and Noah [31] showed a necessary condition that stable double layers found in laboratory experiments must exist for upstream densities greater than a critical value (n_c), which determine by the trapped electron density by the double layer. Our experimental density profile in presence of MAPS shows density humps corresponding to each potential hills (figure 4.16 and 4.17). These results are in agreement with the critical density requirement for the formation of stable double layer.

4.6 Summary

Spontaneous formation of electrostatic potential structures in geometric and magnetic expanding plasma has been observed. In quasi-neutral plasma it does not support to have significant electric field, however violation of plasma quasi-neutrality can create local potential gradient and consequently a strong electric field, which is strong compare to ambipolar fields. This layer of non-neutral regime separates two quasi-neutral plasmas called the double layer like potential structures. Current-free double layer like potential structures have been observed in expanding helicon plasma systems when both geometric and maximum of magnetic field gradient closely coincide with each other. Generation of cusp like magnetic field configuration after the throat helps to generate MAPS like potential structure. Associated ion beam generation, having energy nearly equal to the potential drops corresponding to first strong structure confirms the existence of the structure. Second weak structure is found to be much sharper than the predicted Boltzmann potential drop, confirms the existence of the second structure. The density profile maintains in such way in the system that it gives two unidirectional axial gradients, which corresponds to two distinct potential structures keeping a uniform potential zone in between, hence summing up the thrust along the axial direction.

5

Localized electron heating

5.1 Introduction

As discussed in the previous chapter that the critical downstream density peak is responsible for the formation of multiple axial potential structures (MAPS), in this chapter a through investigation has been carried out to find out the source of local electron heating and ionization. In 1995 Chen et al. [128, 129] showed electron temperature (T_e) peaked near the antenna and the density rise at $\sim$ 40 cm away from the helical antenna with $\sim$ 800G uniform axial magnetic field in their system. They commented that the electron temperature (T_e) peaking is located within one wavelength from the antenna, where electrons are apparently heated by the near field of the antenna [129]. Recently, Siddiqui et al. have observed the electron temperature peaking 10cm away from the end of helical antenna [88]. However, they did not observe any density peak through out the axis of their radially uniform cylindrical system, without any expansion chamber. They reproduced [130] the peak electron temperature location closer to the antenna as observed by chen et al. [129] by moving the grounded end plate further away from the antenna. Tysk et al. too have reported the downstream density rise without any explanation[53]. Therefore both these phenomena, localized electron heating and downstream density rise at different distances from the antenna warrant further experimentation and analysis for resolving the root cause behind these phenomena in helicon plasma.

We report electron temperature (T_e) peaking far away from the antenna (~ 35 to 45 cm) along with the rise in density further downstream where the temperature decreases. Presence of helicon wave has been identified even at low densities ($\sim 10^{16} m^{-3}$). Axial wave field measurement shows a damped helicon wave like structure. Landau damping heating mechanism is found to be highly consistent with our experimental observations. A density trough is created at the location of the electron heating. Further downstream, density peak is observed $\sim 55 - 65$ cm away from the antenna. Qualitative discussion on this downstream density peaking is carried out using the proposed pressure balance equation. The experiments are repeated with several source magnetic field strength and the location of magnetic field divergence both in presence and absence of strong axial plasma potential (V_P) gradients, known as "double layer like structures" [88].

The rest of this chapter is organized as follows: In section 5.2 and 5.3 experimental results of localized electron heating and downstream density rise are presented. In section 5.4 existence of helicon wave is reported at low magnetic field. In section 5.5 helicon wave particle interaction is discussed with measuring the wave phase velocity and electron ionization velocity. The mechanisms for electron heating is discussed and downstream density rise is modeled using pressure and energy balance followed by a summery of this chapter.

5.2 Observation of localized electron heating

In the first set of experiments current of 21 A is applied to four magnets (magnet 3 to 6) producing a magnetic field of ~ 45 G on axis at low 4×10^{-4}mbar Argon fill pressure. This configuration of magnets produce B-field gradient at $Z = 46$ cm (figure (5.1c)). The axial variation of density, electron temperature and plasma potential in this parameter regime are plotted in figure (5.1a, b) and (5.2) respec-

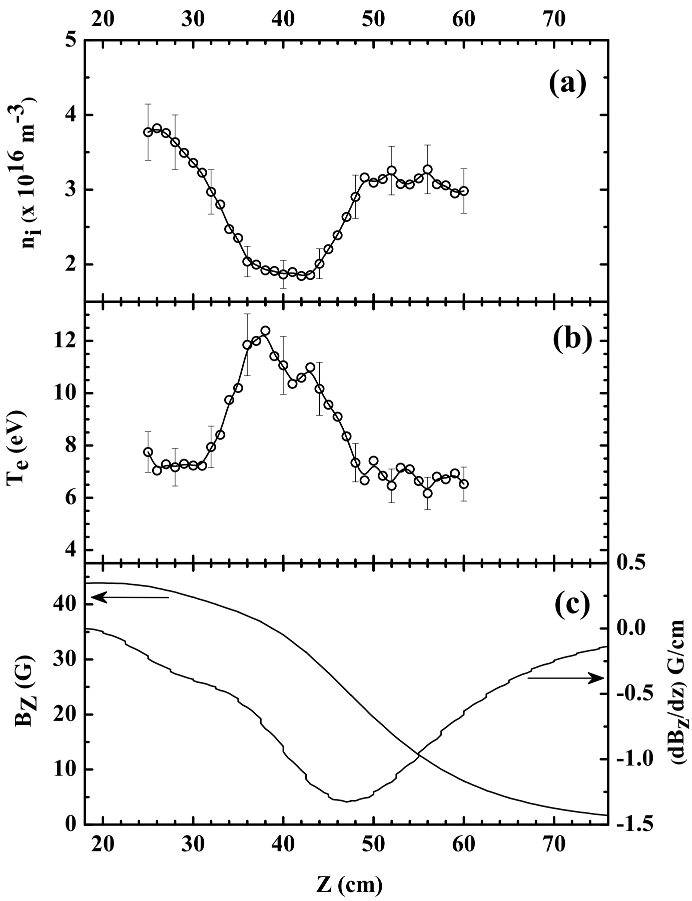

Figure 5.1: Axial variation of (a) density, (b) electron temperature and (c) magnetic field and its gradient in 4 magnets (3rd to 6th) configuration. Pressure: 4×10^{-4}mbar, RF power: 200W. Antenna located at $Z = 0$ cm, geometrical expansion is at $Z = 45$ cm.

tively. Figure (5.1) clearly shows that axial profile of electron temperature with peak electron temperature $\sim$ 12.5 eV occurring at $Z \sim$ 35cm. The temperature decreases to $\sim$ 6eV, i.e. a factor of approximately two of the peak value at $Z \sim 50$ cm.

In another set of experiments, where Argon fill pressure is increased by an order, did not show any variation in the location of maximum electron temperature along the axis (figure (5.3)). The parameters varied are the magnitude of the axial magnetic field and the location of the magnetic field gradient in the expansion chamber. To change the gradient location, different numbers of electromagnets,

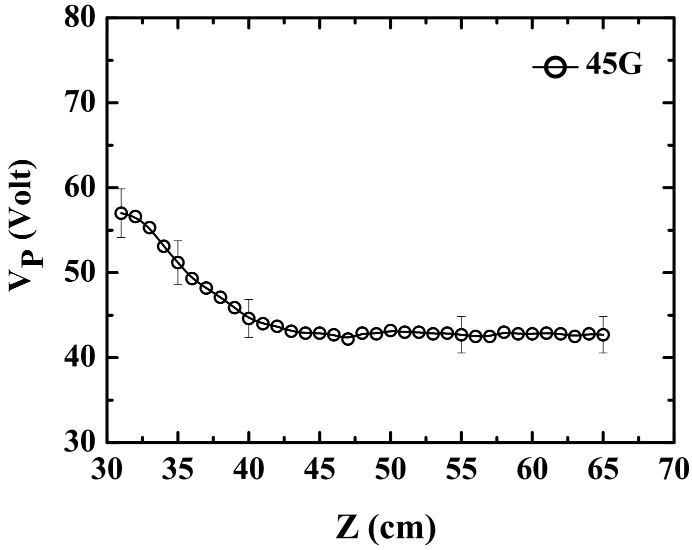

Figure 5.2: Axial variation of plasma potential with similar experimental condition as in figure 5.1.

e.g. 4 magnets (magnet 3 to 6) or 5 magnets (magnet 3 to 7) or 6 magnets (magnet 3 to 8) are energized. Source magnetic field is varied by energizing magnets with different currents. For example, 21 A, 95 A, 150 A and 250 A current in the magnets, produces magnetic field of $\sim$ 45 G, $\sim$ 220 G, $\sim$ 345 G and $\sim$ 575 G respectively. However, interestingly the heating location did vary with changing the gradient location of axial B-field as shown in figure (5.4). To move the magnetic field gradient location further away from the antenna at $Z = 76$ cm, 6 magnets (magnet 3 to 8) are used as shown in figure (5.4c). Similar behavior in axial variations of electron temperature and density (figure (5.4a, b)) has been observed. However, the location of the electron temperature peak of $\sim$ 12 eV moved further downstream at $\sim$ 50 cm compared to earlier case when the magnetic field gradient stay closer to the antenna at $Z \sim 46$ cm (figure 5.1). The temperature finally decreases to $\sim$ 5.5 eV at $Z \sim 65$ cm. Similar to the movement of electron temperature peak position, the peak location of the downstream density rise also moves further downstream occurring at $Z \sim 65$ cm. In figure (5.1), the T_e peak occurs at the location of the magnetic field gradient, and in figure (5.4) it occurs well

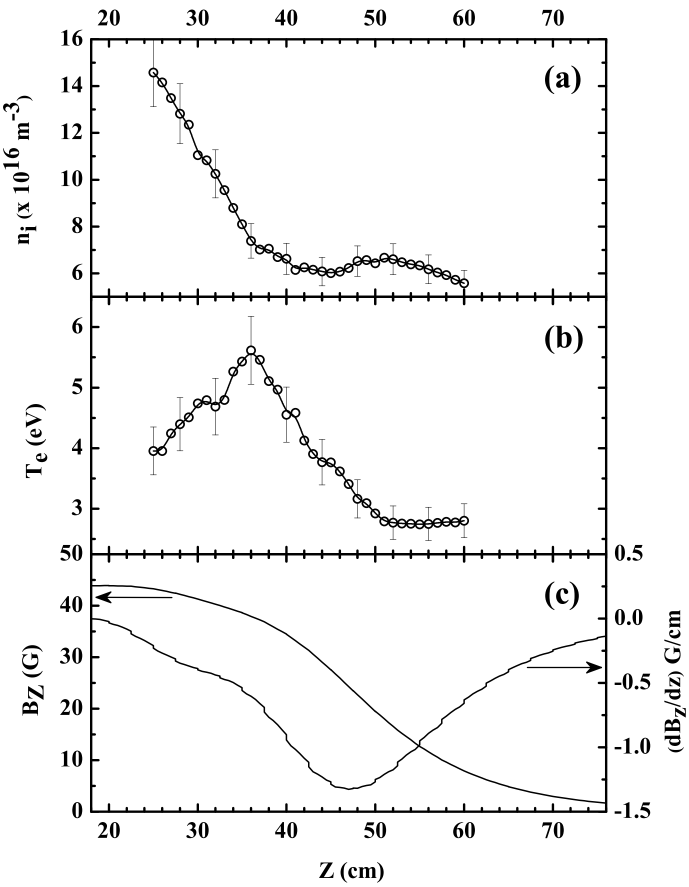

Figure 5.3: Axial variation of (a) density, (b) electron temperature and (c) magnetic field and its gradient in 4 magnets (3rd to 6th) configuration. Pressure: 4×10^{-3}mbar, RF power: 200W. Antenna located at $Z = 0$ cm, geometrical expansion is at $Z = 45$ cm.

before the gradient. In figure (5.1), the location of magnetic divergence coincides with that of geometrical expansion whereas in figure (5.4), the location of magnetic divergence is placed far away from the geometrical expansion. The location of geometrical expansion may plays more dominant role of T_e peaking compared to the magnetic divergence. Plasma potential (V_p) measurement figure (5.5) corresponding to the condition of figure (5.4) shows there is no such significant axial electric fields. Which also confirms that T_e peaking can be taken place even when there is no axial electric fields.

The observation of location of maximum electron temperature quite away from

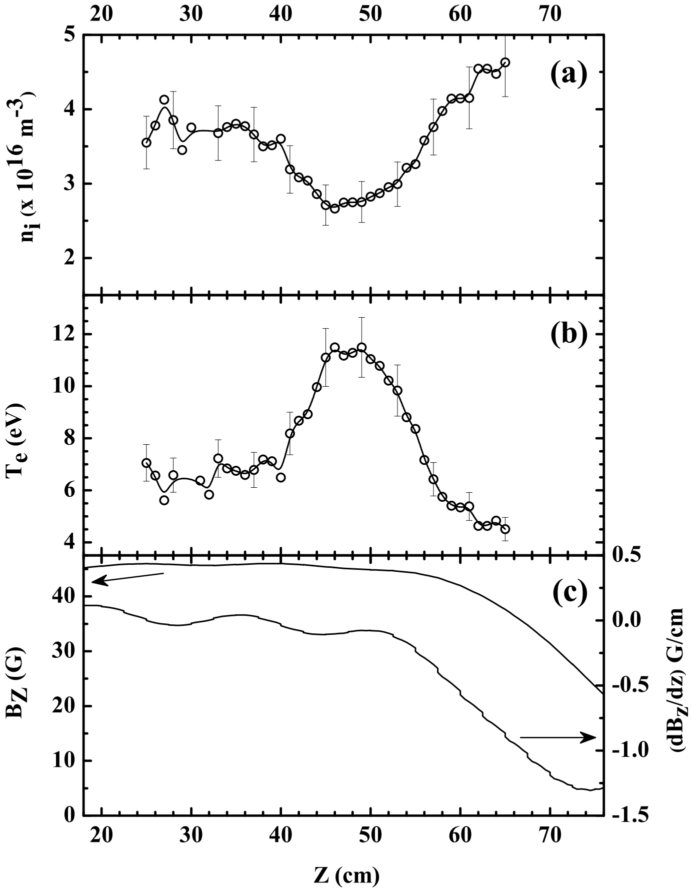

Figure 5.4: Axial variation of (a) density, (b) electron temperature and (c) magnetic field and its gradient in 6 magnets (3^{rd} to 8^{th}) configuration. Pressure: 4×10^{-4}mbar, RF power: 200W. Antenna located at $Z = 0$ cm, geometrical expansion is at $Z = 45$ cm.

the antenna and its movement further away from the antenna with changing the position of magnetic field gradient indicates that the near field effects of the antenna cannot be held responsible for the temperature peaking as it is happening far away from the helical antenna.

5.3 Observation of downstream density rise

The axial density profile shows (figure 5.1) that the density decays from its initial value of $3.8 \times 10^{16}\ m^{-3}$ at $Z \sim 25$ cm near the antenna to $1.8 \times 10^{16}\ m^{-3}$ at $Z \sim 35$

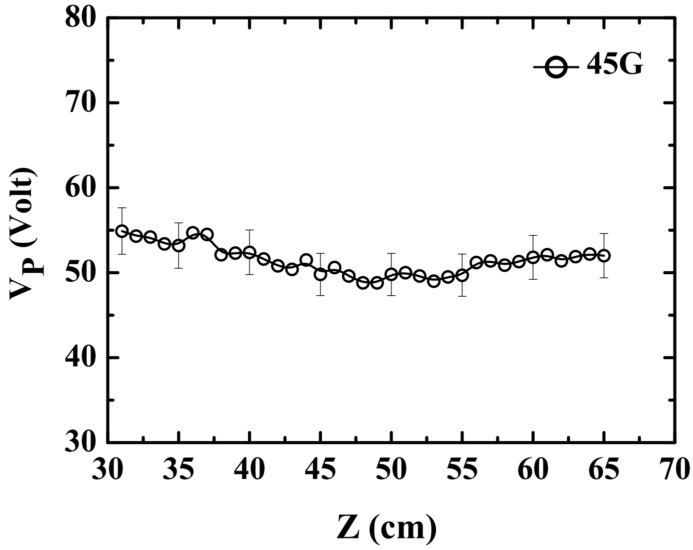

Figure 5.5: Axial variation of plasma potential with similar experimental condition as in figure 5.4.

cm before increasing again to 3×10^{16} m^{-3}, i.e. by a factor of approximately 1.5 of its minimum value. Plasma potential (V_P) measurement (figure 5.2) shows the existence of an electric field at location $Z = 30$ to 40 cm. In totality, it has been observed that at an axial distance $Z \sim 35$ cm, the electron temperature peaks while the density hits its minimum, at that location followed by a density rise and temperature minimum further downstream at $Z \sim 55$ cm. Moreover, a systematic trend has been observed between the magnitude of the potential gradient and the ratio of incremental reduction of temperature ($\frac{\delta T_e}{Te}$) to the incremental rise of downstream density ($\frac{\delta n}{n}$). In presence of weak potential gradient (and hence the weak axial electric field) as in case of 45 G, the percentage change (decrease) in the electron temperature from its peak value is almost equal to the percentage change (increase) in the density from its minimum value. As the potential gradient increases the ratio of incremental reduction of temperature to the incremental rise of downstream density becomes less than unity, i.e. percentage fall in temperature is much more than the percentage increase in density.

5.4 Existence of helicon wave at low magnetic field

The measurements of radial profile of axial wave magnetic component (b_z) demonstrated the presence of helicon waves in both low as well as high source magnetic field cases. This is shown in figure (5.6), where the radial (b_z) profile clearly indicating the presence of $m = +1$ helicon wave mode (figure (5.6)). Helicon-TG wave dispersion plot for 45 G magnetic field also at source density of 3.5×10^{16} m^{-3}, shown in figure (5.7). To investigate further the causes of this axial peaking of electron temperature, we measured the wave magnetic fields using high frequency B-dot probes. To increase the sensitivity of the measurements, the magnetic field has been increased up to 575 G in two steps of 220 G and 345 G.

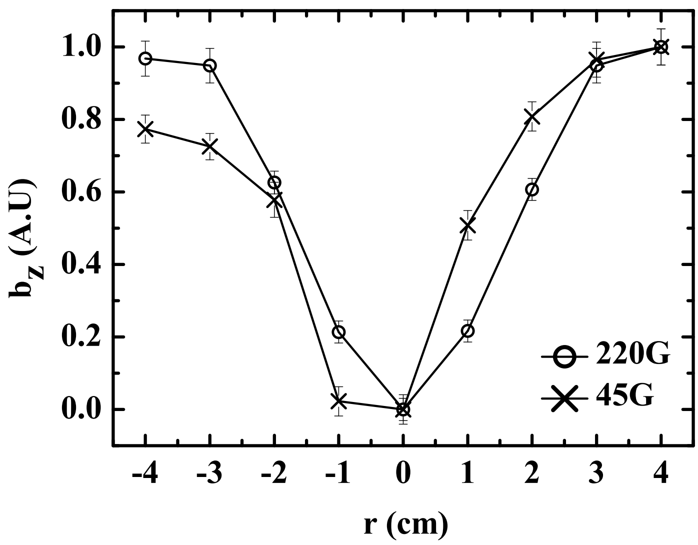

Figure 5.6: Radial variation of axial component of wave magnetic field at 3 to 6 magnets configuration.Pressure: 4×10^{-4}mbar, RF power: 200W.

Axial profile measurements of density, temperature and plasma potential have been repeated with increased magnetic field strengths, keeping the maximum of axial magnetic field gradient at $Z \sim 46$ cm. Figure (5.8a, b) shows the axial temperature and density measurements with different magnetic field strengths. As shown in the figure (5.8a, b), the axial variation of both T_e and density remained similar trend as observed in low magnetic field of ~ 45 G as discussed earlier

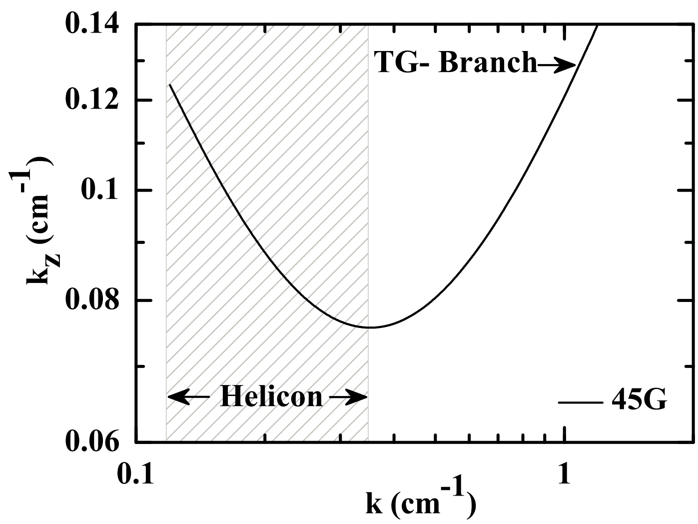

Figure 5.7: Helicon - TG dispersion plot at 13.56MHz.

(figure (5.1)). Although no such noticeable variation in location of maximum temperature and density in the downstream plasma is observed, the magnitude of downstream density rise gradually decreases as the magnetic field is increased. However, the strength of potential structure increases significantly as shown in figure (5.9) compared to the case as shown in figure (5.2).

As mentioned earlier, the density and temperature are measured using RF compensated Langmuir probes. Although Langmuir probes are easier to design, the proper interpretation of its $I-V$ characteristics is quite complex and difficult, especially in the presence of complicating factors such as magnetic fields, RF fluctuations of varying strength, hot and cold electrons, beam and secondary emission effects. Figures (5.10a) and (5.11a) show the $I-V$ characteristic traces of RF compensated Langmuir probes at 220 G and 345 G respectively. The ion saturation part of the $I-V$ characteristics is magnified and presented in the insets of figures (5.10a) and (5.11a). After proper subtraction of ion current from the total probe current, the semilogarithmic plots of electron current versus probe bias voltage are shown in figure (5.10b) and (5.11b) for two magnetic field strengths. It is quite well known that the electron temperature is determined from the slope of the linear regime and presence of different slope indicates the presence of different

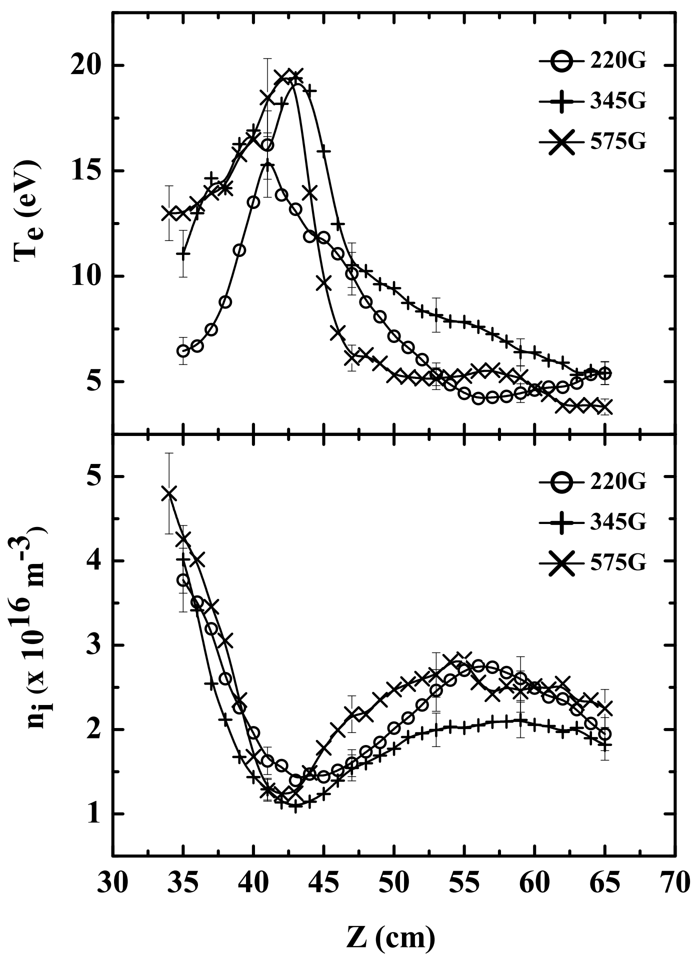

Figure 5.8: Axial variation of (a) electron temperature, (a) density for three different source magnetic field at 4 magnets (3^{rd} to 6^{th}) configuration. Pressure: 4×10^{-4}mbar, RF power: 200W. Antenna located at $Z = 0$ cm, geometrical expansion is at $Z = 45$ cm.

electron temperature components. Figures (5.10b) and (5.11b) show mainly the presence of single component and there seems to be insignificant contribution of second component or non-thermals in the measurements. This is also confirmed from the non-observance of any distinct slope, [131] in dominant ion current region of the I-V characteristics shown in the insets of figure (5.10a) and (5.11a).

As mentioned earlier, the electron temperature peaking in the downstream region far from the antenna cannot be due to near field effect of the antenna and to investigate the processes governing local heating far from the antenna, wave field

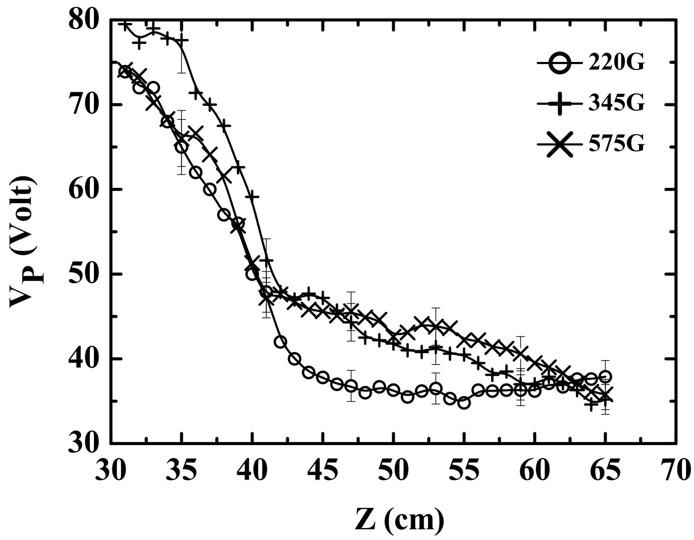

Figure 5.9: Axial variation of plasma potential with similar experimental condition as in figure 5.8. Antenna located at $Z = 0$ cm, geometrical expansion is at $Z = 45$ cm.

measurements of helicon wave are carried out using high frequency B-dot probes.

5.5 Helicon wave particle interaction

Helicon wave field amplitude and phase measurements have been carried out for all the three different source magnetic fields, which are shown in figure (5.12) (5.13) and (5.14). It is observed that the amplitude of the propagated helicon wave decays nearly after first wave length. The wavelength of the helicon wave has been deduced from the measured phase variation ($\lambda_{\parallel} = \frac{360}{(d\phi/dz)}$). The wave lengths are found to be nearly same $\sim 36 - 38$ cm in all three high source magnetic fields. Phase velocity of the helicon wave is easily calculated by multiplying wavelength with the RF frequency $v_p = \lambda_{\parallel} f_{rf} = 4.8 \times 10^6$ m/s, which is very close to the electron impact ionization velocity [42]. This strongly suggest Landau damping wave particle interaction plays an important role for electron heating and density production in our low density helicon plasma.

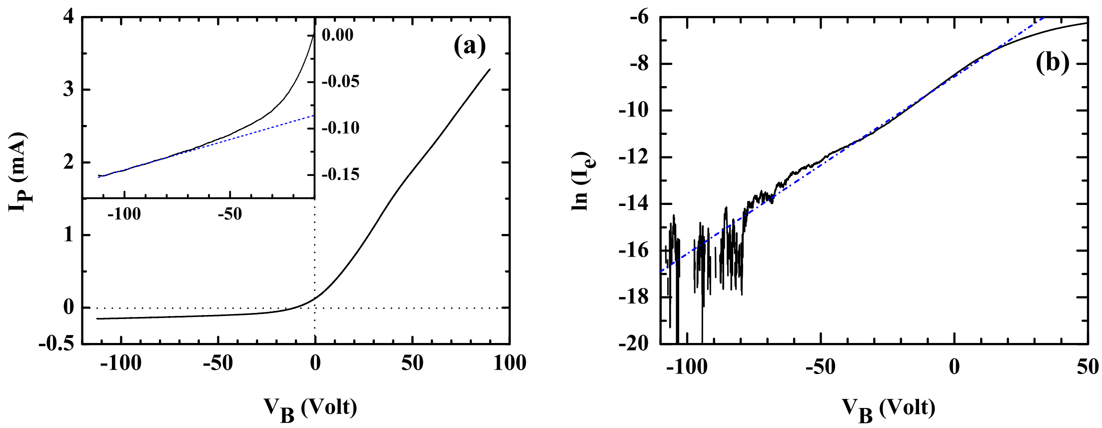

Figure 5.10: (a) RF compensated single Langmuir probe characteristics at $Z = 40$ cm corresponding to figure 5.8, at 220G source magnetic field, the magnified ion current with straight line fit for subtraction of ion current contribution from the whole $I - V$ trace to obtain electron current, is shown in the inset. (b) $ln(I_e)$ with bias voltage, electron temperature $T_e = 14.28eV$.

5.5.1 Electron heating mechanism

In-spite of several rigorous theories and experiment, the high efficiency of helicon wave absorption is still not fully understood. Several mechanisms have been proposed for heating and power deposition in a helicon antenna produced plasmas. Such as, collisional absorption [40], TG mode absorption [44, 59, 60] resonant electron interaction with RF field [106, 132–134], parametric decay instabilities [61, 70, 135], wave trapped electrons [42, 55] and Landau damping in low density [40, 56]. However, no single mechanism is able to describe heating and power deposition in all regimes of helicon plasmas and different mechanisms are required in different plasma parameters.

For example, collisional damping mechanism [40] describe well the phenomena of heating and power deposition at very high density, but at low pressure, it is not applicable as collisional damping is insignificant. Role of TG mode in helicon wave absorption was explained by Shamrai [44]. This mechanism is dominant at low magnetic field and power mostly deposited at the plasma boundary. Since the localized heating is observed with both low and high magnetic field strengths in our

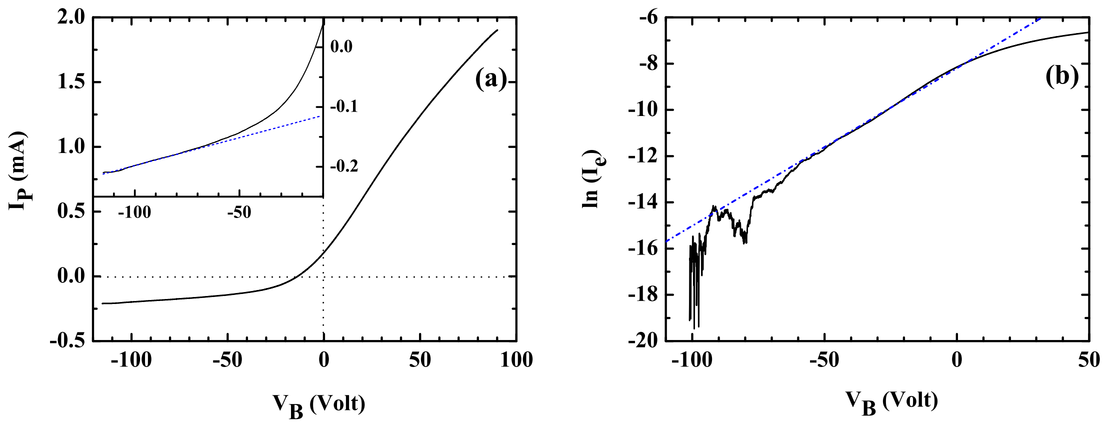

Figure 5.11: (a) RF compensated single Langmuir probe characteristics at $Z = 40$ cm corresponding to figure 5.8, at 345G source magnetic field, the magnified ion current with straight line fit for subtraction of ion current contribution from the whole $I - V$ trace to obtain electron current, is shown in the inset. (b) $ln(I_e)$ with bias voltage, electron temperature $T_e = 16.6eV$.

experiment, TG wave damping mechanism is unlikely to describe our experimental result. Resonant electron interaction with RF field is an established mechanism in collision less inductively coupled plasmas which leads to electron heating. The RF electric field stochastically transfer energy to the electrons before they cross the skin layer δ [106, 132], i.e. during the transit time of the electrons in the skin layer. The resonance condition for power absorption is $\omega = \omega_{res} = \frac{v_{th}}{\delta}$, where $\delta(= \frac{c}{\omega_{pe}})$ skin depth and ω_{pe} is the electron plasma frequency, c is the speed of light and v_{th} is the electron thermal speed. Local density and electron temperature decides the necessary condition for this resonance. Again, in our experiment, although the resonance condition is satisfied at low pressure, however they are not at high pressure. Therefore, this possibility can also be ruled out as well. It is also well known that absorption of helicon wave can arise from parametric decay instability, leading to generation of ion acoustic turbulence, which in turn can heat electrons and/or ions. This happens at relatively high magnetic field (more than few hundred Gauss) where lower hybrid frequency approaches pump wave frequency ($\sim 13.56MHz$). In case of low magnetic field ($20 - 40G$), parametric decay instability can grow, when the helicon wave is propagating near the resonance

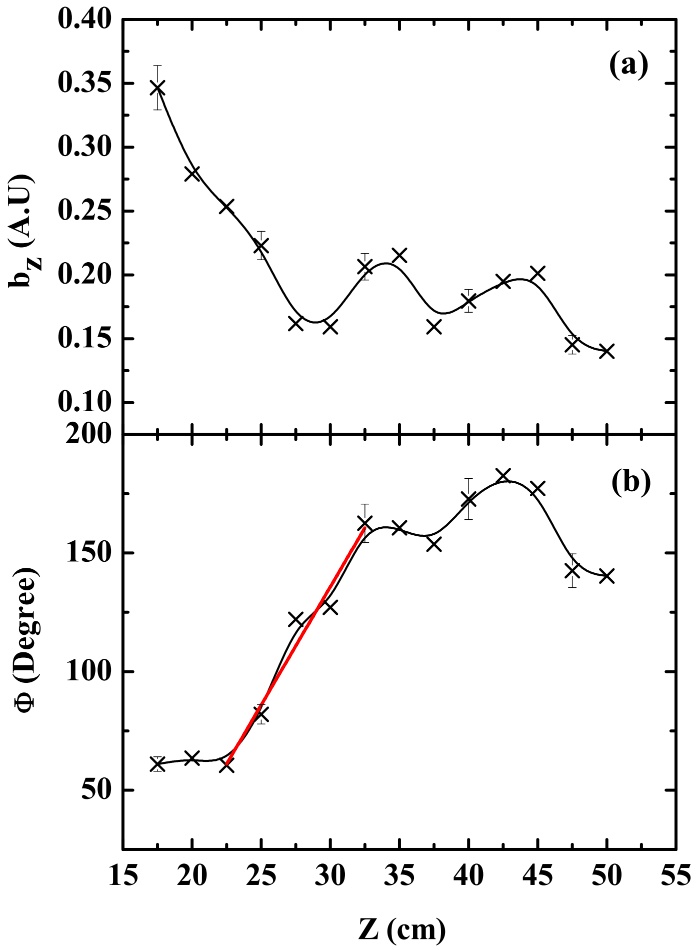

Figure 5.12: (a) Axial component of wave amplitude variation wave field and (b) is its phase at 4×10^{-4}mbar, 200W with 220G magnetic field in 3 to 6 magnet configuration, $\lambda_{\|} = 36$cm

cone as reported by Arnush [136], Bosewell [137, 138] and Barada [139]. Akhiezer et al. [61] have shown that during electron heating due to parametric instability, T_e attains a maximum value at a certain distance ~ 15 cm from the antenna. In our experiment, it is observed (figure 5.1 and figure 5.4) that the peak temperature location changes from 35 cm to 45 cm by shifting magnetic field gradient keeping everything in the source region same. This suggests that parametric instability may not be the main driving mechanism, however studies of parametric decay instability is causing localized electron heating is needed further investigation.

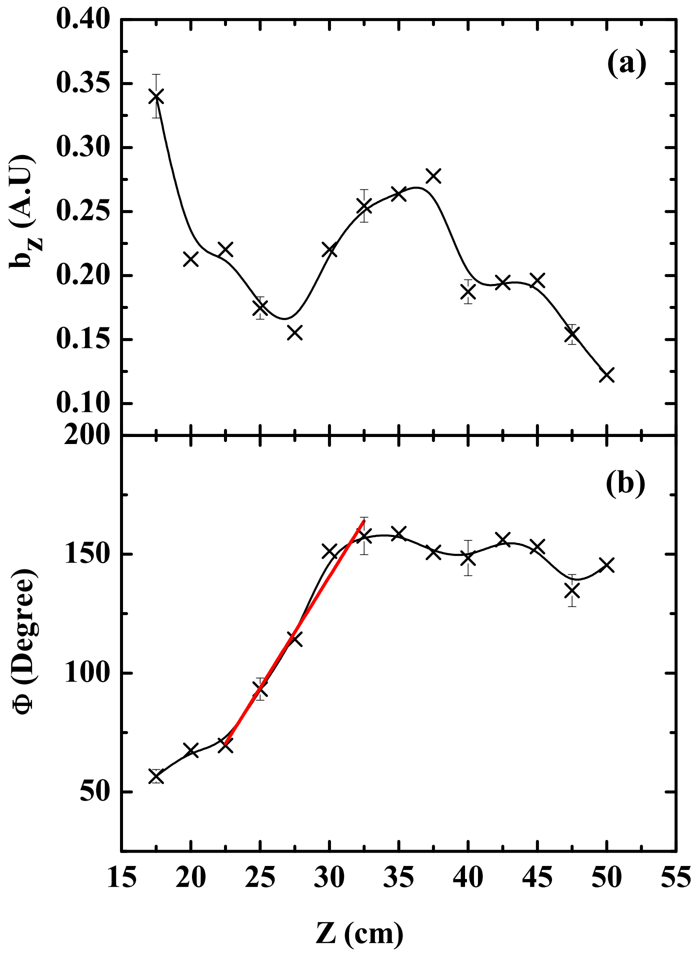

Figure 5.13: (a) Axial component of wave amplitude variation wave field and (b) is its phase at 4×10^{-4}mbar, 200W with 345G magnetic field in 3 to 6 magnet configuration, $\lambda_{\|} = 37$cm

Nonlinear Landau damping theory for wave electron trapping is another possible mechanism as proposed by Degeling [42, 55]. Electrons with velocity slower than the helicon wave get trapped in the longitudinal component of the wave electric field and are accelerated by taking energy from the wave. However, a simple linear landau damping mechanism might explain the present electron heating as explained below. Major helicon wavelengths in our experiment are nearly twice the antenna length and phase velocity is very close to the speed of electron impact ionization. This strongly supports the hypothesis of helicon wave Landau damping

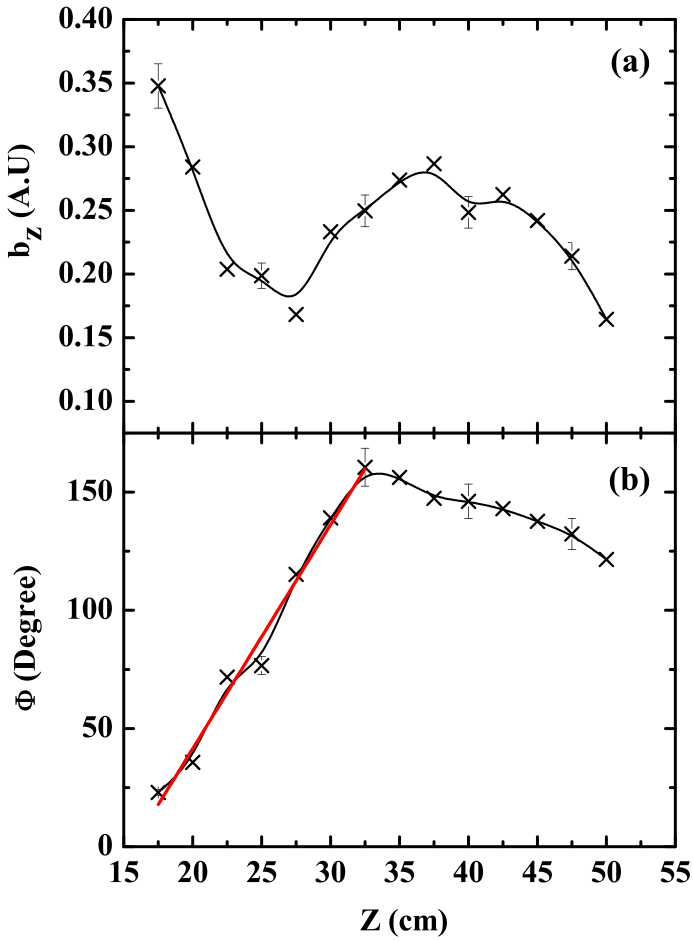

Figure 5.14: (a) Axial component of wave amplitude variation wave field and (b) is its phase at 4×10^{-4}mbar, 200W with 575G magnetic field in 3 to 6 magnet configuration, $\lambda_{\|} = 38$cm

heating and density production and determine the global density and temperatures of the plasma. However local damping of such axially propagating wave can cause to increase local electron temperature or accelerate electrons locally [54, 140]. In addition, it is also observe a standing wave character of wave magnetic field. This kind of standing wave feature of wave magnetic field leads to non-monotonic behavior of power deposition as observed by Kramer et al. [135]. The location of standing wave crest is analogous to the power deposition and heating location. This is very much consistent with our results. Therefore, it is concluded that linear

Landau damping with a standing wave pattern is responsible for power deposition as well as localized electron heating.

5.5.2 Theoretical model for downstream density rise

Downstream density rise is modeled using pressure and energy balance model to validate and compare with the experimental data. As mentioned earlier, the density increases at $Z \sim 55$ cm, after it hits a minimum value at $Z \sim 35$ cm along the Z-axis in the downstream region. Figures (5.1) (5.4) and (5.8) clearly showed that the density reaches to its minimum value at the location of electron temperature maximum and then it starts rising again reaching to its peak value at ~ 20 cm away from the T_e peak location. Moreover, the spatial distance between the T_e peak and density peak remain almost constant in all parameter regimes. Moving the gradient location of axial magnetic field further downstream pushes both the T_e peak location and following density peak location more towards downstream, without changing the distance between them. Experimental observations suggest in case of low magnetic field ($\sim 45G$), where the plasma potential remains almost uniform axially (week gradient), the percentage reduction in electron temperature is almost equal to the percentage increase in density.

5.5.2.1 Pressure balance model

Downstream density rise even after both the geometric and magnetic divergence is the most puzzling result. Incorporation of axial force balance equation like Chen et.al. [62, 128, 129] have used for their axially uniform geometric and magnetic field system. The electron equation of motion along the axial Z-direction is given by equation (5.1).

$$-enE_z - \frac{\delta(nkT_e)}{\delta z} - mn\nu_m u_z + F_{NL} = 0 \tag{5.1}$$

Where, u_z is the electron fluid velocity, ν_m is the electron collision frequency for momentum transfer. k is the Boltzmann constant. E_z is the axial electric field.

The collision term ($mn\nu_m u_z$) is negligibly small for our low pressure $\sim 4\times10^{-4}$mbar plasma. Other axial force, such as pondermotive force F_{NL} is very small. Therefore, the reduced electron equation of motion takes the following form (equation 5.2).

$$-enE_z - \frac{\delta(nkT_e)}{\delta z} = 0 \tag{5.2}$$

For our low magnetic field $\sim 45G$ case, where the axial electric field component is very weak as the plasma potential gradient is very low $E = -\frac{dV_s}{dz} \approx 0.7\text{V/cm}$. Therefore, neglecting this force term ($-enE_z$) from equation (5.2), the simplified force balance equation contains only the pressure term (equation 5.3).

$$\frac{\delta(nkT_e)}{\delta z} = 0 \tag{5.3}$$

Which gives the following (equation 5.4) pressure balance equation.

$$nT_e = constant \tag{5.4}$$

This relationship between T_e and n indicates that the amount of electron temperature drop must be reflected on the same incremental density rise. Taking the experimental electron temperature profile fitting with a function (5.5)

$$T_e = T_{e0} + A_1 exp{-}e^{-z_1} - z_1 + 1 \tag{5.5}$$

where $z_1 = \frac{(Z-z_c)}{W}$ and $T_{e0} = 6.7838, A_1 = 5.2839, W = 0.0417, z_c = 0.3793$ are taken Z is in meter. The calculated density profile using equation (5.4) shows close agreement with the experimental density profile. When the magnetic field strength is increase the axial potential gradient increases and as a consequence the electric field term in the force balance equation becomes significant causing ($\frac{\delta n}{n}$) and ($\frac{\delta T_e}{T_e}$) to vary independently. It is also observed in presence of moderate or strong axial plasma potentials in our collision less plasma, equation holds well keeping the non-zero electric field term in the force equation (5.2). Hence in the high

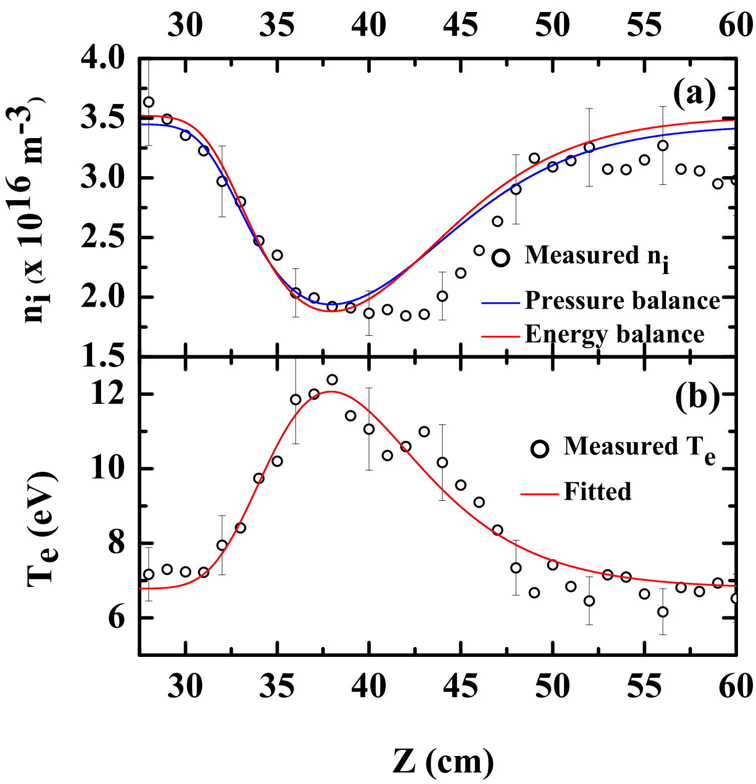

Figure 5.15: Pressure and energy balance model for validation of experimental result of figure 5.1, (a) circular data points are the measured densities, blue line is the calculated density using pressure balance, red line represents the calculated density using energy balance, (b) circular data points are the measured electron temperatures (T_e) and red line is the function (5.5) fitted into it.

magnetic field cases the observed percentage increment in density is less than the percentage reduction in electron temperature, because of presence of axial potential gradient in the bulk plasma as indicated in figure (5.16a). Like the similar way as before, we have fitted the experimental electron temperature profile changing the constant parameters (figure 5.16b) and calculate the axial density profile which is much higher than the experimentally observed downstream density rise. Presence of double layer like potential structure makes this difference. Potential hill trapped the energized/heated electrons, reducing the density on the other side of the hill hence the electron temperature has to be increased for maintaining the pressure balance. Hence linear relationship between the rate of falling T_e and rate of rising

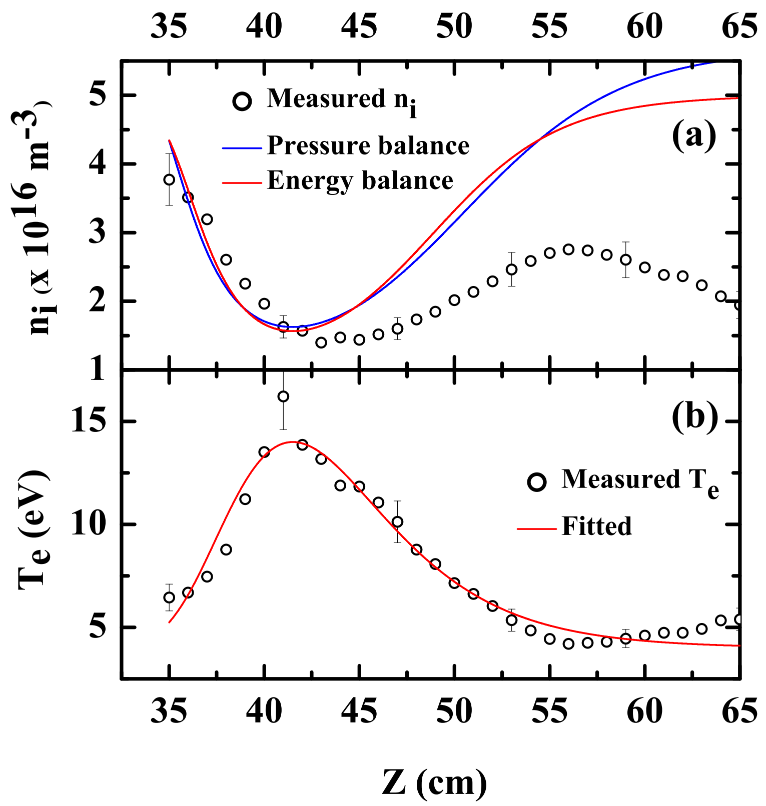

Figure 5.16: Pressure and energy balance model for validation of experimental result of figure 5.8 at 220G magnetic field, (a) circular data points are the measured densities, blue line is the calculated density using pressure balance, red line represents the calculated density using energy balance, (b) circular data points are the measured electron temperatures (T_e) and red line is the function (5.5) fitted into it.

density gets broken by the existence of plasma potential hill of different magnitudes in the downstream plasma generated due to different magnetic field strengths.

5.5.2.2 Energy balance model

Electron or ion density can be determined from the fundamental principle of energy conservation. The power absorbed (P_{abs}) from the source to produce the discharge must be equal to the total power lost from the system (equation 5.6).

$$P_{abs} = enU_B A_{eff} E_t \tag{5.6}$$

Where the power loss is equivalent to a pair of electron-ion escaping with Bohm velocity ($U_B = \sqrt{\frac{kT_e}{m_i}}$) through an effective area (A_{eff}) for total energy loss (E_t).

$$E_t = E_c + E_e + E_i \tag{5.7}$$

Where, $E_e = 2T_e$ is the electron kinetic energy loss and $E_i = \frac{T_e}{2} + V_S$ is the ion kinetic energy loss across the sheath near the surface or boundary. V_S is the sheath edge potential near the boundary, defined in equation (5.8).

$$V_S = T_e \ln(\frac{m_i}{2\pi m_i}) \tag{5.8}$$

Where, E_c is the collisional energy loss per electron-ion pair creation by elastic collision, excitation or ionization with background gas. The collisional energy for an electron-ion pair creation is defined in equation (5.9).

$$E_c = E_{iz} + E_{ex}\frac{k_{ex}}{k_{iz}} + \frac{k_{ex}}{k_{iz}}\frac{3m}{m_i}T_e \tag{5.9}$$

Where, E_{iz} is the ionization energy, E_{ex} is the excitation energy, k_{iz} is the ionization rate constant, k_{ex} is the excitation rate constant and k_{el} is the elastic scattering rate constant. The rate constants are depended with the electron temperature, therefore E_c is very much sensitive to electron temperatures. For Argon gas $E_{ex} = 12.14eV$, $E_{iz} = 15.76eV$ and the rate constants (k_{xx} in m^3/S) are approximated by Lieberman [89] as given in equation (5.10), (5.11) and (5.12).

$$k_{el} = 2.336 \times 10^{-14} T_e^{1.609} e^{0.0618(\ln T_e)^2 - 0.1171(\ln T_e)^3} \tag{5.10}$$

$$k_{iz} = 2.34 \times 10^{-14} T_e^{0.59} e^{-17.44/T_e} \tag{5.11}$$

$$k_{ex} = 2.48 \times 10^{-14} T_e^{0.33} e^{-12.78/T_e} \tag{5.12}$$

Although, these rate constants are well applicable for the temperature range $\sim (1-7)eV$, we have used them for up-to $\sim 12eV$ for our experiments. Effective particle loss area A_{eff} is defined for a cylindrical system as given in equation (5.6).

$$A_{eff} = A_s + A_d = h(\pi r_s^2 + 2\pi r_s l_s) + h(\pi r_d^2 + 2\pi r_d l_d) \tag{5.13}$$

Where r_s and l_s respectively are the radius and effective length of the source chamber, r_d and l_d respectively are the radius and effective length of the diffusion chamber and $h = \frac{n_s}{n_0}$ is the density ratio near the sheath edge, which is assumed to be same both at source and diffusion chamber. Our working pressure laying in the range $(1-50) \times 10^{-4}$ mbar where the collisional mean free path (λ) is $\sim$ meter, longer than our system dimensions. Therefore, the working pressure range belongs to low pressure regime, where ion transit into the sheath is collision-less and well described by an ion free fall profile within the bulk plasma. This profile is relatively flat near the plasma center and drops near the sheath edge, with $h = \frac{n_s}{n_0} \sim 0.4$ [89] for cylindrical geometry with axial length (l) much greater than radius (r). We have considered $r_s = 4.75cm$, $l_s = 10cm$ and $r_d = 10.5cm$, $l_d = 10cm$ ($\pm 10cm$ from the throat expansion) as the localized electron heating and downstream density rise is taking place between $Z = 35$ to 55 cm. Substituting all these parameters in the energy balance equation (5.6) for density calculation as given in equation (5.14).

$$n = \frac{P_{abs}}{eU_B(T_e)A_{eff}(r_s, l_s, r_d, l_d)E_t(T_e, r_s, l_s, r_d, l_d)} \tag{5.14}$$

For fixed r_s, l_s, r_d and l_d the density profile become solely a function of electron temperature profile. Taking the experimental electron temperature profile fitted with a function (5.5) as indicated in figure (5.15b) calculate $U_B(T_e)$, the collisional energy loss (E_c) and total energy loss (E_t) each point along the axis of the system (figure 5.17). The E_c shows a dip and E_t has the peak at $Z \sim 38$ cm where the localized heating is taking place. Collisional energy term is depended with all the rate coefficients which has temperature dependence. On the other hand total energy loss is depended on electron and ion kinetic energy loss together with the E_c. Where E_i and E_e have linear temperature dependence, which is more dominant loss than E_c. Therefore, location of the E_t peaking is consistent with the electron heating location. It is assumed for this calculation that the 50% of input RF power is deposited in the small volume of the plasma (from $Z = 35$ to 55 cm), which is also dissipated through the inner contributed plasma walls for this axial length. The calculated density profile (red curve) using the energy balance is shown in figure (5.15a). This result is very closely matched with the experimental profile as well as pressure balance model. Therefore, energy balance model is also confirmed the downstream density rise. It is to be noted that the power absorption is approximated $\sim 50\%$ of the input RF power within a specified volume of our interest. However this approximated power within the specified volume may change the absolute value of calculated density but not the axial density profile. Therefore, the incremental downstream density rise ($\frac{\delta n}{n}$) is very much consistent with the experimental results.

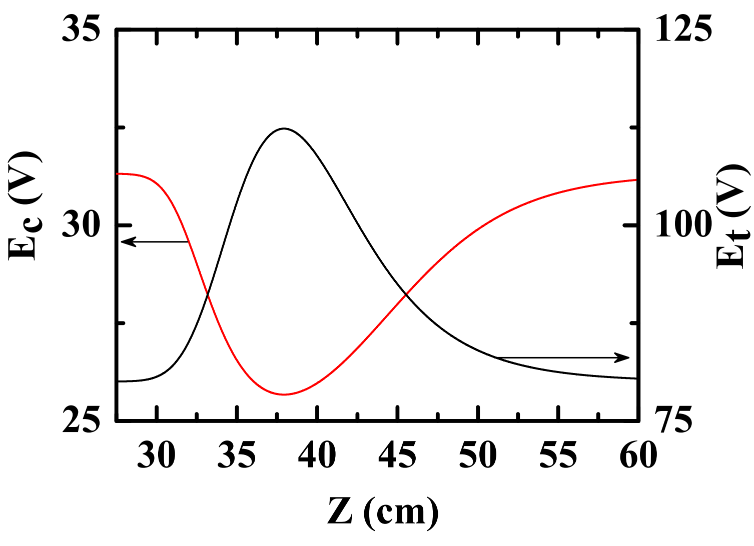

Figure 5.17: Collisional energy loss (E_c) indicated as red line and total energy loss (E_t) indicated as black line along the axis for the experimental condition of figure 5.1

5.6 Summary

In a linear helicon device with both geometrical and magnetic expansion, localized electron heating and density peaking have been observed at different axial locations in the downstream helicon plasma. Measurements of helicon wavelength is nearly twice the antenna length and phase velocity (v_p) is very close to the speed of electron impact ionization. Experimental results presented in this chapter is bearing good evidence of Landau damping heating and density production by the helicon waves, particularly in our low density plasma. In order to explain the underlying mechanisms causing these localized electron heating, axial profile of helicon wave field under different magnetic field configuration are measured. The localized electron heating which is taking place far away from the antenna, is explained by the helicon wave Landau damping with a standing wave pattern of axial wave field. A density trough is created at the location of the electron heating. As the electrons are heated locally, they will rapidly escape the volume they are being heated, creating a density trough in that location. Further downstream, density peak is observed $\sim 55 - 65$ cm away from the antenna to maintain the pressure constant. Both pressure balance and energy balance model bear a resemblance to the downstream density rise even after both geometric and magnetic expansion.

6

Inhomogeneous downstream plasma

6.1 Introduction

Earth diverging magnetic field leads to many astrophysical phenomena observed in space plasma. An electrostatic space charge layer or double layer belongs to one of such astrophysical facts, which has also been observed in laboratory plasma [5]. In a radio frequency (RF) plasma, having diverging magnetic field in association with geometrical expansion has shown to produce current free double layer like structures [4, 114, 123]. Axial potential structure formation in this kind of expanding helicon system produces thrust along the axial direction. However, the radial density distribution plays an important role for controlling and determining the axial thrust efficiency. Recent experiments in such an expanding RF plasma shows that radial density profile is hollow near the throat of the expansion [141] and it is believed that the radial electric field which generates a poloidal current (J) causes ($J \times B$) forces to the electrons and pushed them away from the central location [142]. Ions are also following them as they are electro-statically coupled to each other, creating annulus. The occurrence of this plasma annulus is also considered due to the combined effect of both the expansion. In this chapter it is shown that the annular plasma can be formed both in presence and absence of radial as well as axial potential structures or electric fields in expanding helicon plasmas. Therefore, further experimentation is required to investigate the root causes for this downstream annular plasma formation. Moreover, the dominant role between magnetic and geometrical aperture for the formation of downstream annular plasma is also unclear, which is also discussed along with controlling the annulus diameter in this chapter. Objective of this experiment is to understand the root cause behind the formation of downstream annular plasma and control its diameter.

The rest of this chapter is organized as follows: In section 6.2 observation of downstream annular plasma with independent role of magnetic or geometric aperture and radial electric field and its control are presented. Discussion is carried in section 6.3 followed by summary in section 6.4.

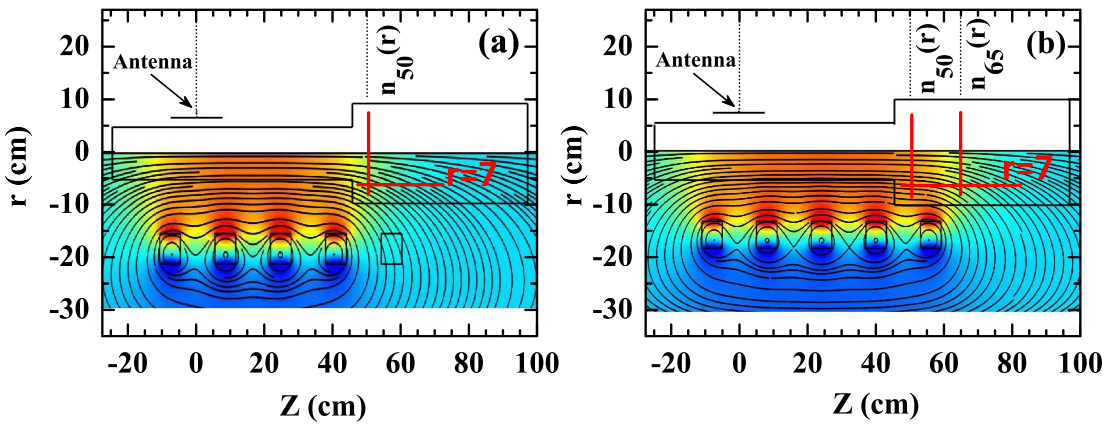

Figure 6.1: (a) is *close magneto-geometry aperture* (CMGA) configuration and (b) is the *far magneto-geometry aperture* (FMGA) configuration.

6.2 Downstream annular plasma

Experiments are carried out in **H**elicon **eX**perimental (**HeX**) system, using a right helicon antenna, powered by 13.56MHz RF generator in a geometrical expanding system in presence of variable external axial magnetic field gradient location. Plasma is produced inside the narrow glass tube and axially diffuse to the larger diameter diffusion chamber, we call this as expansion chamber. The glass to stainless steel chamber junction is called geometrical expansion. Geometrical expansion located Z=45 cm away from the antenna center (Z=0 cm) in HeX system. External axial magnetic field has been used to increase both electron and ion confinement. A 3D schematic of the experimental system with helical antenna and electromagnets shown in figure (4.1) in chapter 4.

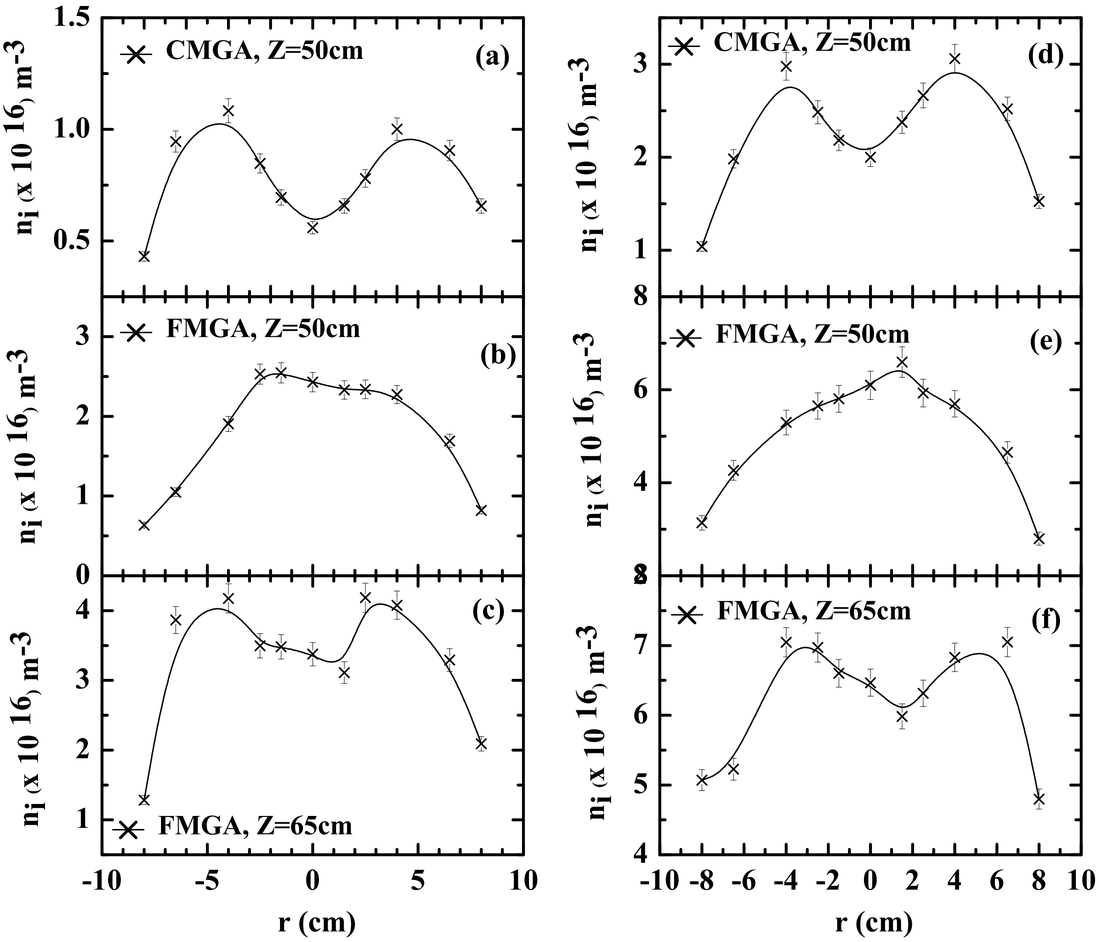

Figure 6.2: (a),(b) and (c) are the radial density profile at pressure 2×10^{-4}mbar; (d),(e) and (f) are the radial density profile at pressure 1×10^{-3} mbar; (a) and (d) are the plasma annulus at Z = 50cm, in CMGA configuration; (b) and (e) are the non-hollow plasma profile at Z = 50cm, in FMGA configuration; (c) and (f) are the plasma annulus at Z = 65cm, in FMGA configuration.

6.2.1 Role of magnetic and geometrical aperture

To investigate (a) the independent role of geometrical and magnetic expansion and (b) axial potential structures for the downstream annular plasma formation, Experiments are carried out with two different magnetic field configurations. In one configuration, 3 to 6 electromagnets have used, where the maximum diverging magnetic field gradient (Z = 46 cm) located close to the geometrical expansion (Z = 45 cm). We call it as *close magneto-geometry aperture* (CMGA) configuration (figure 6.1a). In another configuration, 3 to 7 electromagnets have used, where the maximum diverging magnetic field gradient (Z = 62 cm) located 17 cm far away from the geometrical expansion. We call it as *far magneto-geometry aperture* (FMGA) configuration (figure 6.1b). Triple Langmuir probe [75] is used to measure the radial density distribution, which is inserted into the system through the end flange of diffusion chamber. Triple probe assembly with ceramic housing attached to a English alphabet 'Z' shaped right angle bent rotatable shaft inserted off-axially (r=7 cm) into the system from the diffusion chamber end plate, permitting measurements in a circular arc. Standard trigonometric relation is used to convert this circular arc to radial length measurement. Radial density profile is measured at two axial locations Z = 50 cm and 65 cm from the antenna center ($Z = 0$) cm in both *CMGA* and *FMGA* configurations. Experimental results on radial density profiles are indicated in figure (6.2). At low pressure 2×10^{-4} mbar and low power 100W, in CMGA configuration, off-axial density peaking profile is observed at Z = 50 cm (figure 6.2a), which shows the annular plasma shape. Keeping all the parameter constant when the magnetic aperture is pushed 17 cm away from the antenna, i.e for FMGA configuration, the off-axial density peaking profile at Z = 50 cm has changed to on-axial peaked density profile (figure 6.2b). In FMGA configuration, keeping all other parameters constant, radial density profile after the magnetic divergence at Z = 65 cm is found to be hollow again where the the geometrical expansion does not have any significant role (figure 6.2c). This confirms that the magnetic field aperture is playing dominant role over the geometrical aperture for producing the annular plasma profile. High pressure 1×10^{-3} mbar plots shown in figure 6.2 (d) (e)and (f) established the facts. It is shown [87] that between the two magnetic field configurations, only CMGA configuration is suitable for axial potential structure formation. However, annular plasma is formed in both CMGA and FMGA configurations. Which also confirms that the annular plasma can be formed both in presence and absence of axial potential structures or electric fields.

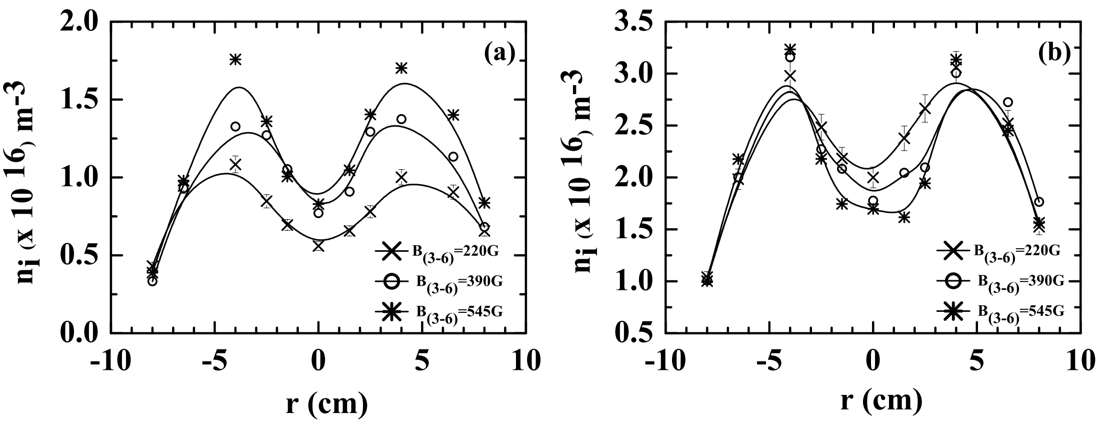

Figure 6.3: Radial density profile at Z = 50cm, with 100W RF power (a) pressure 2×10^{-4}mbar and (b) 1×10^{-3}mbar in CMGA configuration.

Table 6.1: Density hollowness($\frac{n_r - n_0}{n_r}$)% with the magnetic field

P ($mbar$)	I_B(Amp)	Hollowness(%)	P ($mbar$)	Hollowness(%)
2×10^{-4}	95	40	1×10^{-3}	33
	170	45		44
	250	55		53

6.2.2 Role of Radial Electric Field

Numerical simulation has been carried out by Rao and Singh [143], considering only electrons are magnetized in presence of current free double layers. Experiments are carried out with increasing magnetic field to make both electron and ions are magnetized in both the configurations. Density depth at the center with respect to the off-axial density peaking is defined as density hollowness $(\frac{n_{rp}-n_0}{n_{rp}})\%$, where n_{rp} is the off-axial peaked density and n_0 is the central minimum density. It is observed with increasing magnetic field in both configurations, where annular plasma is observed as shown in figure (6.3a). Density hollowness is also increase both at low 2×10^{-4} mbar (figure 6.3a) and high pressure 1×10^{-3} mbar (figure 6.3b). Quantitative representation of hollowness with the source magnetic field is presented in table 6.1. Higher magnetic field doesn't have any significant effect on changing the diameter of the plasma annulus. In FMGA configuration, hollow density profile is regenerated at Z = 65 cm after the magnetic divergence, where there is no axial potential structures [87]. Associated radial plasma potential (V_p) profile corresponding to these hollow density profiles are shown in figure (6.4b), indicating existence of very weak radial electric field $E_r = 0.1V/cm$, which does not have significant effect on the electron poloidal flow compared to other cases as observed in CMGA configuration (figure 6.5 b and d). In CMGA configuration at 100W radial electric fields are $E_r = 10V/cm$ and $E_r = 1V/cm$ respectively at low 2×10^{-4} mbar and high 1×10^{-3} mbar pressure. Hollow plasma is formed in both the cases. Therefore, downstream annular plasma can formed both with and without presence of radial electric field (E_r).

6.2.3 Control of plasma annulus

Experiments are carried out to control the diameter of plasma annulus. At low pressure 2×10^{-4} mbar with increasing RF power it is observed that the diameter of the annulus decreases. The two arrow marks in figure (6.5a) is indicated the decreasing tend with RF power. At high pressure 1×10^{-3} mbar even at 800W RF power hollowness is found to be vanished completely as shown by the two arrow marks in figure (6.5c). Quantitative representation of this diameter reduction with RF power both at low and high pressure is tabulated in table 6.2.

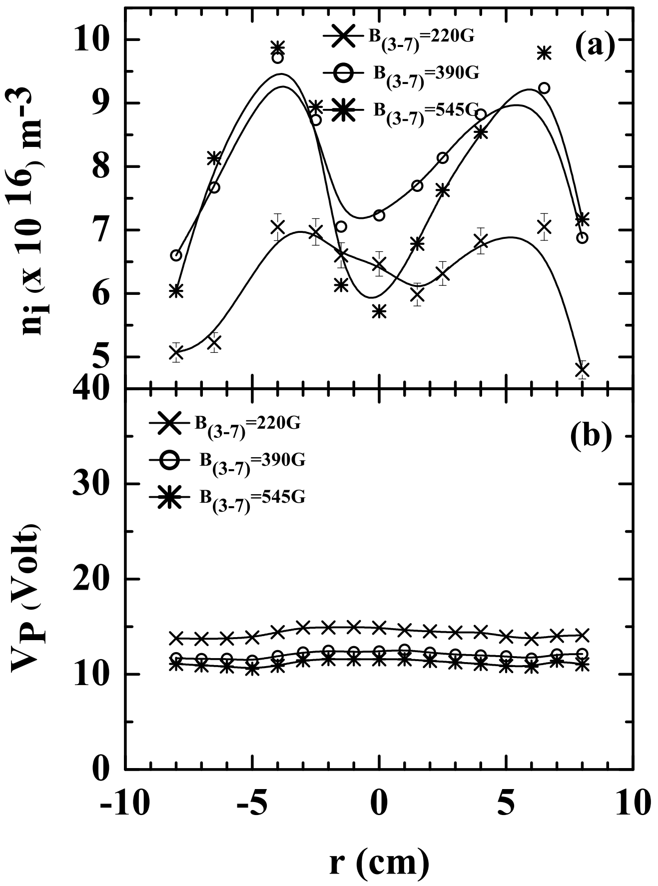

Figure 6.4: (a) is the radial density profile at Z = 65cm, pressure 1×10^{-3}mbar, 100W in FMGA configuration, with increasing source magnetic field, and (b) is the corresponding plasma potential profile.

6.3 Discussion

There are two possible explanations available on this downstream annular plasma formation. First one relies on the presence of radial electric field where ions are unmagnetized. This causes electron current induced by $\mathbf{E} \times \mathbf{B}$ velocity and consequently $\mathbf{J} \times \mathbf{B}$ outer-ward force leads to hollow density profile. In our case not only electric field is weak, ions are also magnetized. Therefore, this mechanism as reported in reference [142, 143] is not applicable to explain our results. The second one relies on the existence of tail electrons confined only at off-axis [141]. To understand the root cause behind the off-axial density peaking, electron en-

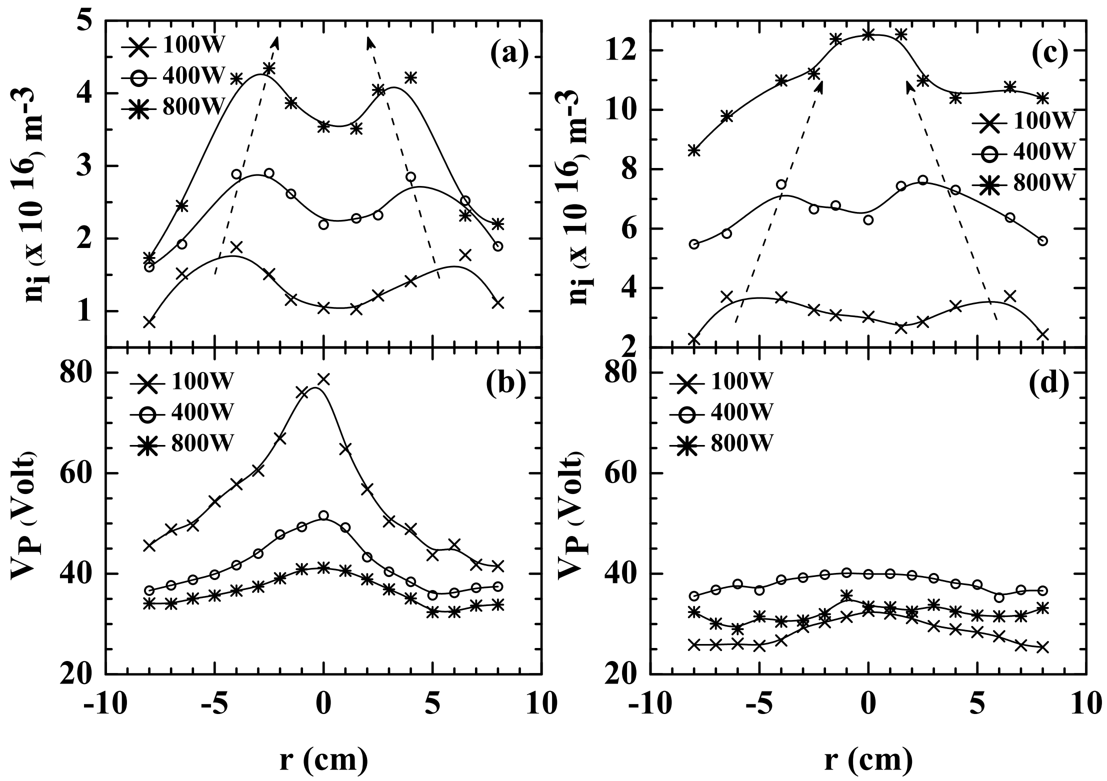

Figure 6.5: (a) is the radial density profile at Z = 50 cm, pressure 2×10^{-4}mbar, in CMGA configuration, with increasing RF power, at 210G source magnetic field and (b) is the corresponding plasma potential profile. (c) is the radial density profile at Z = 50cm, pressure 1×10^{-3}mbar, in CMGA configuration, with increasing RF power, at 210G source magnetic field and (d) is the corresponding plasma potential profile.

ergy probability function (EEPF) [144, 145] is measured off-axially (r = 7 cm) in FMGA configuration in the expansion chamber. Measurement of EEPFs are performed using a 4 mm long 0.5 mm radius cylindrical RF-compensation single Langmuir probe [74] inserted off-axially at r = 7 cm into the system from the diffusion chamber end flange. Sweeping bias voltage is applied to the probe and the current collection by the probe is measured across a resistance, to get $(I - V)$ characteristics. An active analog circuit is used to double differentiate the collected current with respect to the applied bias voltage to determine EEPF, which is more general method to measure electron temperature from the single Lang-

Table 6.2: Diameter (D) of annulus with RF power

P_{RF}W	P $(mbar)$	$D_{Annulus}$(cm)	P $(mbar)$	$D_{Annulus}$(cm)
100		10		10
400	2×10^{-4}	7	1×10^{-3}	5
800		4		Nil

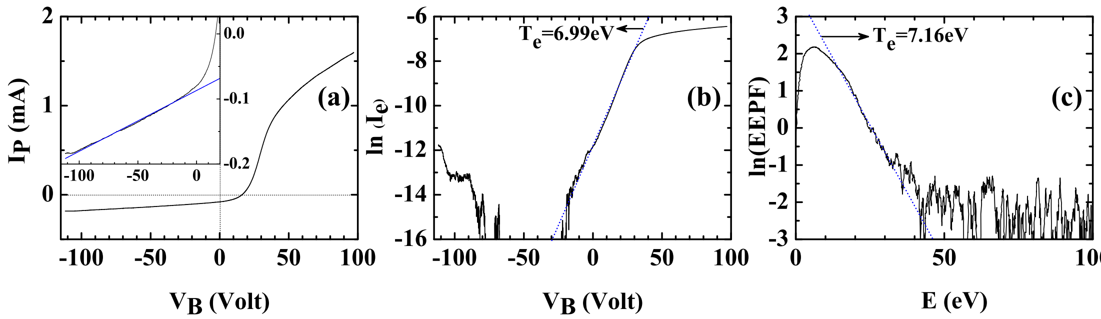

Figure 6.6: (a) is the Langmuir probe characteristics, (b) is the electron temperature from $ln(I_e)$ Vs V_B curve and (c) is the electron temperature from EEPF at 400W, 2×10^{-4}mbar, in FMGA configuration, at $(r, z) = (7, 60)$ cm.

muir probe data. Logarithm of this EEPF is inversely proportional to the electron temperature. The linear regime of $ln(EEPF)$ represents the electron temperature. Presence of two component electrons are represented by two distinct linear regimes, which indicates the presence of different energetic electrons population [146, 147]. Electrons near and away from the plasma potential are respectively called the bulk and tail electrons.

Measurement of EEPFs are shown at three axial location at $Z = 60$ cm, before the magnetic aperture, at $Z = 72.5$ cm just after the magnetic aperture, where the *Last Continuous Magnetic Field Line* (LCMFL) pass through from source to diffusion chamber without intercepting the geometrical expansion throat and $Z = 77.5$ cm far away from the magnetic aperture. Unlike the two locations Z $= 60$ cm (figure 6.6) and $Z = 77.5$ cm (figure 6.8), $Z = 72.5$ cm (figure 6.7) data shows the existence of tail electrons having temperature $\sim 21eV$. These tail electrons are created inside the the source chamber and confined at off-axial

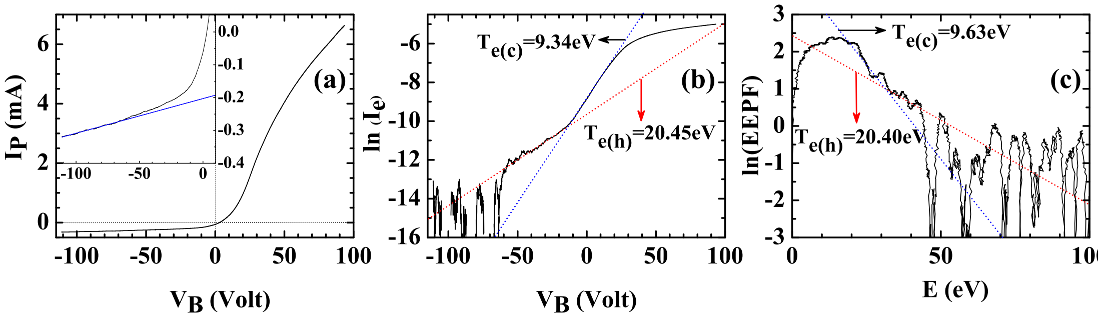

Figure 6.7: (a) is the Langmuir probe characteristics, (b) is the electron temperature from $ln(I_e)$ Vs V_B curve and (c) is the electron temperature from EEPF at 400W, 2×10^{-4}mbar, in FMGA configuration, at $(r, z) = (7, 72.5)$ cm.

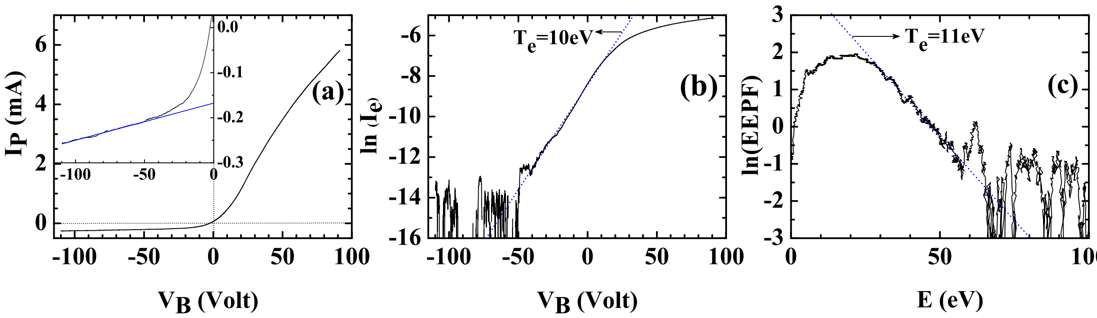

Figure 6.8: (a) is the Langmuir probe characteristics, (b) is the electron temperature from $ln(I_e)$ Vs V_B curve and (c) is the electron temperature from EEPF at 400W, 2×10^{-4}mbar, in FMGA configuration, at $(r, z) = (7, 77.5)$ cm.

location by the axial magnetic fields. Similar observation on existence of tail electron in connection with the downstream annular plasma formation has also been reported [141]. They conjectured that the ionization by these off-axial tail electrons with background neutral may cause for this off-axial density peaking. However, the calculated collisional mean free path for these tail electrons $\sim 21eV$ with background neutrals is $\sim \frac{1}{n_n \sigma} \sim 10$ meter, which is much higher than the system length. Therefore, to explain the results, we invoke the possibilities of ionization of wall recycling neutrals. The LCMFL is the probable way of extraction of these tail electrons from source to diffusion chamber. The ion Larmor radius (ρ_i) is calculated for this LCMFL (figure 6.9), which shows at $Z = 65$ cm, $\rho_i = 4.2$ cm. Therefore, the ions following the LCMFL touches the conducting expansion

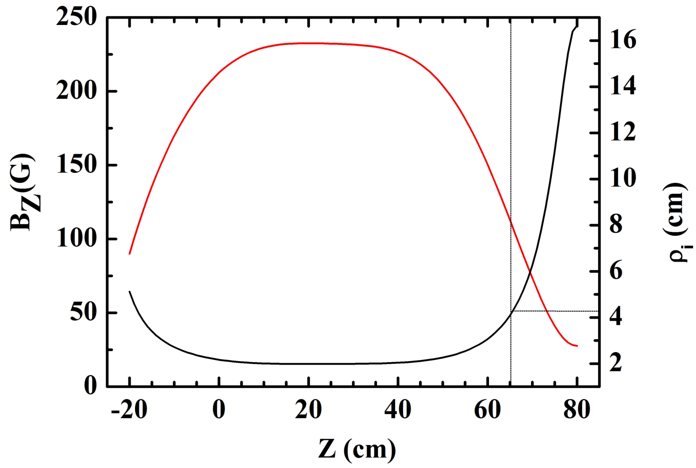

Figure 6.9: *Last Continuous Magnetic Field Line* (LCMFL) from source to diffusion chamber without intercepting the geometrical expansion throat (Red line). Calculated ion Larmor radius each point on this LCMFL (Black line).

chamber wall at $Z = 65$ cm, although the field line touches the wall at $\sim 80cm$. Those ions at this location near the wall recombine and produce neutrals. These neutrals are the fuel for sustaining the plasma called recycling neutrals [148]. The recycling neutral thermal speed is $v_{th(n)} = \sqrt{\frac{3k_B T_{wall}}{M_n}}$, where k_B is the Boltzmann constant and M_n is the argon atom mass. This gives recycling neutral thermal speed $\sim 400m/s$, considering wall is at room temperature ($T_{wall} \sim 300K$). Neutral ionization length is defined as $\lambda_{iz} = \frac{v_{th(n)}}{\nu_{iz}}$, where neutral ionization frequency $\nu_{iz} = K_{iz}n_e$. K_{iz} is the rate constant, equal to $1 \times 10^{-13}m^3/s$ for $21eV$ tail electrons [89]. Local electron density (n_e) at that location $6 \times 10^{16}m^{-3}$. This gives recycling neutral ionization length $\lambda_{iz} = \frac{v_{th(n)}}{\nu_{iz}} \sim 6$ cm from the wall. The off-axial density rise in this case is at 4 cm away from $r = 0$ cm. Hence the off-axial density peaking location from wall is $\sim (10.5 - 4) = 6.5$ cm, which is closely matches with the recycling neutral ionization length. This may be the cause of downstream annular plasma after the magnetic expansion.

6.4 Summary

The following conclusion is made from the results presented in this chapter.

(a) Experimental results show that when magnetic and geometric aperture closely coincide, annular plasma formation occurs beyond both of these two expansions. Moreover, by shifting the magnetic aperture away from the fixed geometrical aperture, the annular plasma always precedes the location of magnetic aperture. No hollow profile is observed immediately after the geometric aperture. This led us to conclude that the magnetic aperture is playing dominant role over geometrical aperture for the formation of annular plasma profile.

(b) It is observed that the annular plasma can be formed in presence of both at high $\sim 10V/cm$ as well as very low $\sim 0.1V/cm$ radial electric field. This shows that the downstream annular plasma formation is independent of radial electric field.

(c) Experiments have been performed at low $\sim 100G$ as well as high $\sim 260G$ magnetic field near the annulus. Low magnetic field $\sim 100G$ corresponds to unmagnetized ions whereas ions are magnetized at $\sim 260G$. In both the cases electrons are magnetized. Hence, plasma annulus has been formed even when both electron and ions are magnetized.

(d) The calculated collisional mean free path for $\sim 21eV$ tail electrons with background neutrals is $(\sim \frac{1}{n_n \sigma}) \sim 10$ meter, which is much higher than the system length, where n_n is the neutral density and σ is the collisional cross-section. Whereas wall recycling neutrals with thermal velocity ~ 400 m/s gives the ionization length ~ 6 cm. Therefore, recycling neutral ionization with the off-axially confined tail electron may cause to create the downstream annular plasma formation.

7

Conclusion and future scope

7.1 Conclusion

The content of this thesis provides a detailed experimental study of downstream physics of expanding helicon plasmas. Plasma expansion from narrow source chamber to wide expansion chamber is associated with complex transport phenomena including double layer like potential structure formation and instabilities. In this kind of systems, ionization dominates mainly in the source chamber and geometrical expansion leads to a gradient in the plasma density, decreasing from source to the expansion chamber. The experimental system consists of dielectric glass source chamber and stainless steel conducting expansion chamber. Plasma is produced by RF, no such active electrode is participating into the plasma. When electron or both electron and ions are magnetized, magnetic field lines tied them and bring out from the source chamber. Since the source chamber is made up of dielectric so there is no chance of getting a ground. Therefore, the only possibility is the expansion chamber to get the nearest ground. Therefore, the magnetic field lines will dictate source plasma to get a ground. By changing the magnetic field profile one can terminate the field line near at the expansion or it can be terminated far more inside the expansion chamber. Thesis provides a comprehensive study on this downstream plasma away from the helical antenna.

The diagnostics used for this thesis experiments are the high frequency magnetic probe for wave field measurements, retarding field energy analyzer (RFEA) for ion beam energy and ion energy distribution function (IEDF) measurements, RF compensated single Langmuir probe [74], double probe, triple probe [75] for local density, temperature and floating potential measurements, emissive probe [76] for plasma potential measurement, RF current probe for antenna, plasma impedance measurement. Flexible RFEA design provides easy mechanical and electrical access, which make it unique in its class. Entering energetic electrons into the RFEA cavity, bias voltage scheme, offset adjustment, capacitive pick up problems are addressed to make the RFEA working in this RF environments. RF compensation technique is limited only at high density ($> 10^{17}m^{-3}$) RF plasmas. RF compensation of Single Langmuir probe at low density RF plasmas ($\sim 10^{16}m^{-3}$) is discussed in this thesis. $\sim 2.5eV$ electron temperature compensation is achieved by using ($A_X >>> A_P$) even with the impedance limitation of the available self-resonating choke in low density plasma. The conventional triple probe method is very much useful for instantaneous measurements, but due to non-uniform potential distributions of three probes [99] and inappropriate choice of bias voltage, it underestimates or overestimates electron temperature compared to double and single probe measurements in different situations and require compensation to obtain correct temperature values. A through investigation has been carried out for accurate electron temperature using the triple probe. Appropriate bias voltage for properly compensated electron temperature measurement is in the range $5V_{d2} < V_{d3} < 10V_{d2}$. If the bias voltage ($V_{d3}$) is above $10V_{d2}$, compensated T_e values using triple probe are higher than double probe values whereas if the bias voltage (V_{d3}) is less than $5V_{d2}$, compensated T_e values are found to be less than the corresponding double probe measurements. This may be due to the fact that the relation $I^2 \propto V_B$ remains linear only in an intermediate bias voltage range for cylindrical probe[107]. At lower bias when $V_{d3} < 5V_{d2}$ probe is at a potential which is quite below that of its ion saturation, whereas at higher bias particularly when $V_{d3} > 10V_{d2}$, ions enters to the sheath too fast to be absorbed by the probe therefore creating a space charge limited zone around the probe.

Multiple axial potential structures (MAPS) have been observed first time in our expanding helicon plasma. It is known that for the existence of a double layer like potential structure there must be maintained a density above a critical value at the upstream. Therefore, for multiple of such structure there must exist non-uniform axial density distribution. Experimentally it has been verified, simultaneously with plasma potential scan with density and temperature profile.

In a linear helicon device with both geometrical and magnetic expansion, localized electron heating and density peaking have been observed at different axial locations in the downstream helicon plasma. Measurements of helicon wavelength is nearly twice the antenna length and phase velocity (v_p) is very close to the speed of electron impact ionization. Experimental results presented in this chapter is bearing good evidence of Landau damping heating and density production by the helicon waves, particularly in our low density plasma. In order to explain the underlying mechanisms causing these localized electron heating, axial profile of helicon wave field under different magnetic field configuration are measured. The localized electron heating which is taking place far away from the antenna, is explained by the helicon wave Landau damping with a standing wave pattern of axial wave field. A density trough is created at the location of the electron heating. As the electrons are heated locally, they will rapidly escape the volume they are being heated, creating a density trough in that location. Further downstream, density peak is observed $\sim 55 - 65$ cm away from the antenna to maintain the pressure constant. Both pressure balance and energy balance model bear a resemblance to the downstream density rise even after both geometric and magnetic expansion.

Radial density inhomogeneity or annular plasma formation detriments the axial thrust efficiency for electric propulsion, where the rotational kinetic energy is converted into axial kinetic energy due to gas dynamical expansion from narrow source to wide expansion chamber. It is shown that the annular plasma can be formed both in presence and absence of radial as well as axial electric fields. Presence of tail electrons are observed only at the off axial location where the density is piling up. Calculation of ionization length for recycling neutrals shows that the recycling neutrals with off-axially confined tail electrons may give probable explanation for this annular plasma formation. The magnetic aperture is playing dominant role over geometrical aperture for annular plasma formation.

7.2 Future scope

Our expanding helicon plasma system is capable of producing current-less double layer like potential structure. However it can be make current driven by replacing the dielectric end plate into a conducting plate and electrically connect this end plate to the conducting expansion chamber. While transition from current free to current driven how does the strength of potential structure varies is unknown. This study will bridge the double layer like potential structure study between helicon plasma as well as the glow discharge or filament plasmas.

It is observed that the tail electrons are confined only at off-axis. However the reason has not been properly understood yet. Our initial guess is that in our parameter space the power coupling is taking place simultaneously both by helicon wave and Trivelpiece-Gould (TG) mode. TG mode is localized at the edge which may transfer energy to electrons at the edge. There is no such studied has been carried out to understand the TG wave to electron interaction, which can be perused to find out the root cause behind this off-axially localized tail electrons. Another possibility of resonance electron interaction with RF field may also be responsible for this off-axially localized tail electrons.

In this thesis it has been throughly investigated the downstream regime of the expanding helicon plasma using half wave right helical antenna. It is observed that half wave right helical antenna is superior than full wave antenna having similar helicity. The term superior consider here because the half wave right helical antenna produced more downstream plasma compared to the full wave helical antenna. There is no explanation is available to support this effect. Full wave antenna length is $l_F = 2l_H = \lambda$; where l_F and l_H respectively are the full and half wave antenna length, λ is the helicon wave length. The k spectra of energy deposition by the full wave antenna will be more than the half wave antenna $l_H = \frac{\lambda}{2} = l$, where l is the antenna length. Energy will be spread more in k in half wave antenna than full wave antenna. Therefore, full wave antenna should acts as more efficient than half wave antenna. However, the experiment shows exactly the opposite. Therefore, there must be some more physical parameter such as antenna loading or other phenomena such as faster radial transport in the full wave antenna case compared to half wave case may be studied to explain the superiority of half wave right helicon antenna.

Equilibrium plasma profiles before and after the throat are very different in terms of stability determination. Therefore, study of instability in that transition zone will be interesting for basic plasma studies as well as controlling thrust efficiency for thruster application purpose. Strong gradients in electron temperature, density and plasma potential both in axial and radial direction in cylindrical geometry can be the sufficient free energy source for the instability.

Bibliography

[1] http://www.nap.edu/catalog/11960/plasma-science-advancing-knowledge -in-the-national-interest

[2] G. Hairapetian, 1990, Phys. Rev. Lett. 65, 175.

[3] N. Hershkowitz, 1985, Space Science Rev. 41, 351-391.

[4] C. Charles and R. Boswell, 2003, Appl. Phys. Lett. 82, 1356.

[5] L. P. Block, 1978, Astrophys. Space Sci., 55, 1, 59-83.

[6] G. Knorr and F. W. Crawford, 1974, Astrophys. Space Sci. 31, 209.

[7] J. E. Borovsky, 1986, Astrophys. J., 306, 451.

[8] R. W. Boswell, 1970, Phys. Lett. A, 33, 457.

[9] R. W. Boswell, 1984, Plasma Phys. Control. Fusion, 26, 1147.

[10] A. J. Perry, D. Vender and R. W. Boswell, 1991, Journal of Vacuum Sci. Tech. B, 2, 310-317.

[11] S. J. Wang, J. G. Kwak, C. B. Kim, and S. K. Kim, 2003, Phys. Lett. A, 313, 278-283.

[12] B. C. Master, T. K. Gray, D. N. Ruzic, and R. Stubbers, 2005, 21^{st} Symposium on Fusion Engineering, IEEE.

[13] R. A. Stubbers, B. E. Jurczyk, J. L. Rovey, M. D. Coventry, D. A. Alman, and M. L. R. Walker, 2007, 43^{rd} AIAA/ASME/SAE/ASEE Joint Propulsion Conference & Exhibit.

[14] P. K. Loewenhardt, B. D. Blackwell, R. W. Boswell, G. D. Conway, and S. M. Hamberger, 1991, Phys. Rev. Lett. 67, 2792.

[15] S. J. Jeon, W. Choe, G. C. Kwon, J. H. Kim, H. S. Yi, W. Herr, H. Y. Chang, 1998, 20^{th} Symposium on fusion technology.

[16] S. K. P. Tripathi and D. Bora., 2002, Nuclear fusion, 42, 10, L15.

[17] F. R. Chang Diaz, 2001, AIP Conference Proceedings, 595, 3.

[18] W. D. Michael, C. Charles, and R. W. Boswell, 2008, Journal of Propulsion and Power, 24, 134-141.

[19] C. Charles, 2007, Plasma Sources Sci. Technol. 16, R1-R25.

[20] N. Singh, 2011, Phys. Plasmas 18, 122105.

[21] C. Charles, R. W. Boswell, R. Laine, and P. MacLellan, 2008, J. Phys. D: Appl. Phys. 41, 175213.

[22] K. Takahashi, C. Charles, R. Boswell and A. Ando, 2014, Plasma Sources Sci. Technol. 23, 044004.

[23] K. Takahashi, A. Komuro and A. Ando, 2015, Plasma Sources Sci. Technol. 24, 055004.

[24] S. C. Thakur, A. Hansen, and E. E. Scime, 2010, Plasma Sources Sci. Technol., 19 025008.

[25] M. Wiebold, Y. T. Sung, and J. E. Scharer, 2011, Phys. Plasmas 18, 063501.

[26] X. Sun, A. M. Keesee, C. Biloiu, E. E. Scime, A. Meige, C. Charles, and R. W. Boswell, 2005, Phys. Rev. Lett. 95, 025004.

[27] L. Conde and L. Leon, 1994, Phys. Plasmas 8, 2441.

[28] C. Chan and N. Hershkowitz, 1982, Phys. Fluids. 25, 2135.

[29] Ch. Hollenstein, M. Guyot, and E. S. Weibel., 1980, Phys. Rev. Lett. 45, 2110.

[30] B. B. Sahu, A. Ganguli, and R. D. Tarey, 2013, Appl. Phys. Lett. 103, 184105.

[31] P. Coakley and N. Hershkowitz, 1976, Phys. Fluids. 22, 1171.

[32] C. Ionita, D. G. Dimitriu, R. W. Schrittwieser., 2004, Int. J. Mass Spectrom. 233, 343.

[33] H. Barkhausen, 1919, Physik. Z. 20, 401.

[34] H. Barkhausen, 1930, Proc. IRE, 18, 1155.

[35] D. G. Swanson, 2002, Plasma waves, Second Edition.

[36] P. Chabert and N. Braithwaite, 2011, Physics of radio-frequency plasmas, First Edition.

[37] A. W. Trivelpiece, and R. W. Gould, 1959, Jour. Appl. Phys. 30, 1784-1793.

[38] D. D. Blackwell, T. G. Madziwa, D. Arnush, and F. F. Chen, 2002, Phys. Rev. Lett. 88, 145002.

[39] R. Boswell, R. Porteous, A. Prytz, A. Bouchoule, and P. Ranson, 1982, Phys. Lett. A, 91, 163.

[40] F. F. Chen, 1991, Plasma Phys. Controlled Fusion 33, 339.

[41] A. R. Ellingboe and R. W. Boswell, 1996, Phys. Plasmas 3, 2797.

[42] A. W. Degeling, C. O. Jung, R. W. Boswell and A. R. Ellingboe, 1996, Phys. Plasmas, 3, 2788-2796.

[43] L. Porte, S. M. Yun, D. Arnush, and F. F. Chen, 2003, Plasma Sources Sci. Technol. 12, 287-293.

[44] K. P. Shamrai, and V. B. Taranov, 1996, Plasma Sources Sci. Technol., 5. 474-491.

[45] R. L. Kinder, A. R. Ellingboe and M. J. Kushner, 2003, Plasma Sources Sci. Technol., 12. 561-575.

[46] J. P. Klozenberg B. McNamara and P.C. Thonemann, 1965, Jour. Fluid Mech. 21, 545-563.

[47] B. Davies and P. J. Christiansen, 1969, Plasma Physics, 11, 987-1000.

[48] R. W. Boswell, 1973, Australian Journal of Physics, 25, 403-407.

[49] F. F. Chen, M. J. Hsieh, and M. Light, 1994, Plasma Sources Sci. Technol. 3, 49.

[50] R. T. S. Chen, R. A. Breun, S. Gross, N. Hershkowitz, M.-K. J. Hseih, and J. Jacobs, 1995, Plasma Sources Sci. Technol. 4, 337.

[51] M. Light and F. F. Chen, 1995, Phys. Plasmas, 2, 1084.

[52] M. Light, I. D. Sudit, F. F. Chen and D. Arnush, 1995, Phys. Plasmas, 2, 4094.

[53] S. M. Tysk, C. M. Denning, J. E. Scharer, and K. Akhtar, 2004, Phys. Plasmas, 11, 878.

[54] A. R. Ellingboe, R. W. Boswell, J. P. Booth and N. Sadeghi, 1995, Phys. Plasmas, 2, 1807-1809.

[55] A. W. Degeling, and R.W. Boswell, 1997, Phys. Plasmas, 4, 2748.

[56] A. Komori, T. Shoji, K. Miyamoto, J. Kawai, and Y. Kawai, 1991, Phys. Fluids B, 3, 893.

[57] P. A. Keiter, E. E. Scime, and M. M. Balkey, 1997, Phys. Plasmas, 4, 2741.

[58] F. F. Chen, and D. D. Blackwell, 1999, Phys. Rev. Lett. 82, 2677.

[59] F. F. Chen, and D. Arnush, 1997, Phys. Plasmas, 4, 3411.

[60] D. Arnush, and F. F. Chen, 1998, Phys. Plasmas, 5, 1239.

[61] A. I. Akhiezer, V.S. Mikhailenko, and K.N. Stepanov, 1998, Physics Letters A, 245, 117-122.

[62] F. F. Chen, 1996, Phys. Plasmas, 3, 1783.

[63] J. L. Kline, and E. E. Scime, 2003, Phys. Plasmas, 10, 135.

[64] R. W. Boswell, O. Sutherland, C. Charles, J. P. Squire, F. R. Chang Diaz, T. W. Glover, V. T. Jacobson, D. G. Chavers, R. D. Bengtson, E. A. Bering, R. H. Goulding, and M. Light, 2004, Phys. Plasmas, 11, 5125.

[65] G. Chen, A. V. Arefiev, R. D. Bengtson, B. N. Breizman, C. A. Lee, and L. L. Raja, 2006, Phys. Plasmas, 13, 123507.

[66] J. L. Kline, E. E. Scime, P. A. Keiter, M. M. Balkey, and R. F. Boivin, 1999, Phys. Plasmas, 6, 4767.

[67] M. M. Balkey, R. Boivin, J. L. Kline, and E. E. Scime, 2001, Plasma Sources Sci. Technol. 10 284.

[68] J. L. Kline, E. E. Scime, R. F. Boivin, A. M. Keesee, X. Sun, and V. S. Mikhailenko, 2002, Phys. Rev. Lett. 88, 1950021.

[69] J. L. Kline, E. E. Scime, R. F. Boivin, A. M. Keesee, and X. Sun, 2002, Plasma Sources Sci. Technol. 11, 413-425.

[70] E. E. Scime, J. Carr Jr., M. Galante, R. M. Magee, and R. Hardin, 2013, Phys. Plasmas, 20, 032103.

[71] Y. Sakawa, N. Koshikawa, and T. Shoji, 1993, Appl. Phys. Lett, 69, 1695-1697.

[72] D. Arnush, 2000, Phys. Plasmas, 7, 3042.

[73] R. B. Schulz, V. C. Plantz, and D. R. Brush, 1988, IEEE Trans. Elec. Mag. Compatibility, 30, 3.

[74] I. D. Sudit, and F. F Chen, 1994, Plasma Sources Sci. Technol. 3, 162-168.

[75] S. Ghosh, K. K. Barada, P. K. Chattopadhyay, J. Ghosh, and D. Bora, 2015, Plasma Sources Sci. Technol. 24, 015017.

[76] J. P. Sheehan and N. Hershkowitz, 2011, Plasma Sources Sci. Technol. 20, 063001.

[77] D. L. Rudakov, M. G. Shats, R. W. Boswell, C. Charles, and J. Howard, 1999, Rev. Sci. Instrum. 70, 476.

[78] K. Denieffe, C. M. O. Mahony, P. D. Maguire, D. Gahan, and M. B. Hopkins, 2011, J. Phys. D: Appl. Phys. 44, 075205.

[79] R. A. Pitts, R. Chavan, S. J. Davies, S. K. Erents, G. F. Matthews, G. Neill, J. E. Vince, JET-EFDA workprogramme contributors, and I. Duran, 2003, Rev. Sci. Instrum. 74, 4644.

[80] J. A. Simpson, 1961, Rev. Sci. Instrum. 32, 1283.

[81] P. Horowitz and W. Hill, 1989, The art of electronics, Second edition.

[82] S. Franco, 1988, Design with operational amplifier and analog integrated circuits, International edition.

[83] A. Boschi and F. Magistrelli, 1963, Nuovo Cimento 29, 487.

[84] V. A. Godyak, R. B. Piejak and B. M. Alexandrovich, 1992, Plasma Sources Sci. Technol. 1, 36-58.

[85] U. Flender, B. H. Nguyen Thi, K. Wiesemann, N. A. Khromov, and N. B. Kolokolov, 1996, Plasma Sources Sci. Technol. 5, 61-69.

[86] N. Hershkowitz, 1989 Plasma Diagnostics ed, O Auciello, and D L Flamm (New York: Academic), vol 1, pp 117.

[87] S. Ghosh, K. K. Barada, P. K. Chattopadhyay, J. Ghosh and D. Bora, 2015, Plasma Sources Sci. Technol. 24 034011.

[88] M. U. Siddiqui, and N Hershkowitz, 2014, Phys. Plasmas, 21, 020707.

[89] M. A. Lieberman and A. J. Lichtenberg, 2005, Principle of plasma discharge and material processing, Second edition.

[90] B. Crowley, D. Homfray, S.J. Cox, D. Boilson, H.P.L. de Esch and R.S. Hemsworth, 2006, Nucl. Fusion 46, S307-S312.

[91] H. Motto-Smith and I. Langmuir, 1926, Phys. Rev. 28, 727.

[92] V. A. Godyak, R. B. Piejak and B. M. Alexandrovich, 1992, Plasma Sources Sci. Technol. 1, 36-58.

[93] Yi-Ming Ling, 2005, Phys. Plasmas 12, 113504.

[94] K. Takahashi, C. Charles, R. W. Boswell, T. Kaneko and R. Hatakeyama, 2007, Phys. Plasmas, 14, 114503.

[95] E. O. Johnson and L. Malter, 1950, Physical Review. 80, 58.

[96] G. S. Kirnev, V.P. Budaev, S.A. Grashin, L.N. Khimchenko and D.V. Sarytchev, 2005, Nucl. Fusion 45, 459-467.

[97] C. Riccardi, G Longoni, G. Chiodini and M. Fontanesi, 2001, Rev. Sci. Instrum. 72, 461.

[98] P. M. Bryant, S. A. Voronin, J. W. Bradley and A. Vetushka, 2007, Journal of Appl. Physics. 102, 043302.

[99] Sin-Li Chen and T. Sekiguchi, 1965, Journal of Appl. Physics. 36, 2363.

[100] M. Y. Naz, A. Ghaffar, N. U. Rehman, S. Naseer, and M. Zakaullah, 2011, Progress In Electromagnetics Research, Vol. 114, 113-128.

[101] K. K. Barada, P. K. Chattopadhyay, J. Ghosh, S. Kumar and Y. C. Saxena, 2012, Rev. Sci. Instrum. 83, 063501.

[102] R. R. Arslanbekov, N. A. Khromov and A. A. Kudryavtsev, 1994, Plasma Sources Sci. Technol. 3, 528.

[103] V. I. Demidov, S. V. Ratynskaia, K. Rypdal, 2002, Rev. Sci. Instrum. 73, 3409.

[104] T. K. Popov, P. Ivanova, M. Dimitrova, J. Kovacic, T. Gyergyek, and M. Cercek, 2012, Plasma Sources Sci. Technol. 21, 025004.

[105] V. A. Godyak, R. B. Piejak, B. M. Alexandrovich and V. I. Kolobov, 1998, Phys. Rev. Lett. 80, 3264.

[106] Yu. O. Tyshetskiy, A. I. Smolyakov, and V. A. Godyak, 2003, Phys. Rev. Lett. 90, 255002.

[107] R. H. Huddlestone, and S. L. Leonard, 1965, Plasma Diagnostic Technique, Academic Press, New York.

[108] K. K. Chi, T. Sheridan, and R. W. Boswell, 1999, Plasma Sources Sci. Technol. 8, 421.

[109] T. Shoji, Y. Sakawa, S. Nakazawa, K. Kadota, and T. Sato, 1993, Plasma Sources Sci. Technol. 2, 5.

[110] K. Suzuki, K. Nakamaura, H. Ohkubo, and H. Sugai, 1998, Plasma Sources Sci. Technol. 7, 13.

[111] R. W. Boswell, 2006, Astrophys. J., 640, L199.

[112] S. A. Cohen, N. S. Siefert, S. Stange, R. F. Boivin, E. E. Scime, and F. M. Levinton, 2003, Phys. Plasmas 10, 2593.

[113] A. M. Keesee, E. E. Scime, C. Charles, A. Meige, and R. Boswell, 2005, Phys. Plasmas 12, 093502.

[114] N. Plihon, P. Chabert, and C. S. Corr, 2007, Phys. Plasmas 14, 013506.

[115] K. Takahashi, K. Oguni, H. Yamada, and T. Fujiwara, 2008, Phys. Plasmas 15, 084501.

[116] O. Sutherland, C. Charles, N. Plihon, and R. W. Boswell, 2005, Phys. Rev. Lett. 95, 205002.

[117] T. Schroder, O. Grulke and T. Klinger, 2012, Euro. Phys. Lett, 97, 65002.

[118] E. Ahedo, and M. M. Sanchez, 2009, Phys. Rev. Lett. 103, 135002.

[119] F. Perkins, and Y. C. Sun, 1981, Phys. Rev. Lett. 46, 115.

[120] A. Meige, R. W. Boswell, C. Charles, and M. M. Turner, 2005, Phys. Plasmas 12, 052317.

[121] K. Goswami, K. Saharia, and H. Schamel, 2008, Phys. Plasmas 15, 062111.

[122] J. Carr Jr, P. A. Cassak, M. Galante, A. M. Keesee, G. Lusk, R. M. Magee, D. McCarren, E. E. Scime, S. Sears, R. Vandervort, N. Gulbrandsen, M. Goldman, D. Newman, and J. P. Eastwood, 2013, Phys. Plasmas 20, 072118.

[123] C. Charles and R. W. Boswell, 2007, Appl. Phys. Lett. 91, 201505.

[124] A. M. Keese, E. E. Scime, C. Charles, A. Meige, and R. W. Boswell, 2005, Phys. Plasmas, 12, 093502.

[125] C. Charles and R. W. Boswell, 2007, Appl. Phys. Lett. 91, 201505.

[126] J. Potkalitsky, R Dahlburg and D. Montgomery, 1981, Bull. Am. Phys. Soc. 26, 1025.

[127] N. Hershkowitz, G. L. Payne, C. Chen and j. P. DeKock, 1981, Plasma Phys, 23, 903.

[128] I. D. Sudit, and F. F Chen, 1996, Plasma Sources Sci. Technol. 5, 43-53.

[129] F. F Chen, I. D. Sudit and M. Light, 1996, Plasma Sources Sci. Technol. 5, 173-180.

[130] M. U. Siddiqui, J. F. Kim, C. D Jackson, and N. Hershkowitz, 2015, Plasma Sources Sci. Technol. 24, 015022.

[131] R. T. Shiung and N. Hershkowitz, 1998, Phys. Rev. Lett. 80, 4677.

[132] V. A. Godyak, R. B. Piejak, B. M. Alexandrovich, and V. I. Kolobov, 1998, Phys. Rev. Lett. 80, 3264.

[133] V. A. Godyak and V. I. Kolobov, 1997, Phys. Rev. Lett. 79, 4589.

[134] V. A. Godyak and V. I. Kolobov, 1998, Phys. Rev. Lett. 81, 369.

[135] M. Kramer, Y. M. Aliev, A. B. Altukhov, A. D. Gurchenko, E. Z. Gusakov, and K. Niemi, 2007, Plasma Phys. Control. Fusion, 49, A167-A175.

[136] D. Arnush, and C. F. Kennel, 1973, Phys. Rev. Lett. 30, 597.

[137] R. Boswell, 1975, Physics Letters A, 55, 93-94.

[138] R. Boswell, and M. J. Giles, 1976, Phys. Rev. Lett. 36, 1142.

[139] K. K. Barada, P. K. Chattopadhyay, J. Ghosh, S. Kumar and Y. C. Saxena, 2013, Phys. Plasmas, 20, 042119.

[140] A. W. Molvik, A. R. Ellingboe, and T. D. Rognlien, 1997, Phys. Rev. Lett. 79, 233.

[141] C. Charles, 2010, Appl. Phys. Lett. 96, 051502.

[142] S. K. Saha, S. Chowdhury, M. S. Janaki, A. Ghosh, A. K. Hui, and S. Raychaudhuri, 2014, Phys. plasma. 21, 043502.

[143] S. Rao and N. Singh, 2012, Phys. plasma. 19, 093507.

[144] S Saloum, M Akel and B Alkhaled, 2009, J. Phys. D: Appl. Phys. 42 085201.

[145] V A Godyak and V I Demidov, 2011, J. Phys. D: Appl. Phys. 44 233001.

[146] K. Takahashi, C. Charles, R. Boswell and R. Hatakeyama, 2008, Phys. Plasmas 15, 074505.

[147] K. Takahashi, C. Charles, R. Boswell, W. Cox and R. Hatakeyama, 2009, Appl. Phys. Lett. 94, 191503.

[148] D. F. Berisford, R. D. Bengtson and L. L. Raja, 2010, Phys. Plasmas 17, 033503.